

國立交通大學

電機與控制工程研究所

碩士論文

整合 SOI 與 SU-8 之微光學平台製作

**MEMS Based Micro Optical Bench with
Integration of SOI and SU-8**



研究生：吳忠衛

指導教授：邱一 博士

中華民國九十五年十月

整合 SOI 與 SU-8 之微光學平台製作

**MEMS Based Micro Optical Bench with
Integration of SOI and SU-8**

研究生:吳忠衛

Student: Jhong-Wei Wu

指導教授:邱一

Advisor: Yi Chiu

國立交通大學 電機學院

電機與控制工程研究所



A Thesis

Submitted to Department of Electrical and Control Engineering
College of Electrical and Computer Engineering
National Chiao Tung University
In Partial Fulfillment of the Requirement
For the Degree of
Master
In

Electrical and Control Engineering

October 2006

Hsinchu, Taiwan, R.O. C.

中華民國九十五年十月

中文摘要

近年來在半導體產業的發展之下，微機電製程技術有許多重大的發展。對於要求更輕更小的光學資料儲存系統，針對微型化與輕量化的研究也如火如荼的進行著。而微光機電技術(Micro Optical Mechanical System)正是提供製造更小更輕的光學資料儲存系統的一個好方法。

利用微光機電技術所製造的微光學讀取頭是實現微型化以及輕量化的方向。此微光學讀取頭是由微光學平台以及可控制的聚焦透鏡所組成。本論文主要探討的是如何完成微光學讀取頭中的微光學平台。

此微光學平台是以數個三維微鏡面結構所組成。採用應力幾乎為零且結構較厚的 SOI(Silicon On Insulator)基板製作微鏡面，以避免一般利用多晶矽製作時可能發生的翹曲現象。並且整合 SU-8 以作為應力臂來抬升微鏡面以及作為栓鎖結構以提供鏡面旋轉的機制。另外嘗試採用 SU-8 作為光學元件如 grating 以及 Fresnel lens 檢視其作為光學元件的成效。

在組裝上是利用探針翻轉元件至預定角度並且利用卡榫機制將其固定。另外為了避免在人工方式的組裝過程中可能產生的風險，也對於自組裝的方法做了嘗試。利用錫球熔融狀態下的表面張力作為組裝時的動力來源以完成組裝的目的，另外錫球尚可作為傳導光電流的導體使用。

在本論文中的製程有別於一般常用的多晶矽製程，採用類似面型微加工製程，藉由整合 SU-8 與 SOI 來減少製程步驟。並且在利用錫球自組裝的方式之下將可再次的簡化製程。

Abstract

Recently, the Micro Electro Mechanical Systems (MEMS) technology has many important developments with the rapid progress in the semiconductor industry. The requirement of miniaturization and lightness pushes the development of more miniature and lighter optical data storage system. Micro optical pick-up head fabricated by Micro-Opto-Electro-Mechanical System (MOEMS) technology is one of the methods to realize portable high-capacity optical storage systems. In this thesis, the micro optical pick-up is composed of a micro optical bench and a controllable focusing lens bonded together. The fabrication process is the focus in this thesis.

In this thesis, the optical bench of the micro optical pick-up head is composed of several 3D micro devices. The silicon on insulator (SOI) wafers with almost zero stress are used in order to prevent the stress-induced curvature of micro devices made by poly silicon. Integrating SU-8 to fabricate stress beams to lift up the devices and anchors for the rotation of devices. SU-8 also attempt to be fabricated as optical component, such as grating and Fresnel lens.

Devices is rotated to desired degree by probe and fixed by latch mechanism. To avoid manual operation, the self-assembly is introduced in the fabrication. The power of assembly is the surface tension of melting solder. Furthermore, solder is also a conductive material.

In this thesis, integration of SOI and SU-8 in a surface-micromaching-like process can simplify the process. And the self-assembly approach of solder can simplify the process more.

誌 謝

碩士生涯隨著這本論文的完成，也即將步入尾聲。首先要感謝我的父母在生活上對我的栽培，也對於他們在我遭遇到挫折時在精神上給予的支持與鼓勵點滴在心頭，讓我每每在心境低落之時猶如見到光芒般的將我帶出低潮的深淵。在研究所的生涯之中，我的指導教授，邱一老師，啟發了我如何作研究的態度與精神，從一個對如何做研究一知半解的毛頭小子，慢慢掌握該怎樣去做你想要做的目標。而老師的努力不懈的精神也實實在在的對我做足了身教不如言教的示範，讓我有個很好的學習典範。在這邊學生我要再次向老師您深深的一鞠躬以表感謝。

碩士生涯的期間，實驗室的歡樂氣氛也是振奮著實驗作失敗時心情的一劑強心針。很開心，進到這麼一個氣氛和諧的實驗室。謝謝企桓學長以及秦輔學長在製程上給予的協助，也謝謝學長志偉、文中、育杉，英傑在知識上的傳承。同學建勳、炯廷、均宏、亦謙和機械所的志柏，感謝你們的陪伴與付出。在實驗室中的歡樂、做實驗失敗彼此的打氣、在 SRC 裡做製程度過的時光，這些的種種都會在我的記憶中深深的留下美麗的畫面，好好的收藏著。學弟繁果與煒智以及隔壁實驗室的同學與學弟們在平時實驗室中帶來的歡樂，更是讓這歡樂的氣氛帶來更加燦爛的顏色。

還有謝謝我的女友，千慧，在這兩年的陪伴，給了我很多的鼓勵以及支持。最後，帶著很開心的心情將這論文獻給我的父母、家人、朋友以及所有曾經幫助過我的人，期許著自己能將這兩年在交大所學到的交大人的精神，在往後的日子之中加以發揚光大有所作為，進而對社會有所貢獻。再次感謝所有曾經幫助過我的人，謝謝你們給予我的幫忙以及關懷。

Table of Content

中文摘要.....	i
Abstract	ii
誌謝.....	iii
Table of Content	iv
List of Figures	vi
List of Tables	x
Chapter1 Introduction	1
1-1 Motivation.....	1
1-2 Literature survey.....	4
1-2-1 Integrated device using SOI and SU-8.....	4
1-2-2 Three dimensional MEMS device and assembly mechanism.....	5
1-2-3 SU-8 negative photoresist.....	10
1-2-4 Photo detector.....	12
1-3 Thesis overview and organization.....	13
Chapter2 Principle and Design	14
2-1 Introduction.....	14
2-2 3D surface micromachined MEMS structure.....	14
2-2-1 single crystal silicon/SU-8 bimorph stress beam.....	14
2-2-2 Solder reflow self-assembly.....	21
2-3 Optical component – Fresnel lens.....	26
2-4 Integrated devices.....	29
2-5 Summary.....	30
Chapter3 Fabrication Process	31
3-1 Optical bench-integration of SOI and SU-8.....	31

3-1-1 Fabrication technology.....	36
3-2 Fabrication process of self-assembly by surface tension.....	39
3-3 Problems and discussions about fabrication process.....	43
3-4 Summary.....	50
4 • Experiment Results and Measurement.....	51
4-1 SU-8/single crystal silicon stress beam.....	51
4-2 Integrated device of optical bench.....	53
4-3 Measurement of optical devices.....	55
4-4 Photo detector.....	66
4-5 Summary.....	68
5 • Conclusion and Future Work.....	69
5-1 Conclusion.....	69
5-2 Future Work.....	69
Reference.....	72



List of Figures

Figure 1-1 Conventional optical pick-up head.....	1
Figure 1-2 SEM micrograph of the monolithic optical-disk pickup head.....	3
Figure 1-3 Schematic of the MEMS based optical pickup head.....	3
Figure 1-4 (a) bulk and (b) surface micromachining.....	5
Figure 1-5 Cross-section of microhinge.....	6
Figure 1-6 Schematic of the principle of step motion.....	6
Figure 1-7 Structure was lifted up by SDA.....	7
Figure 1-8 Rotating hinge flaps using magnetic actuation.....	7
Figure 1-9 Sequence of actuation. (a) ultrasonic vibrations heat and charge the polysilicon parts. (b) electrostatic repulsion forces the plate up.....	8
Figure 1-10 Principle of the polyimide V-groove joint.....	8
Figure 1-11 Large bending by three-V-groove connect in series.....	8
Figure 1-12 Typical assembly mechanism composed of stress-induced beam and locking components.....	9
Figure 1-13 Self-assembly by (a) photoresist, (b) solder.....	10
Figure 1-14 High aspect ratio SU-8 device.....	11
Figure 1-15 Layout schematic of photodiode.....	13
Figure 2-1 Base line process for SU-8.....	16
Figure 2-2 Wafer bowing due to the stress in the SU-8 layer.....	17
Figure 2-3 Dimensions of a cantilever beam.....	17
Figure 2-4 Resulting forces and moments.....	18
Figure 2-5 Deflection vs. beam length.....	20
Figure 2-6 Two dimensional geometry for surface tension powered rotation.....	22

Figure 2-7 Equilibrium shapes for different final angle.....	23
Figure 2-8 Dimension of an equivalent shape for solder ball.....	24
Figure 2-9 Definition of over-rotation.....	24
Figure 2-10 diagram of self-lacking mechanism: (a) 2D cross-section view, (b) 3D model.....	25
Figure 2-11 Schematic of (a) continuous relief of Fresnel zone plate, (b) multiple-step binary Fresnel zone plate.....	26
Figure 2-12 Process cycles of multi-level binary-optics microlens: (a) two-phase structure (b) four-phase structure (c) eight-phase structure.....	27
Figure 2-13 Mask of Fresnel lens (a) SU-8, (b) silicon nitride.....	28
Figure 2-14 Layout of the optical bench- (a) Stress beam assembly, and (b) Surface tension assembly.....	29
Figure 3-1 Schematic of structures and materials.....	32
Figure 3-2 Fabrication process of the optical bench with stress beam.....	33
Figure 3-3 Fabrication process of the optical bench with surface tension.....	39
Figure 3-4 The phenomenon of Si ₃ N ₄ etching: (a) unopened release hole (b) narrowed release hole.....	44
Figure 3-5 Disappearance of the outer rings.....	44
Figure 3-6 The shapes of PR before and after hard bake.....	45
Figure 3-7 Non-vertical and reduced rotational space.....	45
Figure 3-8 Vertical shape for 5μm-thick SiO ₂ etching.....	46
Figure 3-9 Solder ball place on the god pad and pre-melt directly.....	47
Figure 3-10 Assembly is failure after solder melt.....	48
Figure 3-11 (a) and (b) are the different shapes discovered on the same chip. (c) and	

(d) are the cross section view of (a) and (b).....	48
Figure 3-12 Schematic and SEM for solder melt.....	49
Figure 3-13 Layout of the inappropriate latch structure.....	50
Figure 4-1 SU-8/SCS stress beams.....	52
Figure 4-2 SU-8 stress-induced beam measured by WYKO-NT1100.....	52
Figure 4-3 Deflection of stress beams with different lengths.....	53
Figure 4-4 Integrated optical bench (a) Si_3N_4 based devices. with 135° reflective mirror and photo diode, (b) SU-8 based devices, (c) Si_3N_4 based devices.....	54
Figure 4-5 Figure 4-5: Failed assembly of latch structure. (a) the C-shape SU-8 anchor, (b) latch and notch, (c) AA' cross section of latch rotation.....	55
Figure 4-6 Curvature of the Si_3N_4 grating.....	56
Figure 4-7 Curvature of the Si_3N_4 PBS.....	57
Figure 4-8 Curvature of the Si_3N_4 Fresnel lens.....	57
Figure 4-9 Curvature of the SU-8 grating.....	58
Figure 4-10 Curvature of the SU-8 PBS.....	58
Figure 4-11 Curvature of the SU-8 Fresnel lens.....	59
Figure 4-12 The curves of reflective mirror.....	59
Figure 4-13 SEM of SU-8 grating.....	60
Figure 4-14 Schematic diagram of optical measurement of grating.....	61
Figure 4-15 CCD image of diffracted spot.....	61
Figure 4-16 Optical measurement of grating.....	62
Figure 4-17 SEM of SU-8 Fresnel lens.....	63
Figure 4-18 Schematic diagram of the optical measurement.....	64

Figure 4-19 CCD image (a) Fresnel lens, (b) focused spot.....64

Figure 4-20 Analysis of focused spot image.....65

Figure 4-21 135° reflective mirror and photo detectors.....66

Figure 4-22 Reverse biased I-V curve of photo diode with and without light.....67

Figure 4-23 Forward biased I-V curve of photo diode with and without light.....67



List of Tables

Table 2-1 The bowing was measured over a 72mm distance of a fully exposed 4inch, 520um thick silicon wafer.....	17
Table 3-1 Comparison of the two fabrication processes.....	42



Chapter 1

Introduction

1-1 Motivation

People are having a new world in the multimedia era in the rapid progress of the information technology. High fidelity is important when translating the information from analog to digital forms or vice versa. The amount of data becomes very large. Therefore increasing the data storage density plays a very important role. On the other hand, it is also very crucial to obtain rapid access speed of information. Miniature and lighter optical data storage system can achieve these requests. The miniature optical pick-up head can replace the conventional buck head to reduce the access time of information.

The conventional optical pick-up head consists of a laser diode, a grating plate, a beam splitter, a collimator, a mirror, an objective and photodiodes, as showing in Figure 1-1. The laser beam from the laser diode passes through the diffraction grating and diffracted beams are produced. The zeroth-order beam is used to read the data on the disk; the first-order beams can be used to maintain the correct tracking of the spot.

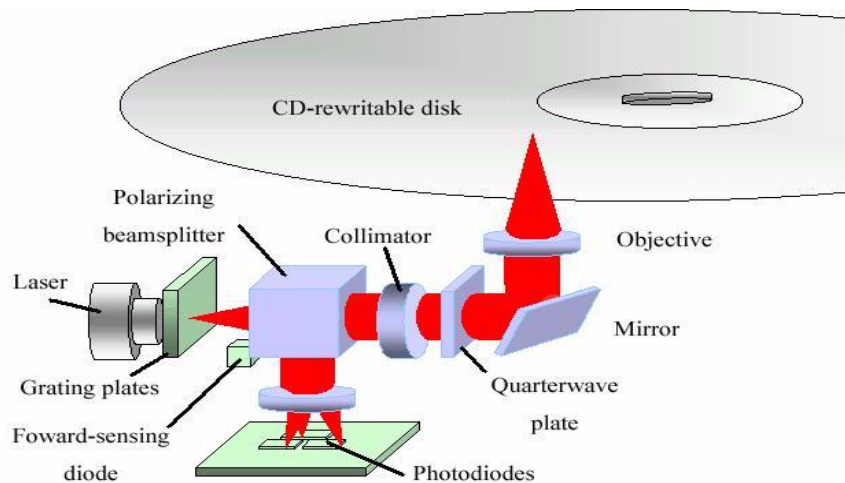
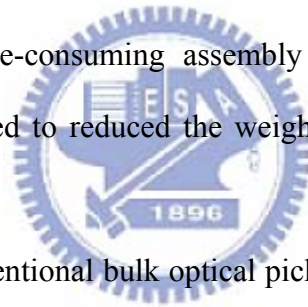


Fig1-1: Conventional optical pick-up head

Then, the light passes through the beam splitter and is converted into a parallel beam by the collimator. After the quarter wave plate, the beam becomes circularly polarized. The beam is then focused onto the surface of disc by the objective lens whose position is maintained by a servo mechanism. The reflected beam becomes orthogonally linearly polarized with respect to the source beam after passing through the quarter wave plate and then is reflected by the polarizing beam splitter into the detectors. Finally, the photocurrent can be measured as the data information by current detected circuits.

As the portable digital devices such as cellular phones, digital cameras and MP3 players are spreading these days, the demand for mobile storage devices increases rapidly. The traditional optical pick-up head is constructed with discrete components and needs complex and time-consuming assembly processes. Therefore, various techniques have been proposed to reduced the weight and volume and simplify the assembly processes.



Compared with the conventional bulk optical pick-up head, miniaturized devices have advantages such as reduced size, weight, cost and enhancement of application flexibility. Recently, MEMS technology has been employed to make various electromechanical components. These devices can be fabricated using the microfabrication batch processes and the assembly can be simplified. The free-space micro-optical bench is an example of this technology. Figure 1-2 is the single-chip optical-disk pickup head developed by M. C. Wu et al. [1]. This optical system has several advantages. First, this is made by an IC-like batch fabrication process. The entire optical system is a batch production and can be monolithically integrated with several different elements on a single chip. Second, the size and weight of the optical systems can be greatly reduced. Third, the optics can be prealigned during the design of layout.

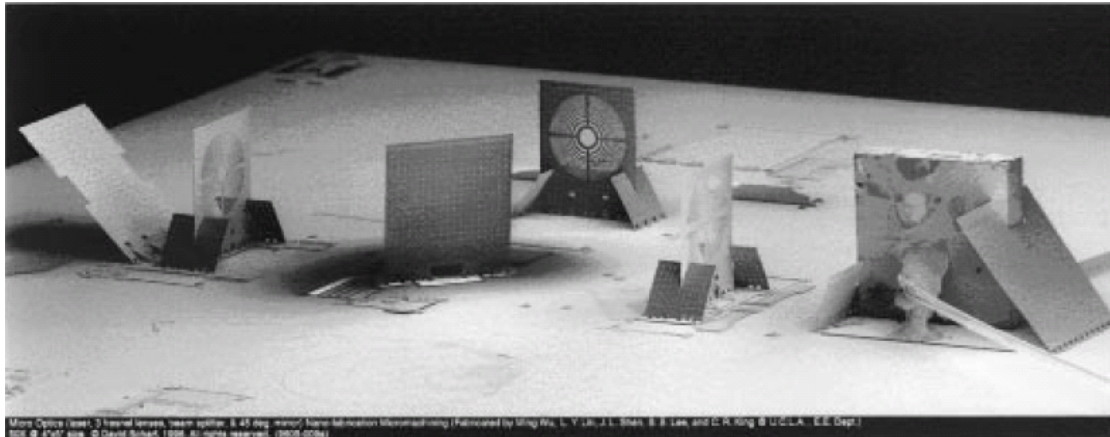


Figure 1-2: SEM micrograph of the monolithic optical-disk pickup head [1].

The objective of our research is to simplify the fabrication process and ensure the functionality of the optical pickup head. The MEMS-based optical pickup head in this research is composed of a laser diode, a coupling and beam shaping lens, a grating plate, a beam splitter, a focusing lens, focusing actuators and photo detectors, as shown in Figure 1-3. This optical system is similar to the conventional one in Figure 1-1. Because of the limits on the three dimensional structure in MEMS, The pick-up head in Figure 1-3 must be separated into two parts. One is the optical bench at the bottom, which has a light path for coupling, shaping, reflection and signal detection. Another is an actuator to tracking and focusing the spot at the correct position on the disk.

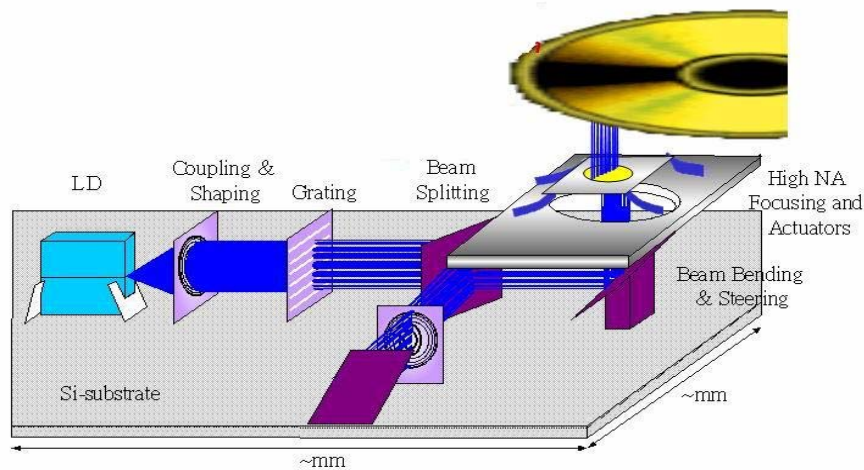


Figure 1-3: Schematic of the MEMS based optical pickup head

This thesis focuses on the fabrication and integration of the optical bench, using SOI technologies. Traditional surface micromachining uses thin poly-silicon layers as the structural and optical material. However, it has several disadvantages for optical applications, such as surface curvature induced by residual stress, absorption of visible light, and poor performance as an optical detector. So, a novel fabrication process using SOI and SU-8 negative photoresist is demonstrated to replace the polysilicon micromachining. Photo diode and other circuits can also be integrated in this process.

Then two assembly processes are investigated in this thesis to lift up the microstructures. One is stressed bimorph beams composed of SU-8 and single crystal silicon (SCS). The other is by the surface tension of melted solder ball.

1-2 Literature survey



1-2-1 High aspect ratio surface micromachining

As mentioned above, poly-silicon has several disadvantages for mechanical and optical applications. To reduce the effect of residual stress, structures employing silicon-on-insulation (SOI) wafer or high-aspect-ratio polysilicon processes were proposed. The single crystal silicon of SOI is recognized as a superior material due to its low intrinsic stress and excellent surface smoothness. The biggest remaining obstacle in SOI process is the inherent lack of out-of-plane motion. To solve this problem, a complex fabrication process of high aspect ratio SOI MEMS system has been proposed [2]. That was accomplished by applying multiple-mask high aspect ratio etches from both the front- and back-side of the SOI device layer, forming beams at different levels. Integration the SOI and polysilicon is another approach to solve the problem [3]. The polysilicon is used to form the bimorph beams. Furthermore, the

residual stress of high aspect-ratio polysilicon created by refilling deep trenches can be almost zero [4]. However, the high deposition temperature of polysilicon in these processes may affect the performance of photo detector or circuits if they are to be fabricated on the same substrate. In this thesis a novel fabrication process to integrate the SOI and SU-8 negative photoresist is demonstrate as a low-temperature and inexpensive process compared to the current technologies.

1-2-2 Three dimensional MEMS device and assembly mechanism

In MEMS, all fabrication processes are derived from surface and bulk micromachining. The purpose of bulk micromachining is to selectively remove significant amounts of silicon from the substrate [5]. Figure 1-4(a) is the schematic of isotropic and anisotropic etching in bulk micromachining. The other technology, surface micromachining, is characterized by the fabrication of micromechanical structures from deposited thin films [6]. Figure 1-4(b) shows schematics of the surface micromachining. In general, the 2D photolithography technique limits the MEMS structures to two dimensions. Therefore, the microhinges were proposed to allow the polysilicon thin film to be patterned by photolithography and then folded into 3D structures [7]. The schematics show the cross-section and rotation process of the microhinge in Figure 1-5.

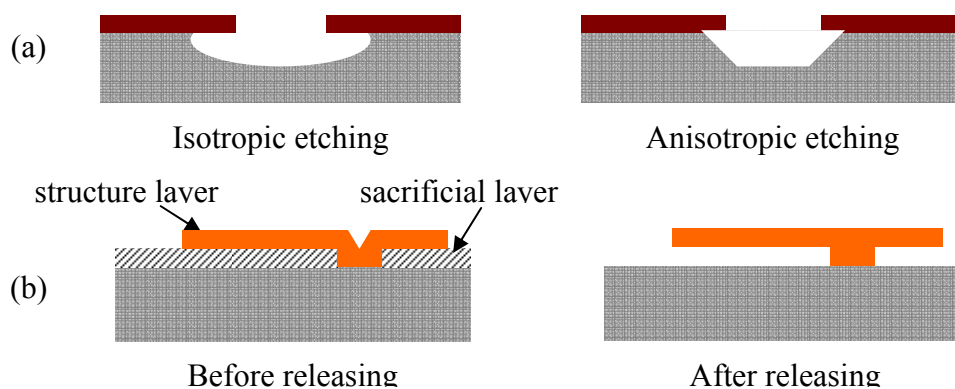


Figure 1-4: (a) bulk and (b) surface micromachining

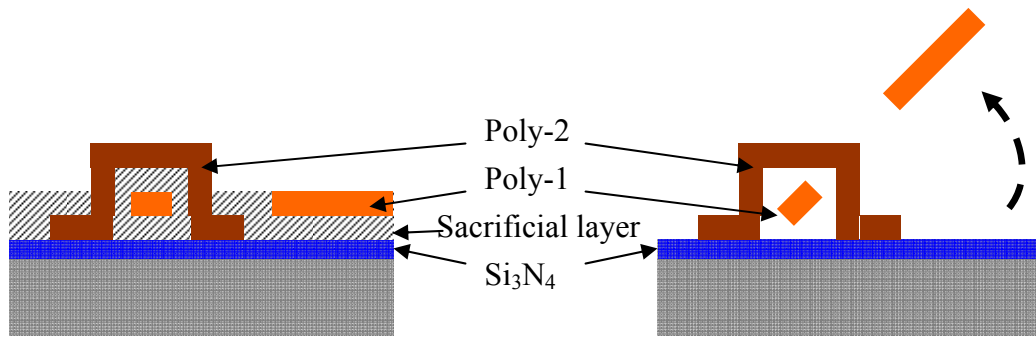


Figure 1-5: Cross-section of microhinge

Numerous rotational assembly processes have been proposed to rotate the moveable structure for 3D devices, as discussed in the following paragraphs.

Scratch drive actuator

The scratch drive actuator (SDA), illustrated in Figure.1-6 (a), consists of the plate, bushing, support arms, insulator and substrate electrode [8]. When a voltage is applied, the plate is pulled down towards the substrate. When the voltage is removed, the plate and bushing return to their horizontal position, but translate forwards a small distance. By driving the device with a periodic voltage, the SDA can advance across the substrate at a velocity and step size determined by the frequency and amplitude of the driving signal, as shown in Figure.1-6 (b). SDA can provide an external force for assembly. Figure 1-7 shows an out-of-plane device lifted by the SDA [8].

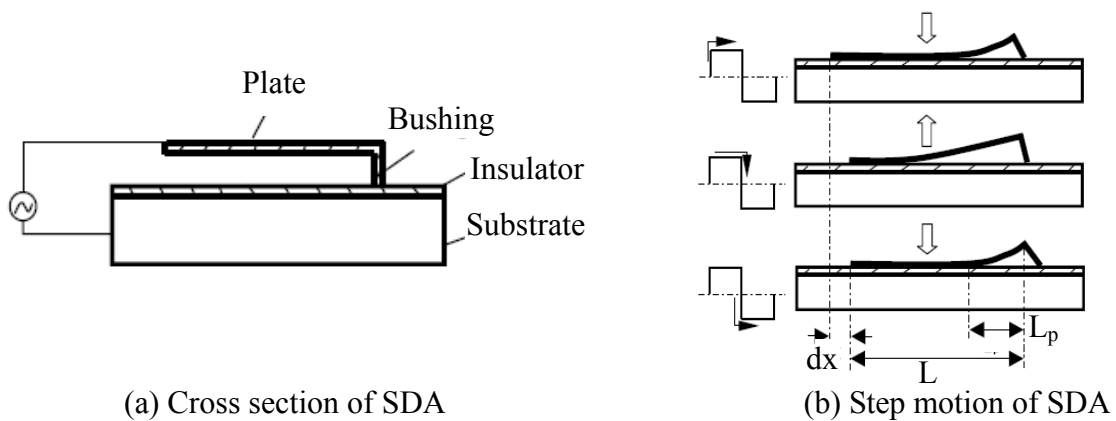


Figure 1-6: Schematic of the principle of step motion [8]

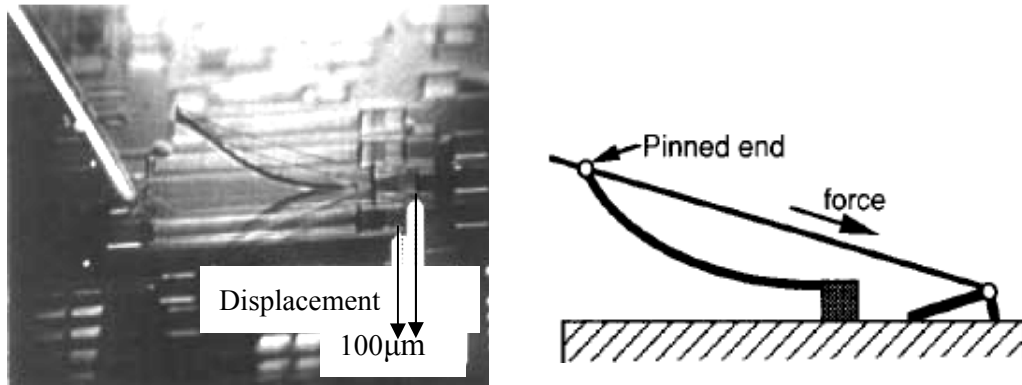


Figure 1-7: Structure was lifted up by SDA [8]

Magnetic force

This method uses magnetic actuation of hinged to lift surface micromachined structures [9]. Figure 1-8 shows the principle of this method. Electroplated magnetic material (Permalloy) is integrated with hinged microstructures. When giving an external magnetic field, the rotational angle of hinge structure is determined by the volume of the magnetic material.

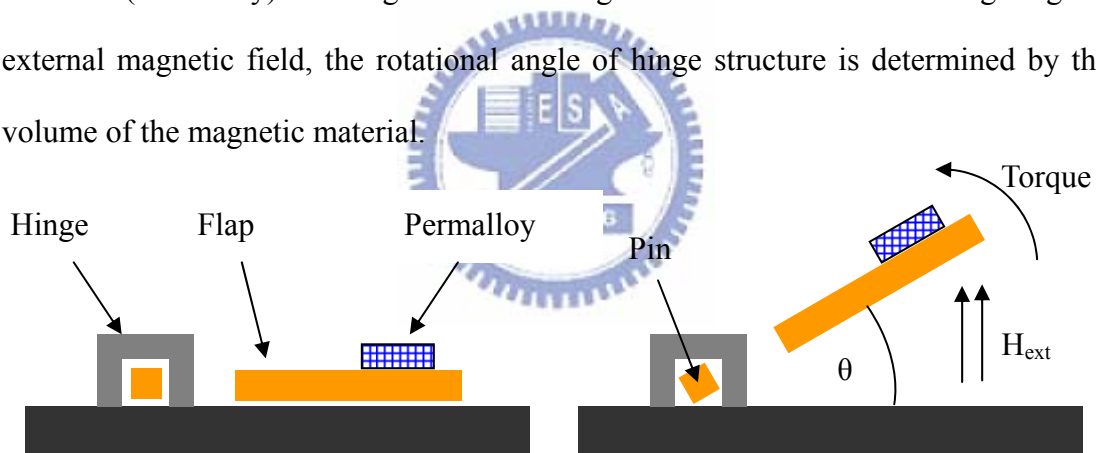


Figure 1-8: Rotating hinge flaps using magnetic actuation [9]

Ultrasonic vibration energy

This method uses ultrasonic vibrations generated with an attached piezoelectric actuator to vibrate polysilicon plates on silicon nitride or polysilicon surfaces. The rubbing between the substrate and the structures creates contact electrification charge. The charge repulsion effectively stabilizes the surface micromachined flaps to the upright position as shown in Figure 1-9 [10]. Nearly perfect yield over the entire area can be achieved.

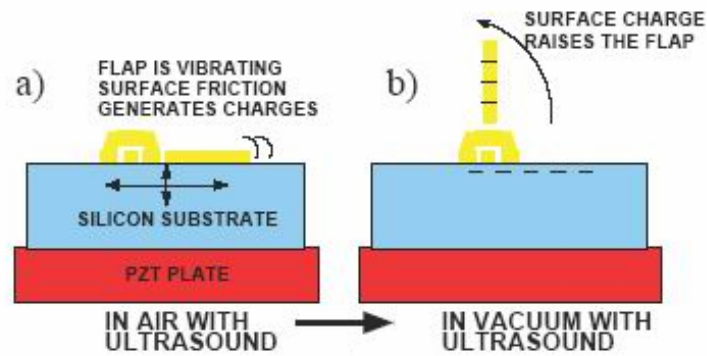


Figure 1-9: Sequence of actuation. (a) ultrasonic vibrations heat and charge the polysilicon parts. (b) electrostatic repulsion forces the plate up [10]

Thermal shrinkage of polyimide

Self-assembly was approached by the thermal shrinkage of polyimide in V-grooves [11], as shown in Figure 1-10. The polyimide in the V-grooves shrinks when it is cured. The absolute lateral contraction length of the polyimide is larger at the top of the V-groove than at the bottom. The different shrinkage results in a rotation. Large bending angles can be obtained by connecting several V-grooves in series. Figure 1-11 shows the schematics view and photo graph of a three-V-groove connection joint.

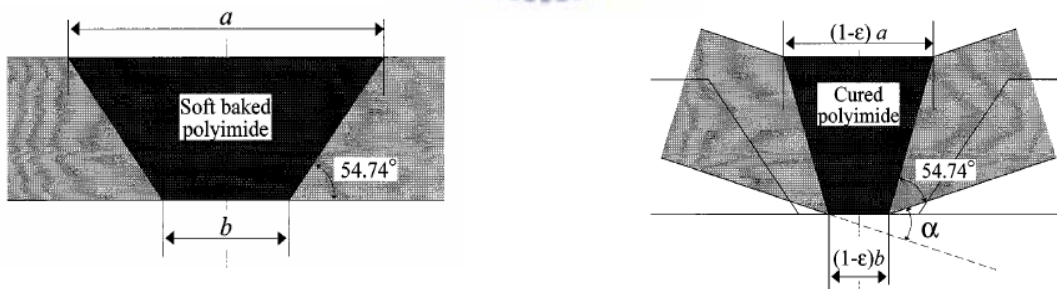


Figure 1-10: Principle of the polyimide V-groove joint [11]

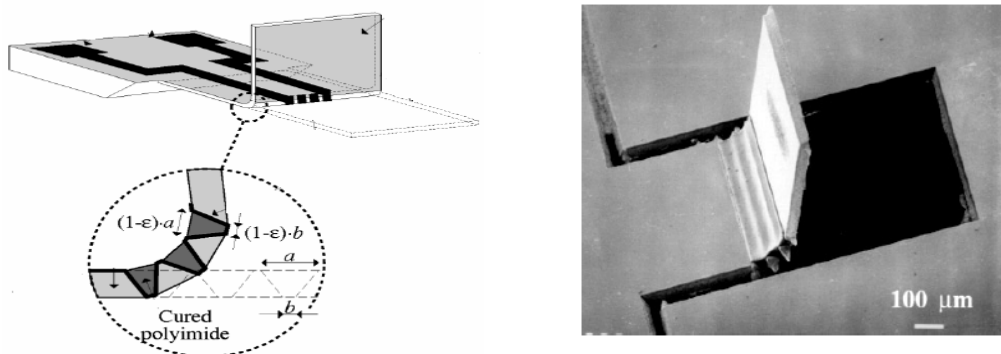


Figure 1-11: Large bending by three-V-groove connect in series [11]

Stress-induced supporting mechanism

The residual stresses that are inherent in thin films have been exploited to lift up and assemble the micro structures [12]. In Figure 1-12, the typical assembly mechanism is composed of stress-induced bimorph beams and locking components [13].

Bimorph stress beams can be fabricated using different materials. For example, polysilicon/gold bimorph stress induced beams for three-dimensional self-assembly of MEMS device was reported in [14]. However, as reported in [15], the displacement of stress-induced beam would drop by 70% after 6 months because of metal relaxation.

Si_xN_y /polysilicon bimorph beams were exploited to lift up and assemble the micro structures [13] and evaluated using various reliability tests [16]. However, in the micro optical bench in this thesis, the Si_3N_4 layer is used for optical devices and its thickness is restricted.

SU-8/polysilicon bimorph actuator probe arrays integrated with a sensing part were proposed in [16]. They were actuated employing the difference of the thermal expansion coefficients between polysilicon and SU-8.

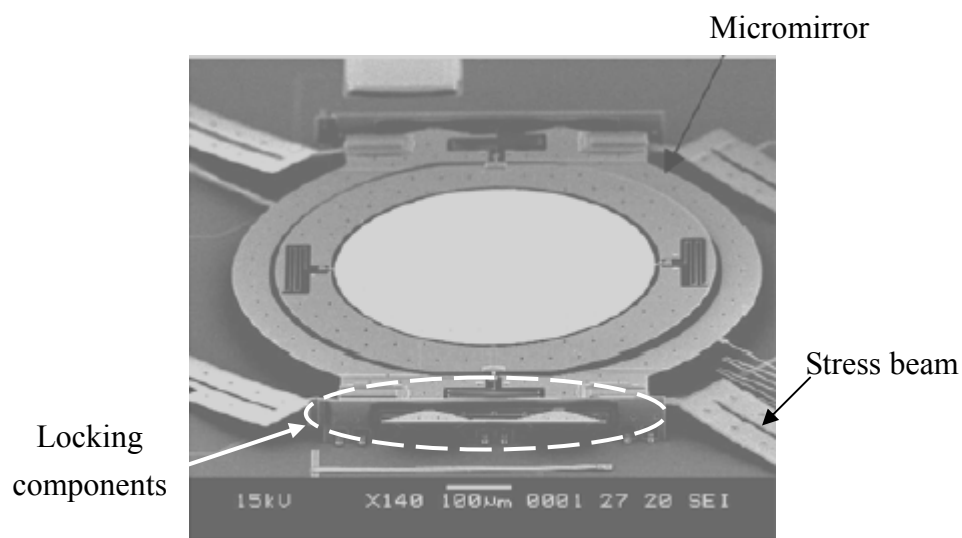


Figure 1-12: Typical assembly mechanism composed of stress-induced beam and locking components [13].

Surface tension powered

Surface tension can be used as the power for self-assembly. The fabrication processes are to pattern the device first, and then pattern the photoresist or solder on the rotation joints. Then the plate will be flipped up by the surface tension power when the photoresist or solder is melt, as shown in Figure1-13 [17, 18].

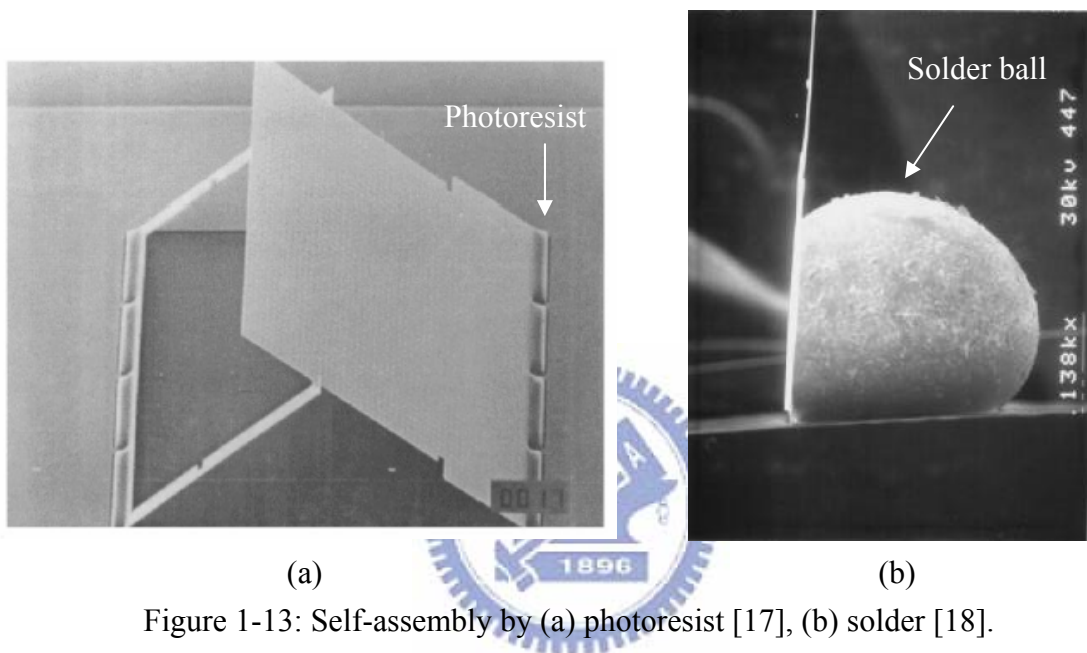


Figure 1-13: Self-assembly by (a) photoresist [17], (b) solder [18].

Bimorph stress beam and surface tension are two methods of assembly in this thesis. Bimorph stress beam is used to lift up device and then the probe flips the device over for assembly. Surface tension is adopted for self-assembling. And solder is chosen as the melted material because it is a conductive material which can connect the photodiode with circuits.

1-2-3 SU-8 negative photoresist

SU-8 is an epoxy-based negative thick photoresist. It is not only used for masking and pattern transfer, but is also directly used as a polymeric material to fabricate micro-mechanical component. The material has several properties that make it suitable for MEMS applications [19] [20]. The most important characteristic is the

high transparency in UV range, which makes it possible to expose the photoresist up to much deeper range with conventional UV photolithography equipment. Furthermore, it is possible to coat the material by conventional spin coater up to several hundreds of microns by single coating. So the use of SU-8 for high aspect ratio and structures in MEMS application is popular recently. The amount of cross-linkage in SU-8, further, is a key factor for lithography. Additionally, SU-8 has a good endurance to chemicals and plasma, which allows more freedom in process design. Figure 1-14 shows the high aspect ratio of SU-8 in MEMS application [20].

Many thermal and mechanical properties of SU-8 had been studied. The influence of curing conditions, such as baking temperature, baking time and UV dosage, on the thermal and mechanical properties of the resultant coatings was studied in detail. The stress which occurs at the curing process can be used to fabricate the stress beam. On the other hand, if it is excessively cross-linked, the patterns are distorted and sometimes adhesion failure occurs. So the adhesion between SU-8 and silicon should be well controlled. In this thesis, the SU-8 is used in bimorph stress beam and anchor structure. Because SU-8 can be spin coated with high aspect ratio, it can result in a high bending deflection for stress beam to lift up devices.

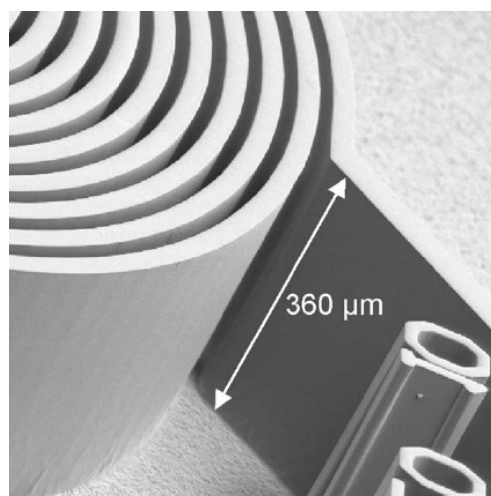


Figure 1-14: High aspect ratio SU-8 device [20]

1-2-4 Photo detector

Recently, silicon photodiodes have been the focus of attention as a widely used standard detector, despite its sensible light wavelength is restricted from 100nm to 1100nm. Its applications include CCD imaging, pattern recognition and front-end receiver for the Opto-Electronic Integrated Circuit (OEIC) [21, 22]. This is due to its simple layout and ease to integrate with other circuitries on the same chip at low cost [23].

A simple theory for photocurrent generation is that light absorbed in the depletion region of a semiconductor diode produces electron-hole pairs, which will be separated by the applied or built in electric field. This phenomenon generates current flow in the diode. The electron-hole pairs that are generated outside the depletion region will swiftly recombine with the majority carriers and become undetectable. Therefore, photodiode with excellent performance should be designed with a wide depletion region. In general, the depletion width varies with the doping profiles. A lower doping concentration and a higher resistivity in the substrate are desirable for a wide depletion region. However, this approach is limited by the technology and fabrication processes, and it will certainly affect the performance of other circuitries when they are integrated in a single chip. The layout design can also help improve the performance [24]. Figure 1-15 shows a simple design layout of a diode. The inside rectangular part is the N⁺ cathode of the diode. The ohmic contact is made only at the corner of the N⁺ region. In this layout, the PN junction is formed mainly between the bottom part of the N⁺ region and the P-substrate. This is also the model of the photo diode in this thesis.

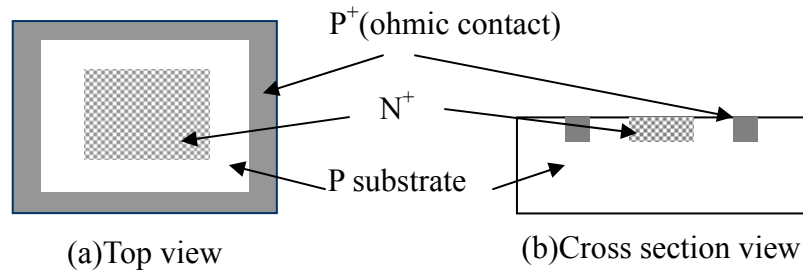


Figure 1-15: Layout schematic of photodiode

1-3 Thesis overview and organization

To realize the MEMS based optical pick up head, a free-space optical bench will be constructed with a novel fabrication process to integrate SU-8 and SOI in this thesis. Therefore, the object of this thesis includes:

- (a) Testing and verifying the feasibility of the novel fabrication process to construct a basic optical bench;
- (b) Investigating self-assembly in the fabrication process of the optical bench;
- (c) Measuring the performance of optical element, especially the SU-8 based components.

The basic principles of bimorph residual stress beams and surface tension assembly are presented in Chapter 2. The fabrication processes and process issues are discussed in Chapter 3. The experiment and measurement results are presented in Chapter 4. Conclusion and future work are discussed in Chapter 5.

Chapter 2

Principle and Design

2-1 Introduction

A novel MOEMS structure employing SOI wafers and the negative photoresist SU-8 as structure materials is proposed to fabricate an optical bench. SU-8 is used as one of the materials for the residual stress beam. And the single crystal silicon (SCS) on the SOI wafer is the other material. Since the SU-8 is stable to get the desired thick pattern and has good endurance to chemicals and plasma, it also can be used in the optical component. Though stress beams are used in the assembly process, additional manual assembly is still needed. Therefore, the self assembly by the surface tension of the solder reflow is considered to simplify the assembly process. The principle of the stress beams and the surface tension is discussed in this chapter.

2-2 3D surface micromachined MEMS structure

Assembly is important in fabricating 3D MEMS structures. The stress beam and surface tension approaches are discussed and investigated in this chapter.

2-2-1 Single crystal silicon/SU-8 bimorph stress beam

SU-8 photoresist has its original as an IBM negative resist used in patterning and packaging of printed circuit boards in 1989 [25]. It is designed specially for ultra-thick, high-aspect-ratio MEMS. Several important properties of SU-8 make it

suitable for such applications. First of all, ultra- thick coating can be easily formed by multi-coating process. Secondly, the absorption for SU-8 in the UV spectrum is very low, so this allows the patterning of thick coatings. Thirdly, since SU-8 has high functionality, high degree of cross-link can be obtained, permitting a high aspect ration and straight sidewall to be achieved in lithographic applications. And because this reason, SU-8 also has high chemical and thermal resistance as well as good mechanical properties.

SU-8 has very high optical transparency above 360nm, so SU-8 is most commonly processed with conventional near UV (350~400 nm) radiation and i-line (365nm) is recommended. When fully processed, SU-8 create a glass-like surface that is extremely hard to remove.

The properties of SU-8 are very sensitive to the processing condition. Five variables, soft-bake time, exposure time, post-exposure bake (PEB) time, develop time, and different substrates, are important processing factors for the final properties of SU-8. Figure 2-1 shows the normal fabrication process flow and some details.

After prebake, a small tensile stress is introduced by the difference between the thermal expansion coefficients (TECs) of the wafer and SU-8 [26]. The stress is small because during the cooling phase of the prebake, polymer chain rearrangements take place in the resists that are not cross-link. The main stress is generated as the cross-link SU-8 cools down especially after hardbaking. In addition to the thermo-mechanical stress introduced by the difference of the TECs, stress due to resist polymerization is also present.

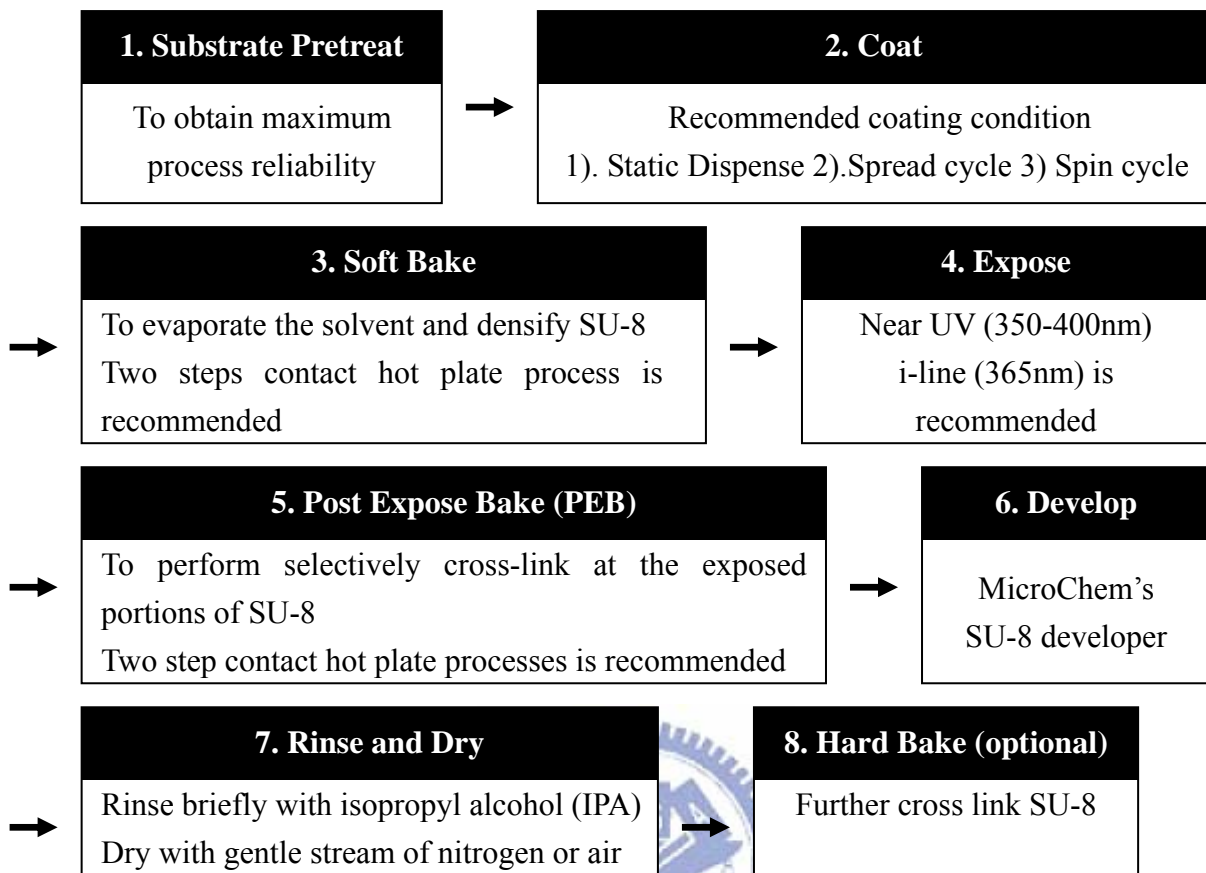


Figure 2-1: Base line process for SU-8

Since the thickness of SU-8 is comparable to the wafer thickness, this stress can be high and consequently the wafer is bowed. According to the experiment, the bowing of silicon wafer which is coated with SU-8 is shown in Figure 2-2. 520-um-thick silicon wafers were used in the experiment. The thickness of coated SU-8 were measured as 21 μm . In this experiment, four different hard bake time, 0 min, 10 min, 20 min, and 30 min were used. The stresses for different hard bake situations are calculated with the Young's Modulus = 4.6GPa [27] and shown in the Table 2-1. The calculated stresses are 13M Pa, 24M Pa, 27M Pa, and 27M Pa, respectively. So the maximum stress of SU-8 with this thickness is about 27M Pa. This value will be used in the following calculation of tip deflection of stress beam.

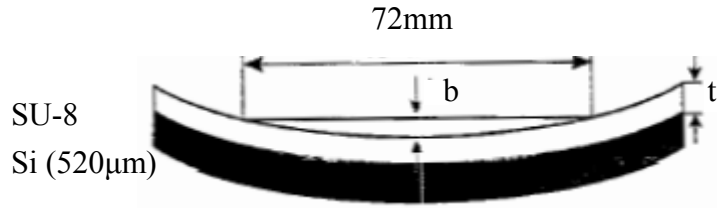


Figure 2-2: Wafer bowing due to the stress in the SU-8 layer

Table 2-1: The bowing was measured over a 72mm distance of a fully exposed 4inch, 520um thick silicon wafer.

	Hardbake time	Before hardbake	After hardbake	Difference	Stress of SU-8
Sample1	0min	b=7.7 µm	b=28.6 µm	20.9 µm	13Mpa
Sample2	10min	b=16.1 µm	b=55.1 µm	39 µm	24Mpa
Sample3	20min	b=-1.9 µm	b=41.5 µm	43.4 µm	27Mpa
Sample4	30min	b=-4.2 µm	b=39.2 µm	43.4µm	27Mpa

The schematic composite cantilever beam is showing in Figure 2-3. Two different materials are used in the bimorph stress beam. The heights are h_1 and h_2 , respectively. They also have the different residual stress, σ_1 and σ_2 , as well as different Young's modulus, E_1 and E_2 [28].

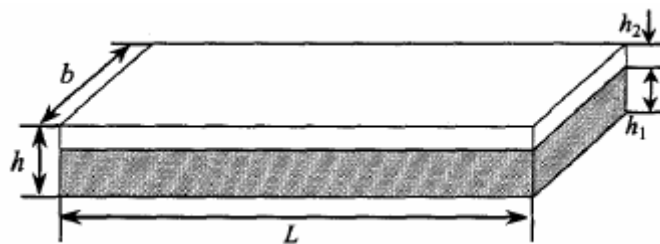


Figure 2-3: Dimensions of a cantilever beam. [28]

For the presupposition, the resultant forces, P_1 and P_2 , are produced when two different residual stresses of two films share an interface at equilibrium. They act at the center of their respective cross sections, the force and moment balance can be made, as shown in Figure 2-4 [29]:

$$P_1 = P_2 = P$$

$$P \cdot \frac{h}{2} = M_1 + M_2 = M \quad , \quad (2-1)$$

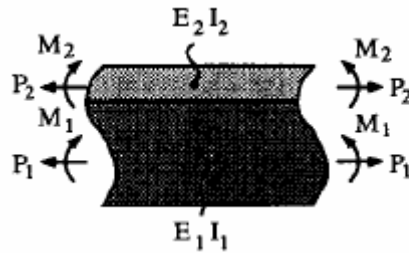


Figure 2-4 Resulting forces and moments. [29]

To calculate the moment-curvature relations for each material, an equivalent beam strength $(EI)_{equiv}$ can be defined [30, 31]

$$(E \cdot I)_{equiv} = \frac{E_2 \cdot b \cdot h_2^3}{12(1 + m \cdot n)} \cdot K \quad , \quad (2-2)$$

where

$$K = 1 + 4mn + 6mn^2 + 4mn^3 + m^2n^4 \quad (2-3)$$

$$m = \frac{E_1}{E_2} \quad \text{and} \quad n = \frac{h_1}{h_2} \quad (2-4)$$

and E_1 and E_2 are the Young's modulus of the lower film and the upper film, respectively. The relationship between the stress-induced internal force (P) and the radius of curvature (ρ) can be determined:

$$P = \frac{2 \cdot (E \cdot I)_{equiv}}{h \cdot \rho} \quad (2-5)$$

The radius of curvature (ρ) is constant along the beam, since the internal force (P) and the beam geometry do not vary.

An additional condition is that of zero slip at the interface. The strain in each

film is composed of three components: one due to the residual stresses σ_1 and σ_2 , one due to the axial force P , and one due to the curvature ρ of the beam. Setting the sum of the three components in one material equal to that of the other at the interface is that:

$$\frac{\sigma_1}{E_1} + \frac{p}{E_1 h_1 b} + \frac{h_1}{2\rho} = \frac{\sigma_2}{E_2} - \frac{P}{E_2 h_2 b} - \frac{h_2}{2\rho} \quad (2-6)$$

The radius of curvature of the pre-biased flexure is obtained by solving Eqs. (2-2), (2-5) and (2-6),

$$\frac{1}{\rho} = \frac{6(m \cdot \sigma_2 - \sigma_1)}{h \cdot E_2 (3m + K[n(1+n)^2]^{-1})} \quad (2-7)$$

With the radius of curvature known, the end deflection of the beam can be calculated from trigonometry. The deflection perpendicular to the unreleased position for a given beam length, L , with radius of curvature ρ is given by

$$\delta = \rho(1 - \cos(L/\rho)) \quad (2-8)$$

The perpendicular deflection of bimorph stress beam can be calculated by Eq (2-8) and also can be simulated by the CoventorWare simulation software. Gold is used as conductive wire and reflective mirror surface. Si_3N_4 is used as isolation layer in this thesis. Therefore, the bimorph stress beam can be composed of SCS/SU-8, SCS/ Si_3N_4 and SCS/gold structure. The material and geometric parameters of a SCS/SU-8 bimorph are $E_1 = 190\text{GPa}$ (SCS), $E_2 = 4.6\text{GPa}$ (SU-8) [27], $h_1 = 5\mu\text{m}$, $h_2 = 13\mu\text{m}$, $\sigma_1 = 0\text{MPa}$ and $\sigma_2 = 27\text{MPa}$. And the material and geometric parameters of a SCS/ Si_3N_4 bimorph are $E_1 = 190\text{GPa}$ (SCS), $E_2 = 270\text{GPa}$ (Si_3N_4) [32], $h_1 = 5\mu\text{m}$, $h_2 = 0.6\mu\text{m}$, $\sigma_1 = 0\text{MPa}$ and $\sigma_2 = 100\text{MPa}$. Finally the material and geometric parameters of a SCS/gold bimorph are $E_1 = 190\text{GPa}$ (SCS), $E_2 = 78\text{GPa}$ (gold) [32], $h_1 = 5\mu\text{m}$, $h_2 = 0.2\mu\text{m}$, $\sigma_1 = 0\text{MPa}$ and $\sigma_2 = 270\text{MPa}$. The residual stresses of gold, Si_3N_4 , and SU-8 are obtained from [14] and measurement results, respectively.

The deflections of the SU-8/SCS, Si₃N₄/SU-8 and gold/SCS residual stress beams, calculated from Eqs. (2-7), (2-8), and a SU-8/SCS residual stress beam simulated by CoventorWare, are shown in Figure 2-5. It can be seen the deflection of SU-8/SCS is higher than the others. So SU-8/SCS stress beams can provide the largest space of hinged structures. This is the reason why SU-8 is used for stress beam.

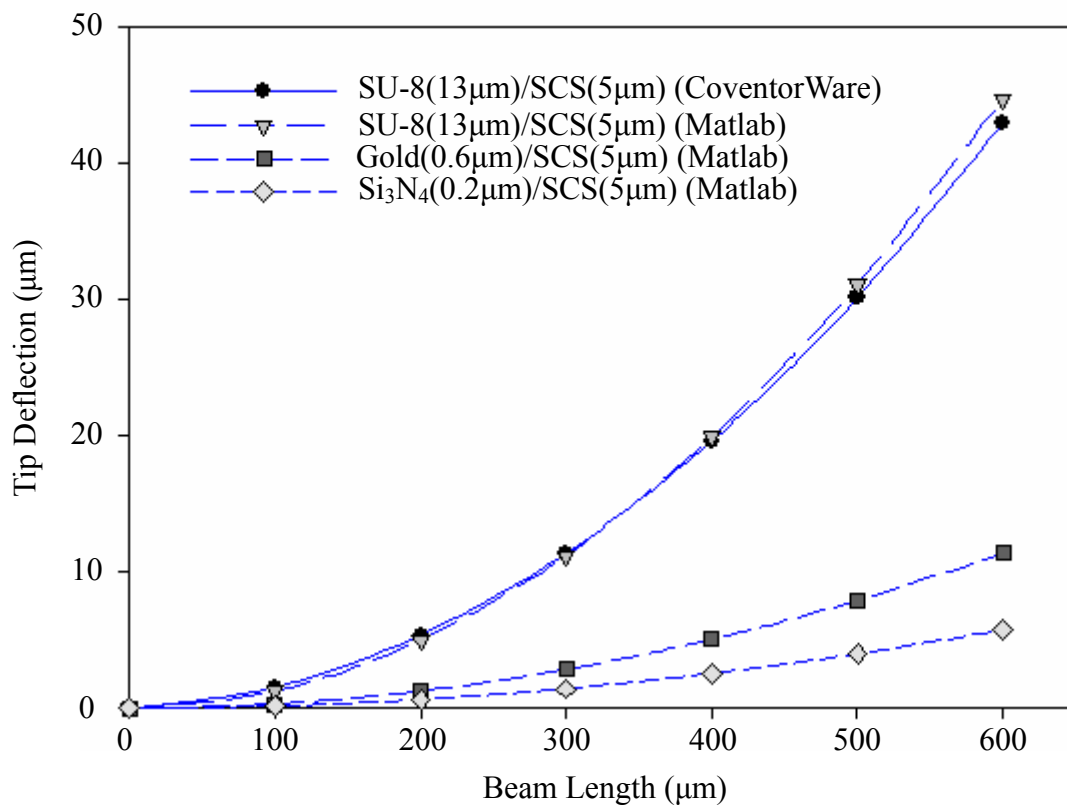


Figure 2-5: Deflection vs. beam length.

2–2–2 Solder reflow self-assembly

Some manual assistance to complete the 3D fabricated devices is still needed though the residual stress beams are used in the assembly approach. This act will increase the risk of devices fail. To solve the difficulty of assembly, the surface tension is adopted. Rising temperature until the material is melted is needed in this approach. If the solder material is used, it also can be used as the conductive material.

In this section, how the surface tension may power the out-of-plane rotation is discussed. A simple 2D model will be used to demonstrate the existence of a torque, and find the variation of torque with angle, showing that the torque will vanish at a particular angle [33].

- **2D Analysis**

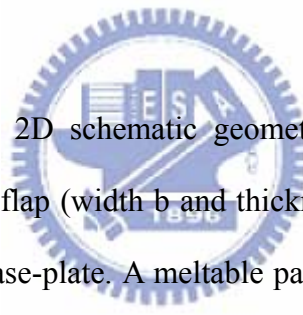


Figure 2-6(a) shows the 2D schematic geometry of the reflow material and rotation flap. Here a movable flap (width b and thickness d) is attached by a flexible hinge (width $2w$) to a fixed base-plate. A meltable pad is deposited on the hinge to a height h ; this material wets the hinge but not the surround, so that the hinge acts as a land. When the pad is melted, the free surface of melted material will deform as shown in Figure 2-6(b). At this moment, the free surface perimeter of the liquid is S . The perimeter is reduced by rotation of the hinged, as shown in Figure 2-6(c), and its decrease lowers the surface energy. The decrease in free energy may exceed the work needed to rotate the flap. The geometry will stabilize when a balance among torques is achieved. Finally, the temperature may be lowered and the pad may then be resolidified as in Figure 2-6(d).

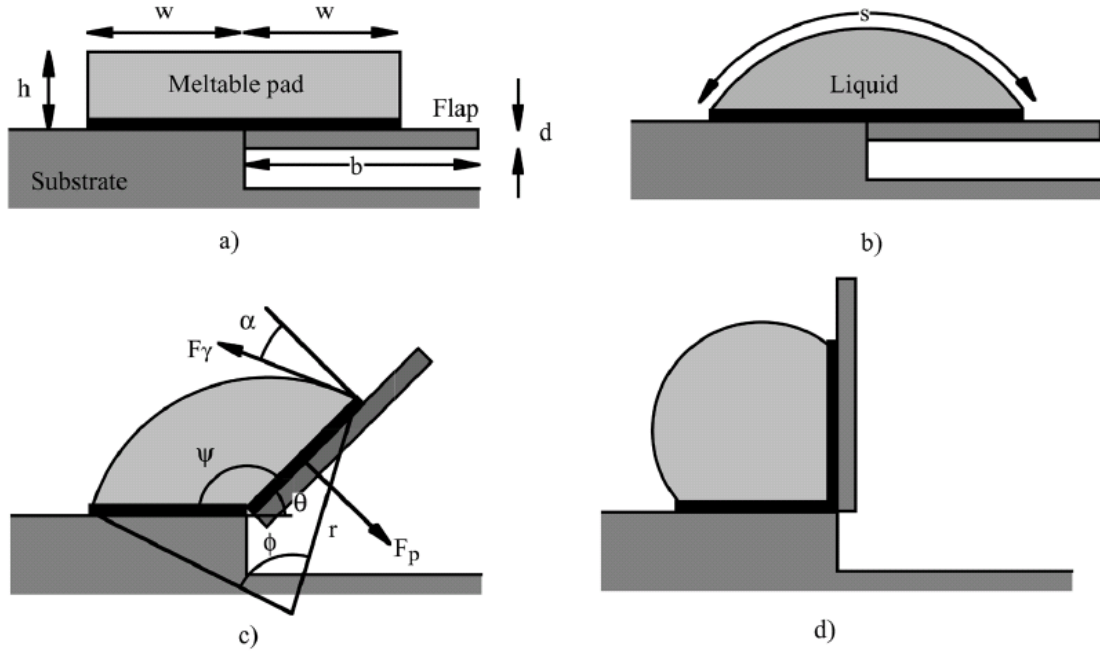


Figure 2-6: Two dimensional geometry for surface tension powered rotation [33]

Some situation should be assumed before analysis. All forces except surface tension are neglected. A cylindrical free liquid boundary is assumed with constant radius of curvature r . The geometric factors ϕ , θ and r , as shown in Figure 2-6(c), can be related by assuming the liquid is incompressible. Then the initial and final cross-sectional areas can be equated,

$$2wh = \frac{\{w^2 \sin(\theta) + \phi r^2 - r^2 \sin(\phi)\}}{2} \quad (2-9)$$

By using the factor $r \sin(\phi/2) = w \cos(\theta/2)$ and defining the normalized initial height η of the pad as $\eta = h/w$, a single equation linking ϕ and θ can be obtained,

$$\cos^2\left(\frac{\theta}{2}\right) \{\phi - \sin(\phi)\} = \sin^2\left(\frac{\phi}{2}\right) \{4\eta - \sin(\theta)\} \quad (2-10)$$

Because of the surface tension of liquid, the final equilibrium shape of the droplet is shown in Figure 2-7 for three different liquid cross-sections. In each case, the shape is an arc of a circle centered on the point O and passing through the ends of the lands (points A and B) and the hinge (point C). Because of the simple equilibrium geometry, there is a relation between the angles ϕ and ψ , namely $\phi_e = 2\psi_e$,

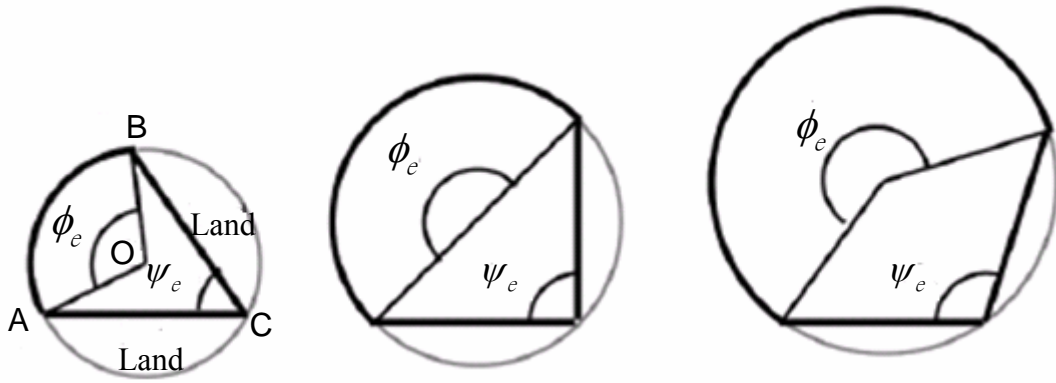


Figure 2-7: Equilibrium shapes for different final angle

where “e” means equilibrium. The value of η needed for a given θ_e can be found by substituting ϕ_e into Eqs. (2-10) to obtain

$$\eta(\theta_e) = \frac{\{\sin^3(\theta_e) + \{1 + \cos(\theta_e)\} \{\pi - \theta_e + \sin(\theta_e)\cos(\theta_e)\}\}}{4\sin^2(\theta_e)} \quad (2-11)$$

For the specific angle $\theta_e = \frac{\pi}{2}$, the normalized initial height η can be obtained

$$\eta = \frac{(2+\pi)}{8} = 0.6427$$

So the normalized height η is assumed as 0.6427 for the rotational angle, 90° .

- **Meltable material**

In general, the meltable material is photoresist [34]. But in this thesis, solder 63Sn/37Pb is used not only as the melt material but also the conductive structure.

The diameter of the solder ball is $0.1\mu\text{m}$. The volume of the solder ball can be calculated and transformed into the volume of a rectangular solid.

$$\frac{4}{3}\pi r^3 = 2whL \quad (2-12)$$

where r is the radius of the solder ball, L is the length of the rectangular solid. Figure 2-8 is the dimension of the equivalent rectangular solid of a solder ball. The width parameter w is assumed to be $50\mu\text{m}$, so the height h is fixed at $32\mu\text{m}$ because of the ratio η . Finally the length L is decided $163\mu\text{m}$ for the equivalent volume of the

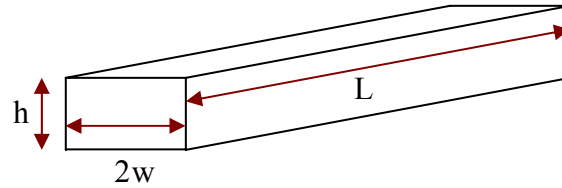


Figure 2-8: Dimension of an equivalent shape for solder ball

solder ball.

- **Mechanical limiter**

Although the above formulas can predict the rotation degree of the surface tension self-assembly type devices, they ignore a second free liquid surface existing in the gap between the fixed and moving parts. This will enable the moving parts to rotate further, as shown in Figure 2-9. The left diagram shows the ideal liquid cross section for $\theta_c = 90^\circ$. The right diagram shows the flap rotating further and opening the gap. These two shapes have the same free-boundary lengths, liquid cross-section areas, and same energy state. Thus, there is no barrier to further rotation once equilibrium has been reached. This is an important drawback, which requires the addition of mechanical limiters. For improving the rotational accuracy, a self-locking mechanism is used with the surface tension assembly approach.

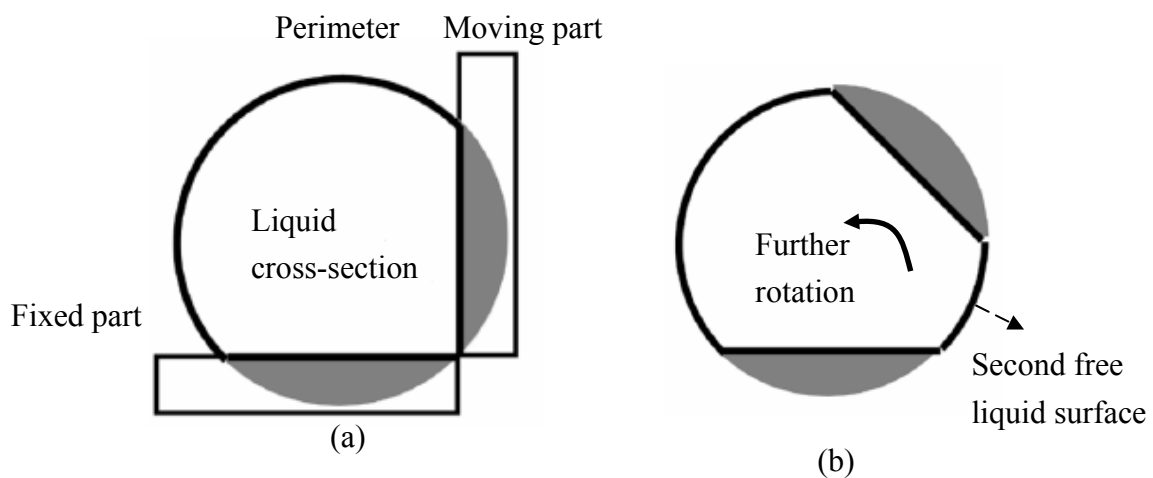


Figure 2-9: Definition of over-rotation.

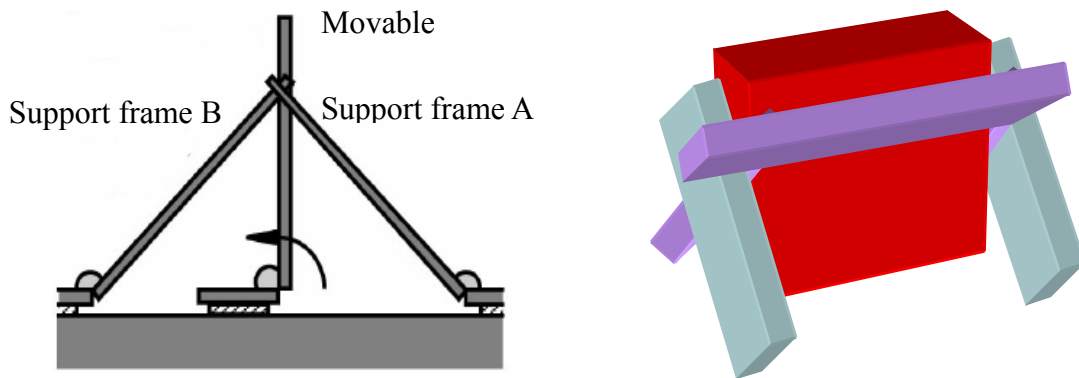


Figure 2-10: diagram of self-lacking mechanism: (a) 2D cross-section view, (b) 3D model

The simple diagram of self-locking mechanism is shown in Figure 2-10. Support frames A and B form an equilateral triangle with the substrate. And the surface tension power is also used at the rotation for support frame A and B. They rotate simultaneously in opposite directions until their extremities catch. So if the further rotation occurs, the movable part will be stopped by the support frames.

According to the above discussion, the parameters of the pad dimension and the mechanic limiter can be decided. Gold layer is used as the adhesion layer between silicon and solder ball. So the width and length are also designed as $w=50\mu\text{m}$ and $L=163\mu\text{m}$. With the help of the mechanical limiter, the rotational angle can be more accurate.

In addition to the self-assembly, the combination of the 90° mirror with photo detector can also be achieved by the solder which is used as the connective part between the diode on mirror and the electrical pad on substrate.

2-3 Optical component – Fresnel lens

There are several optical components on the optical bench. Our focus falls on the diffractive type Fresnel lens. Diffractive microlenses are very attractive for integrating with free-space microoptical bench (FS-MOB) [1]. There are two kinds of diffractive microlenses, one is the continuous kinoform lens, and another is the approximation of the kinoform lens. The continuous form relief lens can be made by direct laser writing in photoresist or patterning by gray scale masks. The approximate ones can be made by multiple-step process of binary design. The advantage of the multiple-step binary is easy to fabricate. Figure 2-11 shows the schematic of these two different types.



Figure 2-11: Schematic of (a) continuous relief of Fresnel zone plate, (b) multiple-step binary Fresnel zone plate

The binary diffractive microlens is an approximation of kinoform, or continuous form relief lens, designed by applying a phase-function constrain between 0 and 2π to subtract an integral number of wavelength from the lens transmittance function. Theoretically, a kinoform lens can achieve 100% diffraction efficiency. Multilevel lithography and stepwise etching can approximate the kinoform lens structure.

Multilevel Fresnel lenses at the expense of more complicated fabrication processes can achieve the efficiency greater than 80%. The efficiency of a binary microlens with $M=2^m$ (m is the mask number for level- m mask) phase levels is

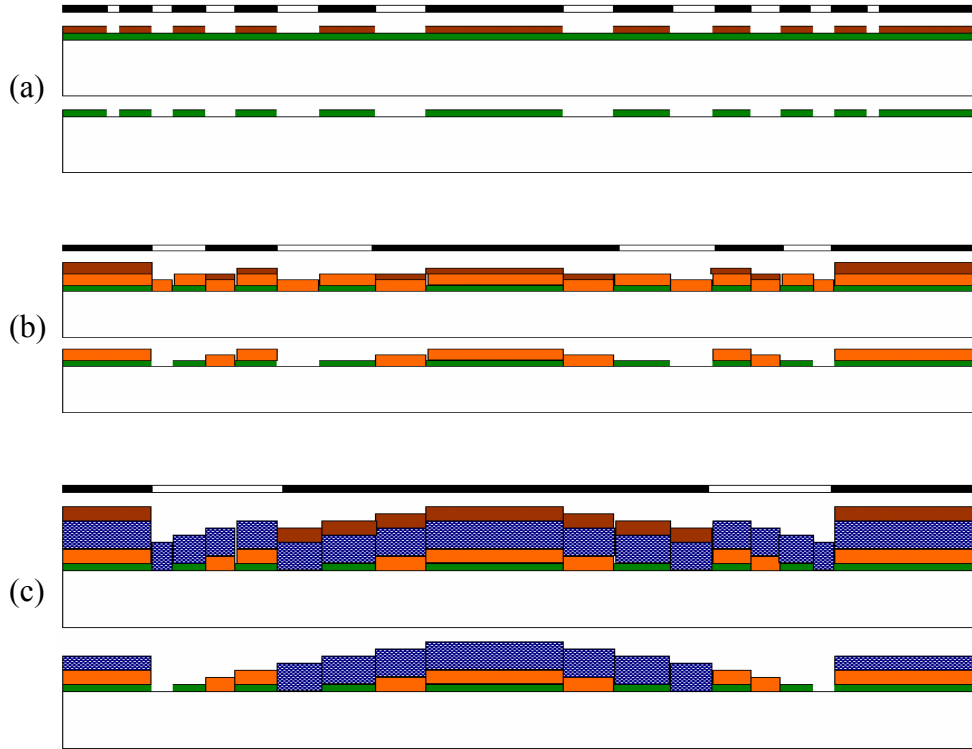
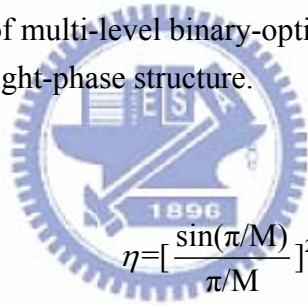


Figure 2-12: Process cycles of multi-level binary-optics microlens: (a) two-phase structure (b) four-phase structure (c) eight-phase structure.



$$\eta = \left[\frac{\sin(\pi/M)}{\pi/M} \right]^2 \quad (2-13)$$

For example, $\eta = 41\%$ for $M=2$, $\eta = 81\%$ for $M=4$, and $\eta = 99\%$ for $M=16$ [1].

Figure 2-12 shows a processing cycle for the fabrication of a two-phase, four-phase, and eight-phase microlens.

For a multilevel binary optical structure, the depth of each level (d) is defined as [35],

$$d(m) = \frac{\lambda}{(n-1)2^m} \quad (2-14)$$

where λ is the wavelength of light in free space, n is the index of refraction of the lens material, m is the mask number for the level. A m -mask process produces an $M=2^m$ step approximation to a continuous diffractive structure. Since microlens operate over a small range in incident angle, a simple planar thin-film lens is

acceptable. The optical path difference (OPD) function for each lens is used to derive the following relationship among the zone radius, focal length, and wavelength [35],

$$r(p,m)=\left[\left(\frac{p\lambda}{n2^m}\right)^2+2f\left(\frac{p\lambda}{n2^m}\right)\right]^{1/2} \quad (2-15)$$

where f is the focus length, $p=0, 1, 2\dots$ is the ring number, n is the index of refraction of the lens material, and $r(p,m)$ gives the successive zone radius for the patterns in mask number m .

In this thesis, the simplest two-phase binary Fresnel lens is used. The odd annular rings are adopted in the mask design. Silicon nitride (Si_3N_4) and SU-8 are used as the lens materials, respectively. The focal length (f) of silicon nitride lens is $2500 \mu\text{m}$, and the index of refraction, $n=2.1$. The parameters in SU-8 Fresnel lens are, $f=3000 \mu\text{m}$ and $n=1.6176$. The other parameters are, wavelength of red laser $\lambda=632\text{nm}$, mask number $m=2$. Figure 2-13 is the layout of the two Fresnel lenses. In the layouts, the four bars support and link the rings.

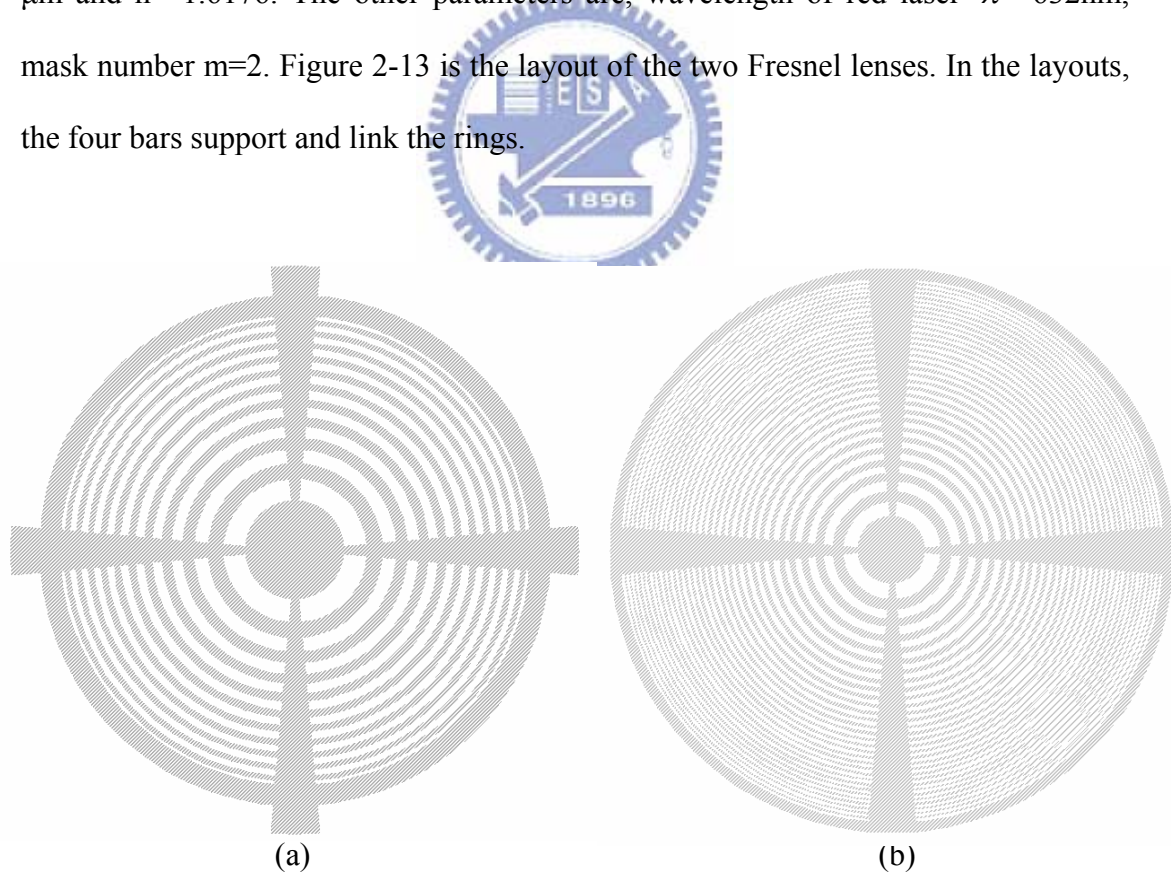


Figure 2-13: Mask of Fresnel lens (a) SU-8, (b) silicon nitride

2-4 Integrated devices

The MEMS based free-space optical bench is composed of grating, polarizing beam splitter(PBS), 45° reflective mirror, Fresnel lens, and photo detector. Figure 2-14 shows the layouts of the bench with different assembly approaches. At the grating, the incident light is diffracted into three beams for reading and tracking. After passing through the PBS, the light is then reflected by the 45° mirror to read data. After reading data, the light with data information reflective by 45° mirror again. This reflective optical data is then reflected by the PBS and focused by the Fresnel lens onto the photo diode array. Those optical components are all mounted on the pop-up single crystal silicon structure. The area of a bench is $8.5 \times 8.5 \text{ mm}^2$.

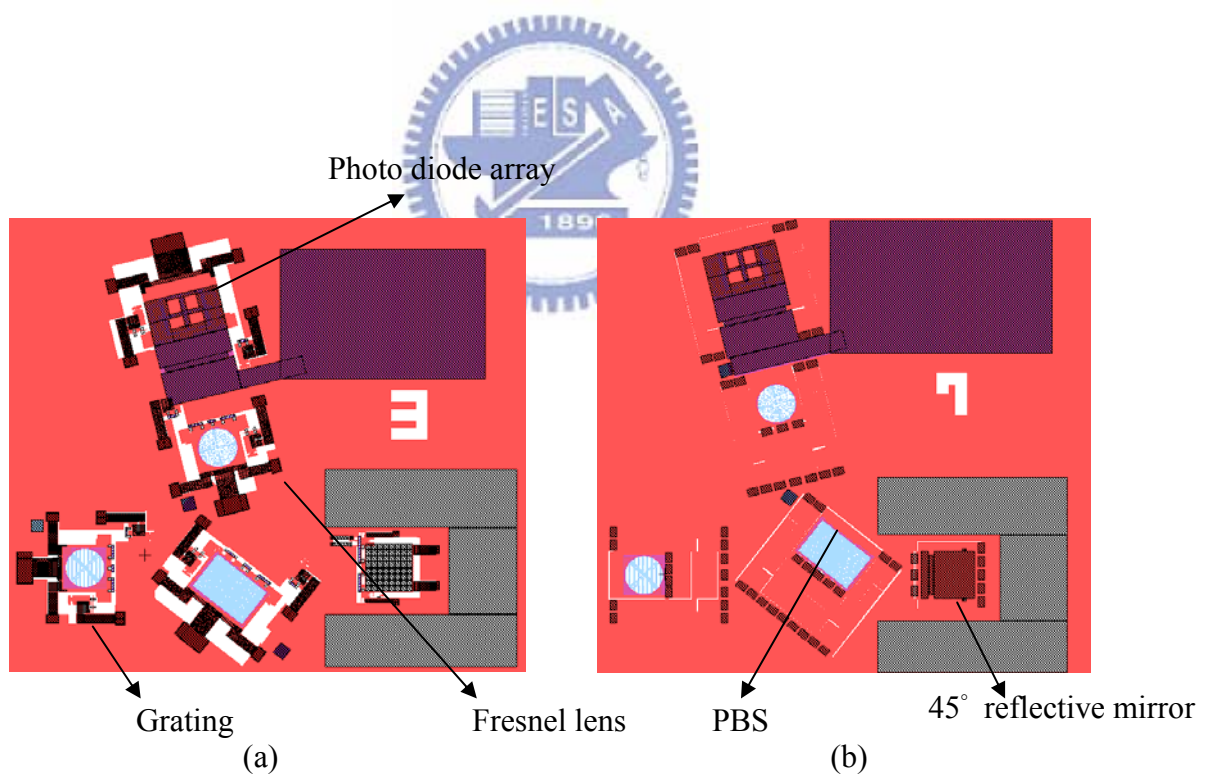


Figure 2-14: Layout of the optical bench- (a) Stress beam assembly, and (b) Surface tension assembly.

2-5 Summary

SU-8 is chosen as the top layer of bimorph stress beam because it can provide a higher deflection distance than Gold and silicon nitride. And the solder for assembly provides not only a self-assembly approach but also a connective part. Several optical elements and photo detector are integrated together as a basic optical bench system. The silicon nitride is a common material for optical elements, but SU-8 can be a new attempt. In the following chapter, the fabrication process will be discussed.



Chapter 3

Fabrication Process

In this chapter, a novel surface micromachining-like fabrication process is used to integrate SOI and SU-8 in an optical bench, including grating plate, beam splitter, reflective mirror, Fresnel lens, and photo-detector. Using SOI wafer can simplify the process flow. The optical components are made not only in silicon nitride but also by SU-8. The optical bench assembled by bimorph stress beams is discussed in first part. The second part discusses the process for surface tension by melting solder ball. Finally, some phenomena and problems will be discussed.



3-1 Optical bench – integration of SOI and SU-8

Flatness is an important issue for optical components. Since the SCS layer almost has no stress, it can provide a flat surface for the optical purpose. Therefore, the basic structures of the bench are defined on the device layer of SOI substrate. The silicon nitride layer is an isolation layer for conducting wires and separates the p^+ and n^+ regions of photo diode. In addition, it is commonly used as an optical material. Silicon oxide is a sacrificial layer. Gold is the material for conductive wires and reflective mirror. Finally, SU-8 is used for the bimorph stress beam and anchor structure. Furthermore, it also can be used as the optical elements. Figure 3-1 is a schematic of the cross-section of a completed device, including the photo detector, 135° reflective mirror and an optical element.

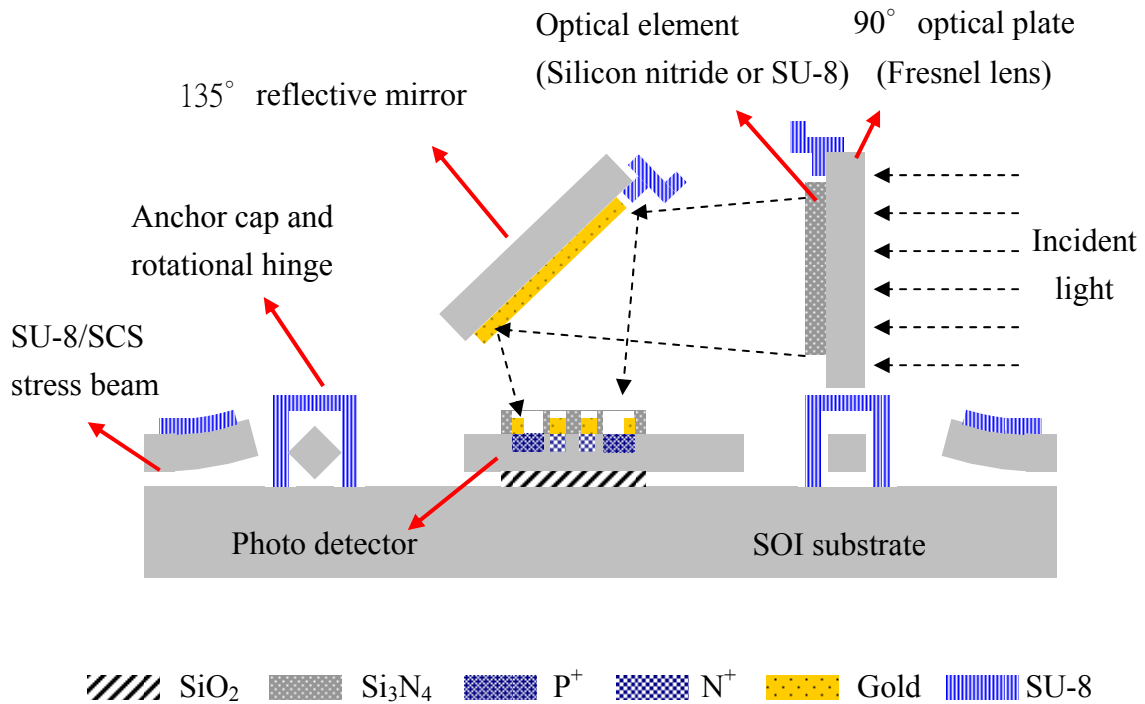


Figure 3–1: Schematic of structures and materials

Most fabrication processes were executed in the Nano Facility Center at National Chiao Tung University. The process flow is showed in Figure 3-2. The detailed parameters of the process will be described later.

Process Flow

Step (A): The device layer (resistivity: 1-10 ohm-cm, thickness: 5 μm) of SOI wafer was pattern by photolithograph. The main device structure was defined by inductively coupled plasma reactive ion etching (ICP DRIE). (Mask #1)

Step (B): low stress Si₃N₄ was deposited by Low Pressure Chemical Vapor Deposition (LPCVD) and patterned by reactive ion etching (RIE). (Mask #2)

Step (C): Boron (B) was implanted for the P⁺ region of the photo detector.

Step (D): Si₃N₄ was patterned by RIE again. Then arsenic (As) was implanted for the N⁺ region of the photo detector. (Mask #3)

Step (E): SiO₂ was deposited by Plasma Enhanced Chemical Vapor Deposition (PECVD). Aluminum was deposited on SiO₂ by thermal coater. They were patterned by High Density Plasma RIE (HDP-RIE) respectively. (Mask #4)

Step (F): Aluminum and SiO₂ were pattern by HDP-RIE again. (Mask #5)

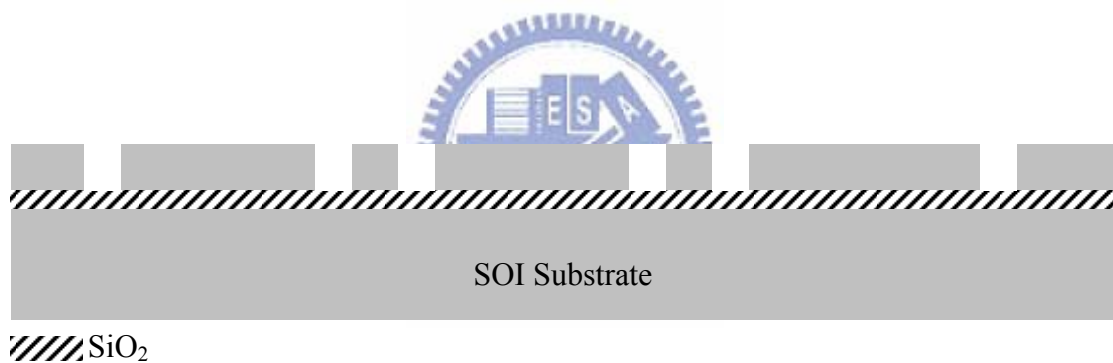
Step (G): Photoresist AZ4620 was coated and patterned for the following lift-off step. (Mask #6)

Step (H): Gold was sputtered by DC Sputter system.

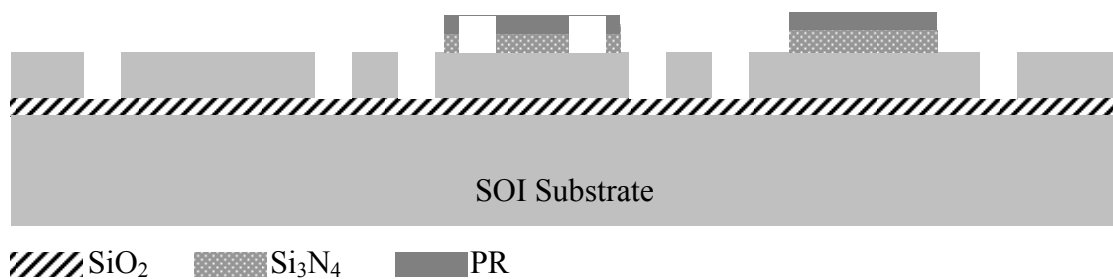
Step (I): Photoresist was removed by acetone. Au is patterned by lift-off.

Step (J): SU-8 was coated and patterned. (Mask #7)

Step (K): SiO₂ was etched by HF. The structures were released by HF vapor.

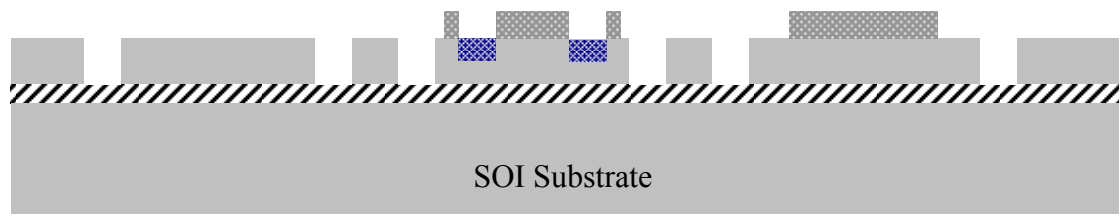


(A) Device layer of the SOI wafer patterned by photolithograph; main device structure defined by ICP DRIE (Mask # 1)



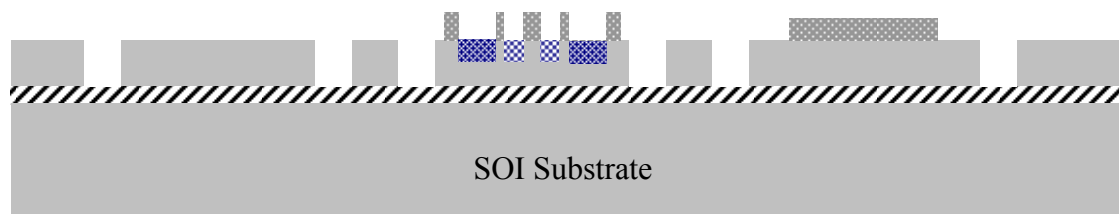
(B) Low stress Si₃N₄ deposited by LPCVD and pattern Si₃N₄ by RIE (Mask # 2)

Figure 3–2: Fabrication process of the optical bench with stress beam.



/// SiO₂ Si₃N₄ P⁺ region

(C) P⁺ region of the photo detector ion implanted (B); photoresist removed



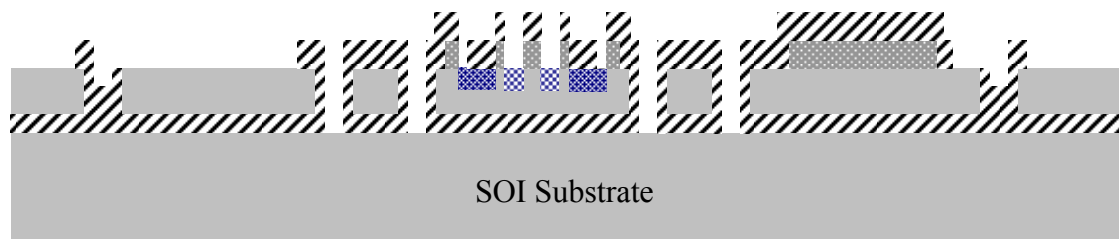
/// SiO₂ Si₃N₄ P⁺ region N⁺ region

(D) Si₃N₄ patterned by Poly-RIE; N⁺ region ion implanted (As); photoresist removed
(Mask # 3)



/// SiO₂ Si₃N₄ P⁺ region N⁺ region Al

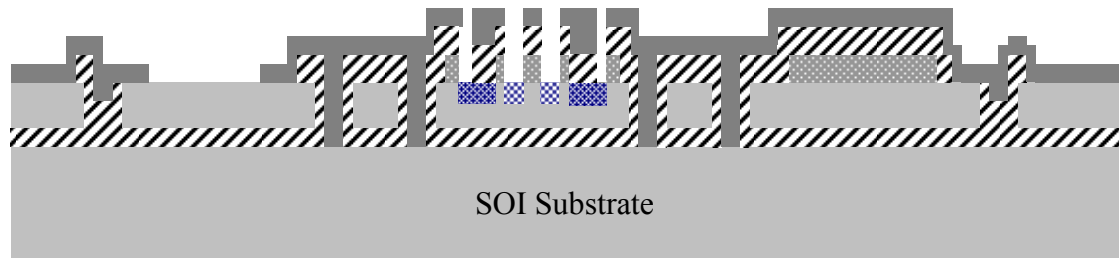
(E) SiO₂ deposited by PECVD and aluminum deposited by thermal coater; aluminum and SiO₂ patterned by HDP-RIE; photoresist removed
(Mask # 4)



/// SiO₂ Si₃N₄ P⁺ region N⁺ region

(F) Aluminum and SiO₂ patterned by HDP-RIE; aluminum and photoresist removed
(Mask # 5)

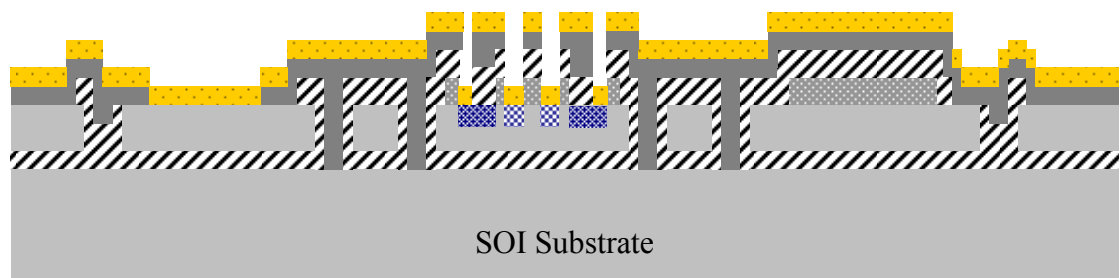
Figure 3-2: Fabrication process of the optical bench with stress beam (continued).



SiO₂
 Si₃N₄
 P⁺ region
 N⁺ region
 PR

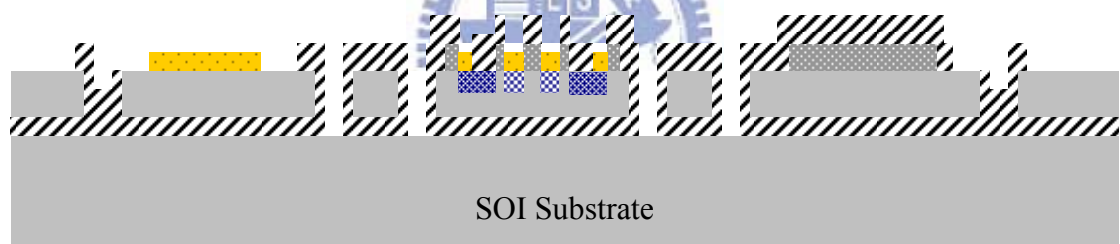
(G) Photoresist AZ4620 coated and patterned

(Mask # 6)



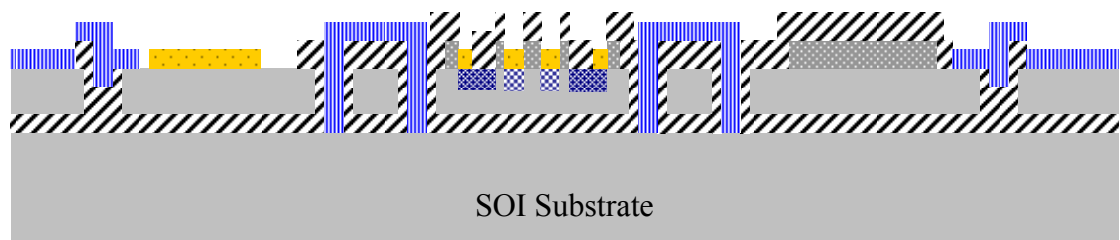
SiO₂
 Si₃N₄
 P⁺ region
 N⁺ region
 PR
 Au

(H) Gold sputtered by DC Sputter system



SiO₂
 Si₃N₄
 P⁺ region
 N⁺ region
 Au

(I) Photoresist removed; gold patterned by lift-off

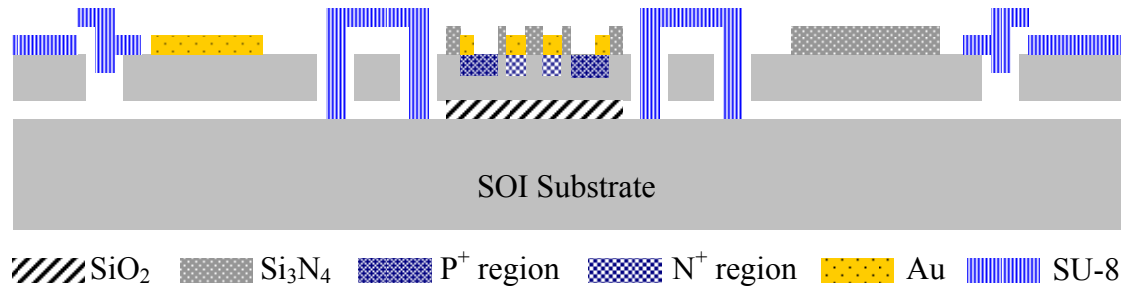


SiO₂
 Si₃N₄
 P⁺ region
 N⁺ region
 Au
 SU-8

(J) SU-8 coated and patterned

(Mask # 7)

Figure 3-2: Fabrication process of the optical bench with stress beam (continued).



(K) Sacrificial layer SiO₂ etched; structures released by HF vapor

Figure 3–2: Fabrication process of the optical bench with stress beam (continued).

3–1–1 Fabrication technology

In this section, the detailed fabrication parameters of the above process are described. A standard RCA clean process was first performed on the bare SOI wafer. In the first step, the photoresist FH6400 was spin coated on the bare SOI wafer with the recipe of spread cycle speed = 1000 rpm for 10 seconds and spin cycle speed = 4000 rpm for 30 seconds. After exposure and development of the photoresist, ICP DRIE was used to anisotropically etch the 5 μm -thick single crystal silicon of the SOI device layer. The photoresist was used as the etching mask. The main structures, including the frame of the optical components and reflective mirror surfaces, were defined in this step. The photoresist can then be removed by acetone in a shaker or immersing in H₂SO₄. Before depositing low stress silicon nitride, the SOI wafer was dipped in HF solution. The native oxide on the device layer can be removed by HF. Then a 0.6- μm -thick low stress Si₃N₄ was deposited by LPCVD with the recipe of NH₃ flow rate = 17 sccm, SiHCl₂ flow rate = 85 sccm, temperature = 850°C and pressure = 180 mTorr. It took 75 minutes to deposit this thin film. After deposition, HMDS was coated on the surface of the Si₃N₄ layer. HMDS can strengthen the adhesion between photoresist and Si₃N₄, SiO₂, or metal. Next the AZ4620 photoresist was spin coated with the recipe of spread cycle speed = 1000 rpm for 10 seconds and

spin cycle speed = 3500 rpm for 30 seconds, followed by exposure and development. It was used not only as a mask for the P⁺ ion implantation but also for the optical elements, such as grating, polarize beam splitter and Fresnel lens. RIE of Si₃N₄ defined the P⁺ implantation region and the optical elements.

The implantation process was performed at National Nano Device Laboratories. Boron was used to form the P⁺ region in the n-type device layer. The implantation energy was 15 keV and the concentration of dopant is $5 \times 10^{14} \text{ cm}^{-2}$. Photoresist was removed subsequently. The sample was then annealed at 900°C for 10 sec to activate the dopants. The N⁺ region was also defined by the photolithography of AZ4620 and RIE of Si₃N₄. Arsenic was the dopant for the N⁺ region. The implantation energy was 60 keV, and the concentration of dopant was $5 \times 10^{15} \text{ cm}^{-2}$. The photoresist was then removed. Then the sample was annealed at 900°C for 15 sec to activate the dopants. Sometimes, it was not easy to remove the photoresist by ACE or H₂SO₄ because it was burned during the implantation process. In such cases, O₂ plasma can be used to remove the burned photoresist.

In the next step, 3- μm -thick SiO₂ was deposited by PECVD on the top side of the SOI wafer. This is a sacrificial layer for the free rotation space in the anchor. Aluminum was coated on this SiO₂ layer as the etching hard mask. The deposition time of the 3- μm SiO₂ layer with 400 sccm O₂ and 10 sccm tetraethoxysilane (TEOS) at 300°C, 300 mTorr chamber pressure and 200 W RF power was about 13 minutes. 5000-Å-thick Al was then deposited by thermal evaporation. Before deposition, clean and dipping in Buffered Oxide Etchant (BOE) was necessary. After coating and patterning with AZ4620, aluminum was etched by HDP-RIE with the recipe of 35 sccm BCl₃, 35 sccm Cl₂, 10 mTorr chamber pressure, 750 W ICP RF power and the etching time is 50 seconds. Subsequently, photoresist was removed and the 5 μm -thick SiO₂, 3 μm PECVD oxide layer and 2 μm -thick thermal oxide of SOI, were also

etched by HDPRIE. The etching time of 5 μm oxide with the recipe of 40 sccm CHF_3 , 40 sccm Ar, 10 mTorr chamber pressure and 750 W ICP RF power is about 30 minutes. The position of anchor cap is defined in this step.

In the following step, the aluminum remained from the last step was patterned again with AZ4620 as the hard mask. The 3- μm -thick PECVD SiO_2 was then etched with the same recipe as the last etching and the etching time was about 18 minutes. Windows of contact of the SOI device layer with gold and with SU-8 were opened in this step.

After coating and patterning of AZ4620 again, chromium (300 \AA) and gold (1000 \AA) were deposited by DC sputtering. Chromium was an adhesion layer between silicon and gold. Then, the photoresist and unwanted metal atop the photoresist were removed in an acetone bath. Note that it was necessary to dip the wafer in diluted HF solution before depositing the gold and its adhesion layer, chromium. Otherwise, the gold layer may be deposited on the native oxide and may peel off after releasing devices.

SU-8 was spin-coated and patterned used in the next step with the recipe of spread cycle speed = 500 rpm for 5 seconds, spin cycle speed 3000 rpm for 30 seconds, pre-bake at 65 $^\circ\text{C}$ for 1 minute and soft bake at 95 $^\circ\text{C}$ for 2 minutes. The exposure time was 4 seconds, and post exposure bake at 65 $^\circ\text{C}$ for 1 minute and 95 $^\circ\text{C}$ for 2 minutes. The development time in SU-8 developer was 3 minutes and hard bake time was 20 minutes at 200 $^\circ\text{C}$. In the next step, devices were released when the sacrificial oxide layer was removed by the vapor of 49% HF solution and rinsed in IPA. The final assembly was done by probe with manual operation.

3–2 Fabrication process of self-assembly by surface tension

The failure of manual assembly in the above process is a big problem. To avoid manual operation, the surface tension self-assembly is introduced in the fabrication process. It also simplifies the process because the sacrificial layer can be canceled, as discussed in the following.

Figure 3-3 shows the diagram of the fabrication process. Step (A) to (D) were the same as for the process with stress beam. The sacrificial oxide layer deposition was eliminated. Gold was deposited and patterned by lift-off in steps (E), (F) and (G). The gold layer was used not only as the conductive wire and reflective surface but also the adhesion layer between silicon and solder.

In the next step (H), solder ball should be pressed first. The flat solder was then put on the adhesion pad of gold and pre-melted.

In the final step (I), the sacrificial layer SiO_2 was removed first by HF vapor. Solder was then melted again. Structures were assembled by the surface tension when solder was melted.

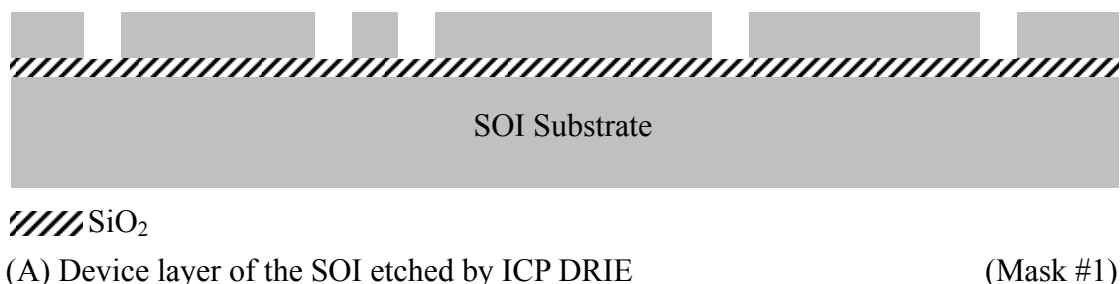
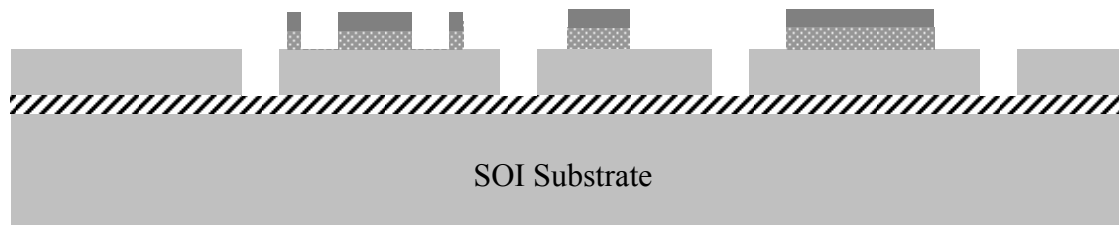
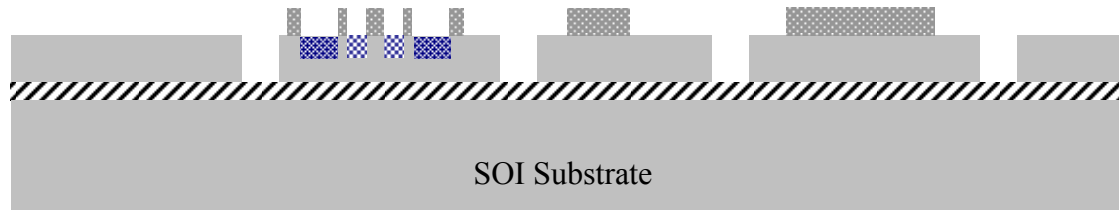


Figure 3–3: Fabrication process of the optical bench with surface tension.



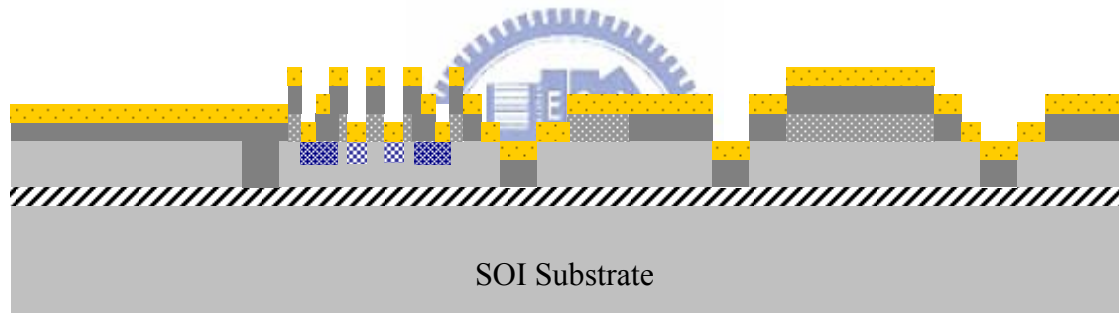
/// SiO₂ ··· Si₃N₄ ■ PR

(B) Low stress Si₃N₄ deposited by LPCVD; Si₃N₄ patterned by RIE (Mask #2)



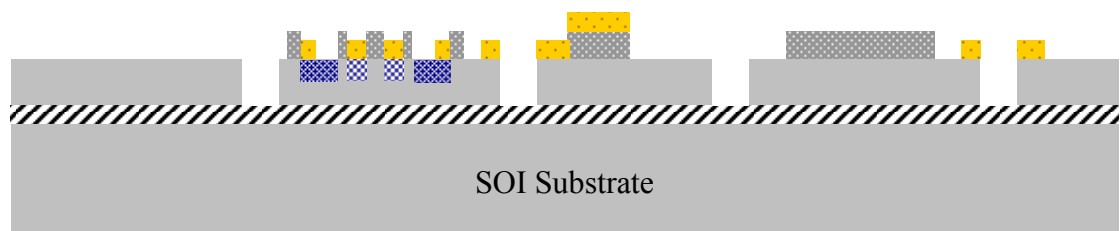
/// SiO₂ ··· Si₃N₄ ■ P⁺ region ■ N⁺ region

(C) and (D) P⁺ region ion implanted (B); remove photoresist; Si₃N₄ patterned by RIE; N⁺ region ion implanted (As); remove photoresist. (Mask #3)



/// SiO₂ ··· Si₃N₄ ■ P⁺ region ■ N⁺ region ■ PR ■ Au

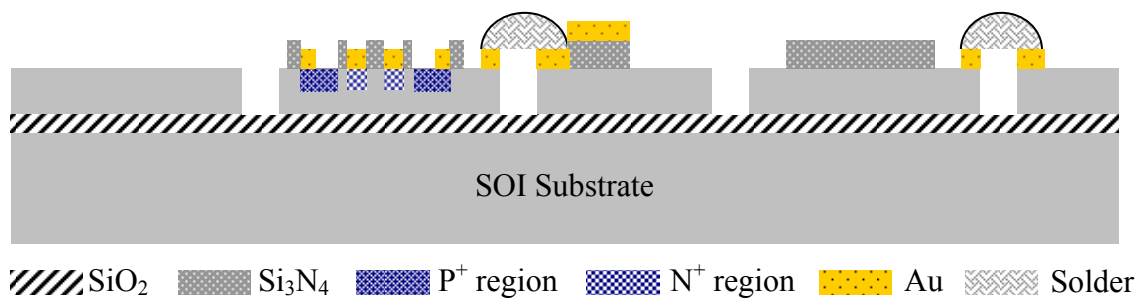
(E) and (F) Photoresist AZ4620 coated and patterned; gold sputtered by DC Sputter system (Mask # 4)



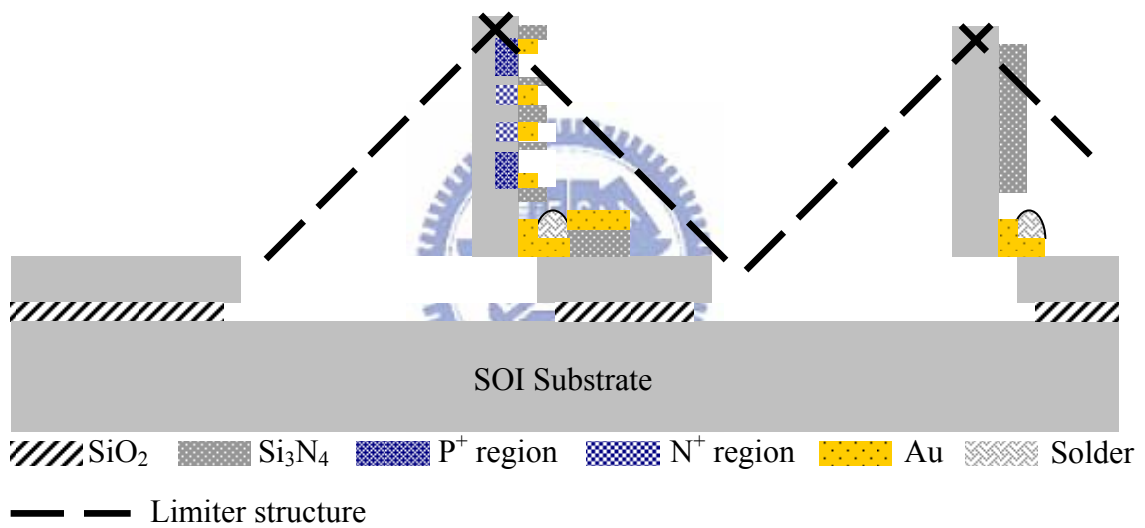
/// SiO₂ ··· Si₃N₄ ■ P⁺ region ■ N⁺ region ■ Au

(G) Photoresist removed; gold patterned by lift-off.

Figure 3–3: Fabrication process of the optical bench with surface tension (continued).



(H) Solder ball placed on pad and pre-melted.



(I) Sacrificial layer SiO_2 etched; release structure by HF vapor; solder melted again; structure assembled by surface tension.

Figure 3-3: Fabrication process of the optical bench with surface tension (continued).

The two processes are compared in Table 3-1. The solder reflow uses only five masks. This really eliminates some complicated steps.

Table 3-1: Comparison of the two fabrication processes.

	Purpose of stress beam assembly	Purpose of self-assembly
Mask 1	Device layer of the SOI wafer; frame of optical elements, reflective mirror surfaces, and stress beams	Device layer of the SOI wafer; frame of optical elements, reflective mirror surfaces, and stress beams
Mask 2	Si ₃ N ₄ ; optical elements, isolation layer, and P ⁺ region	Si ₃ N ₄ ; optical elements, isolation layer, and P ⁺ region
Mask 3	Si ₃ N ₄ ; N ⁺ region	Si ₃ N ₄ ; N ⁺ region
Mask 4	Aluminum and SiO ₂ ; position of anchors	
Mask 5	Aluminum and SiO ₂ ; contact region of the SOI device layer with gold and with SU-8	
Mask 6	Gold; lift-off	Gold; lift-off
Mask 7	SU-8; anchor, stress beam, and optical elements	SU-8; optical elements
Release	Release and assembly by manual	Pre-melt, release, and reflow again for assembly

3-3 Problems and discussions about fabrication process

Some problems and phenomena occurred in the fabrication processes. They are discussed in this section.

(1) Photolithography of Si_3N_4 optical element

In the second mask step, thin Si_3N_4 film was pattern for the Fresnel lens. The Fresnel was composed of concentric rings. The innermost ring had the largest width and the width of rings decreased progressively. It means that the width of the outermost ring can be very small. Further, there were many release holes on the frame and reflective mirrors. The depth of these release holes was 5 μm . After the release hole was opened, Si_3N_4 was deposited by LPCVD with good step coverage, as shown in Figure 3-4. When photoresist was next spin coated on the wafer, the release hole was filled with photoresist. If a 2- μm -thick photoresist AZ4620 was spin coated on the top surface, the exposure time for the 2- μm -thick photoresist was not enough to exposure the photoresist in holes. The window of release holes was not opened after Si_3N_4 RIE because there was photoresist remaining in the hole, as shown in Figure 3-4 (a). This is a problem at the releasing step. Extending the exposure time is a direct solution to remove the residual photoresist in the hole. The outer rings of the Fresnel lens were etched, as shown in Figure 3-5. The line width was decreased by the over exposure, so the outer rings disappeared. Another problem in this step was that the area of release hole was reduced due to the Si_3N_4 on the side wall, as shown in Figure 3-4 (b). Negative photoresist can be used in this photolithography to solve this problem.

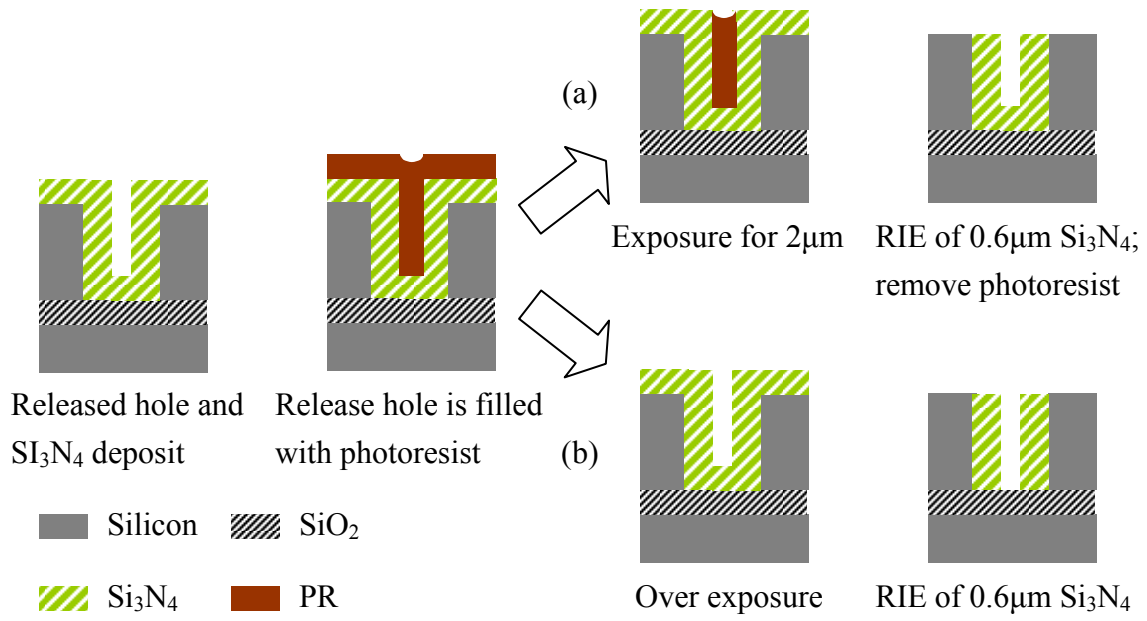


Figure 3-4: Problems in Si_3N_4 etching: (a) covered release hole (b) narrowed release hole

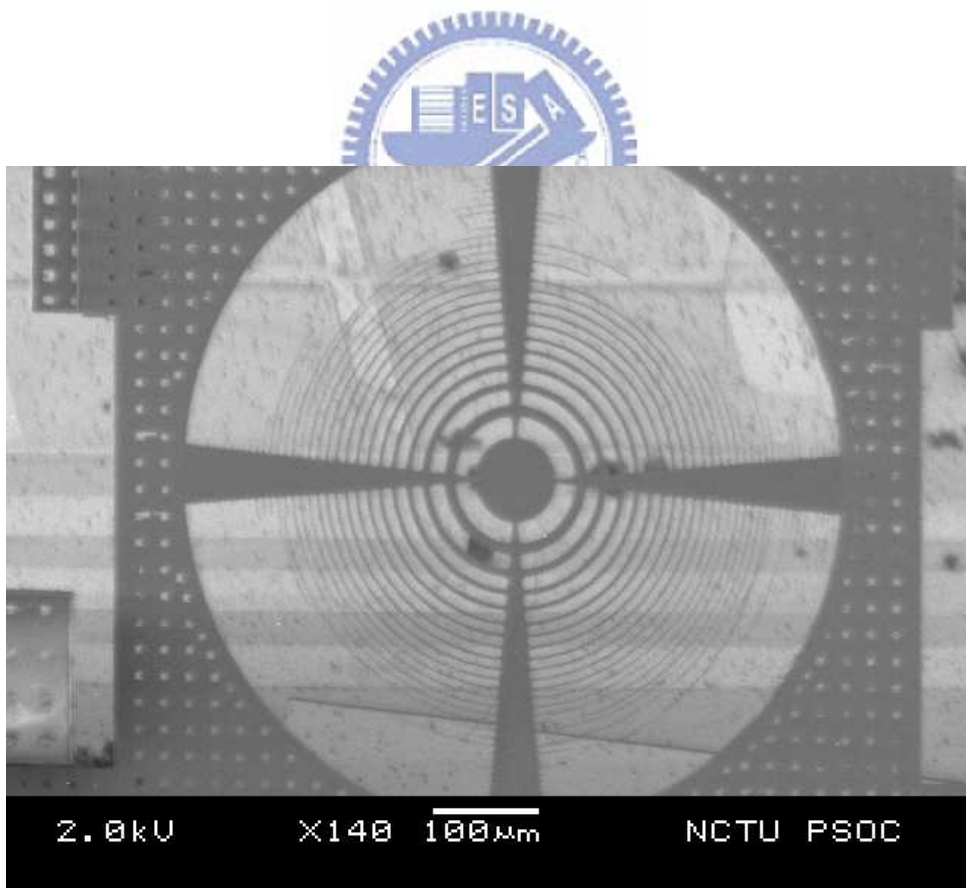


Figure 3-5: Disappearance of the outer rings

(2) Aluminum hard mask

In the step of Mask 4, photoresist was first used as the RIE mask. The etching time of the 5- μm -thick SiO_2 were long and the photoresist mask would also be etched. So, the photoresist must be very thick. The thick-film photoresist AZ4620 would collapse during hard bake, as showing in Figure 3-6. This would cause the non-vertical shape and reduce sacrificial oxidation thickness. The free rotational spaces for the hinge were therefore reduced, as shown in Figure 3-7. If aluminum is used as the hard mask, the vertical shape will be retained, as shown in Figure 3-8.



Figure 3-6: The shapes of PR before and after hard bake

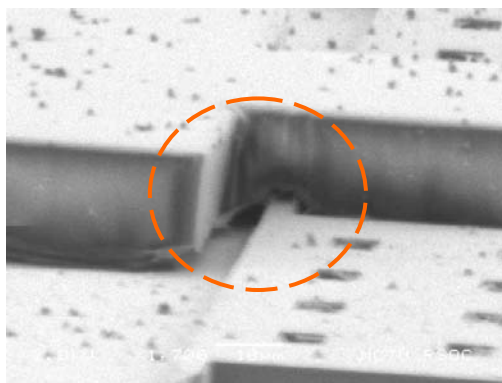


Figure 3-7: Non-vertical and reduced hinge rotational space.

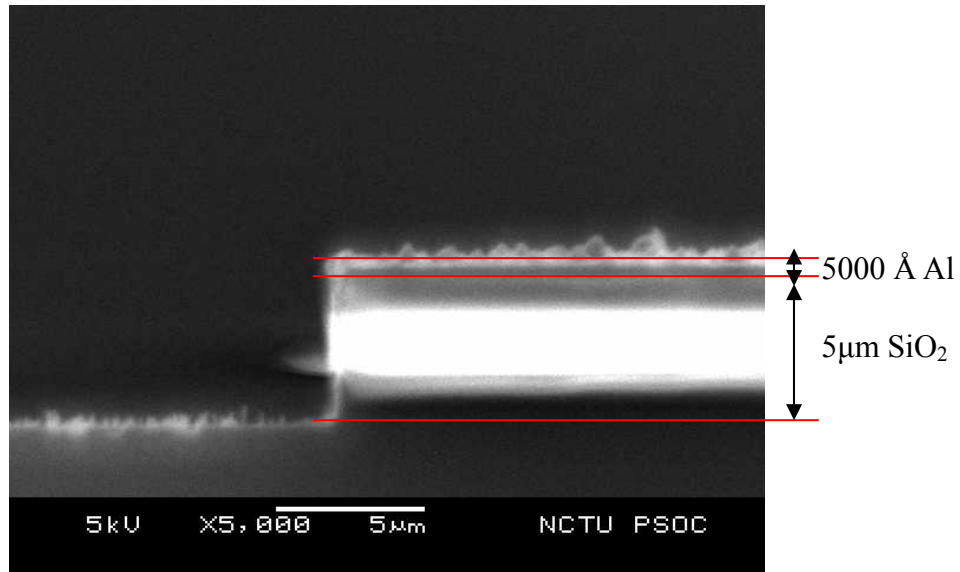


Figure 3-8: Vertical shape for 5 μ m-thick SiO₂ etching.

(3) Over etching silicon oxide in the step of Mask 5

In the Mask 5 step, silicon oxide is etched to open the silicon region for gold and SU-8 contact. So, it is very important to remove the silicon oxide completely to prevent the SU-8 and gold layer from peeling off at the releasing step. But the RIE etches not only silicon oxide but also silicon. If silicon surface is etched, the shallow ion implantation for contacts and photodiodes will be affected. This problem can be avoided by a two-step etching process. The RIE process first etches silicon oxide for almost 3 μ m, and then the wafer is dipped in diluted HF solution to etch the remaining oxide.

However, the etching time is hard to control. Therefore, the solder reflow self-assembly is investigated to avoid the use of the sacrificial oxide layer, as will be discussed in the next section.

(4) Solder ball self-assembly process

To use the solder ball for self-assembly, solder balls were pressed first and then

put on the pad with the flux to improve the adhesion between the solder and the gold. Flux can etch the oxide on the solder to enhance the electrical conductivity. Solder covered and stuck to the pad after pre-melt at 240°C with flux, as shown in Figure 3-9. The flux was removed by water after pre-melt, as shown in Figure 3-9 (b). But some of the flux mixed in the solder may be an impurity for this assembly.

Although the adhesion problem can be solved by flux, the released devices still did not lift-up during the final melt, as shown in Figure 3-10. They may have two reasons. First is the stiction of the large plate structure. Second is the shape of melted solder ball. Stiction can be improved by CO₂ dryer or back-side etching. But the non uniform solder shape after melting is the most important problem, as shown in Figure 3-11.

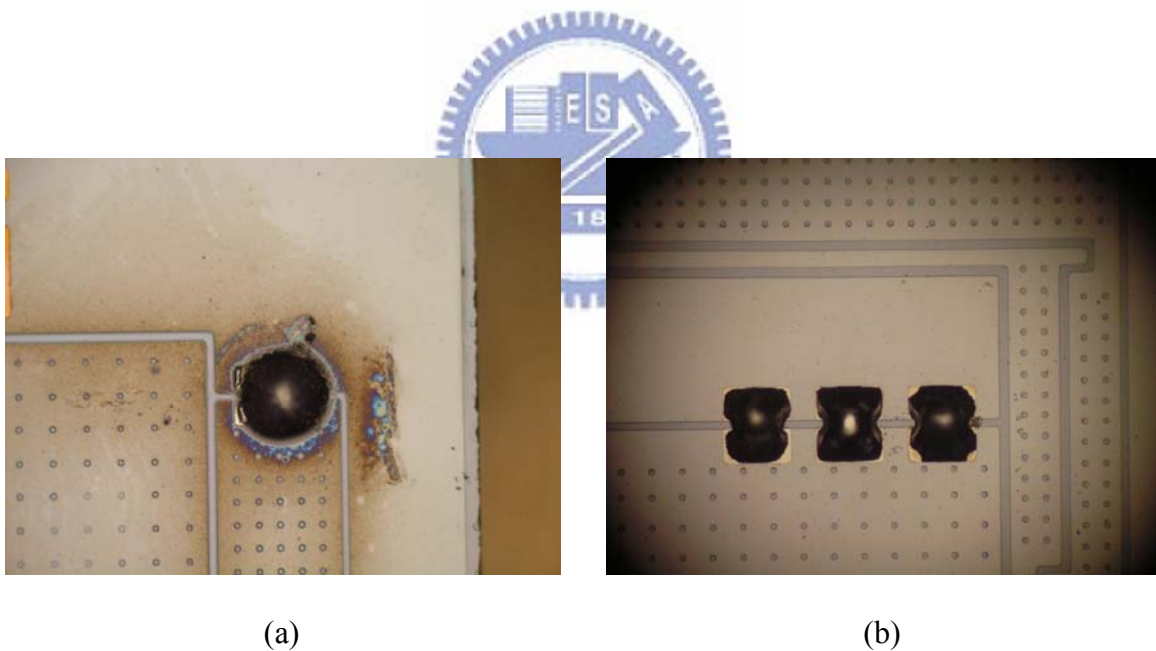


Figure 3-9: Solder ball place on gold pad (a) pre-melt with flux, (b) clean by water

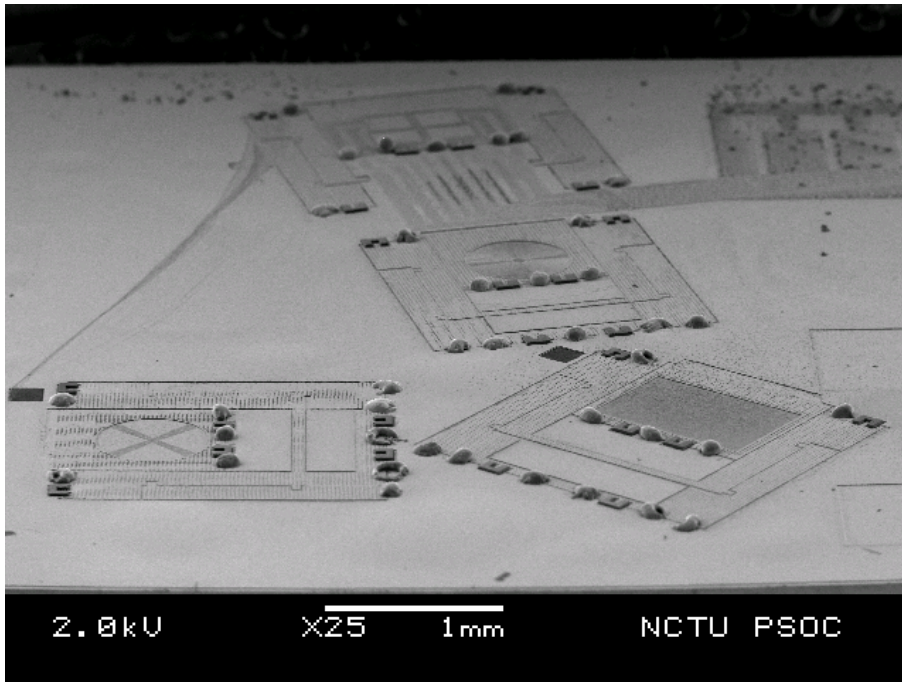


Figure 3-10: Assembly is failure after solder melt

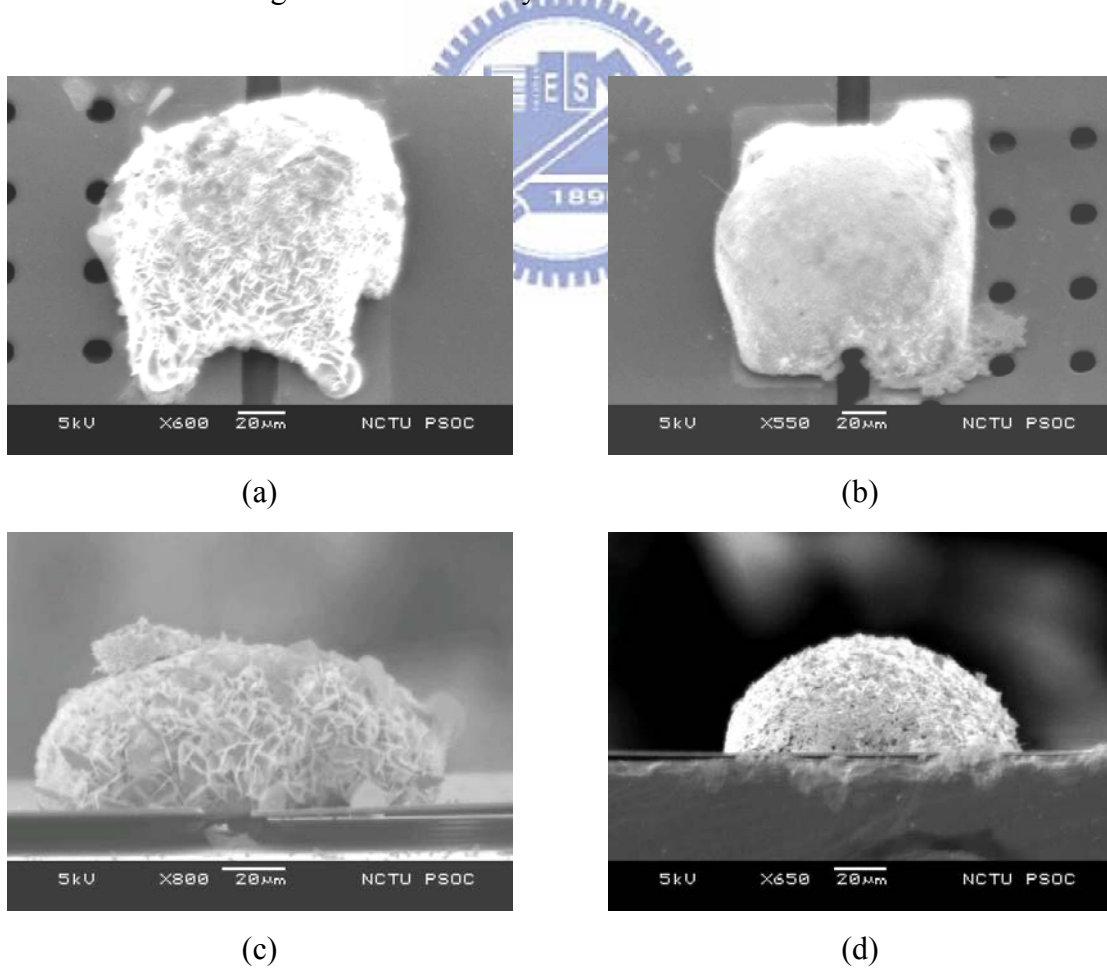
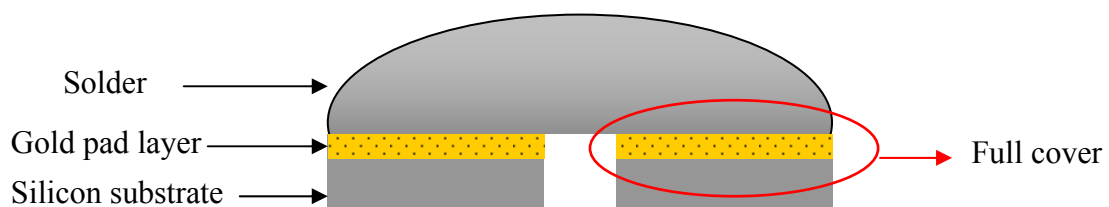


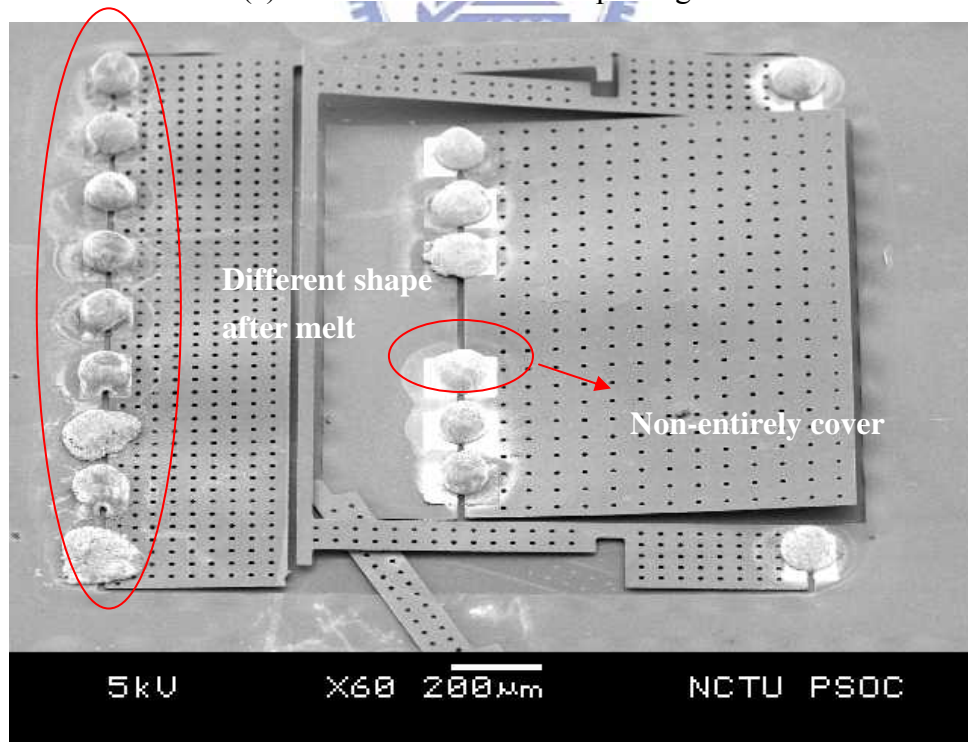
Figure 3-11: (a) and (b) are the different shapes discovered on the same chip. (c) and (d) are the cross section view of (a) and (b).

The melted solder should be able to cover the full pad and has an arc shape, as shown in Figure 3-12 (a). In the experiment, the pad was not entirely covered by the solder, as shown in Figure 3-12(b).

The power of rotation is the surface energy of solder in this assembly approach. The surface energy of solder should be translated into the work to rotate the plate. The device was not released during the pre-melt, so surface energy of the solder might be reduced to a balanced state. After the devices were released and solders were melted again, the shape of solder did not change too much. This should be an important issue in this method. Some solutions of the above problems will be proposed and discussed in Chapter 5.



(a) Solder covers the entire pad region.



(b) Solders do not cover the entire pad and have different melted shapes.

Figure 3-12: Schematic and SEM for solder melt

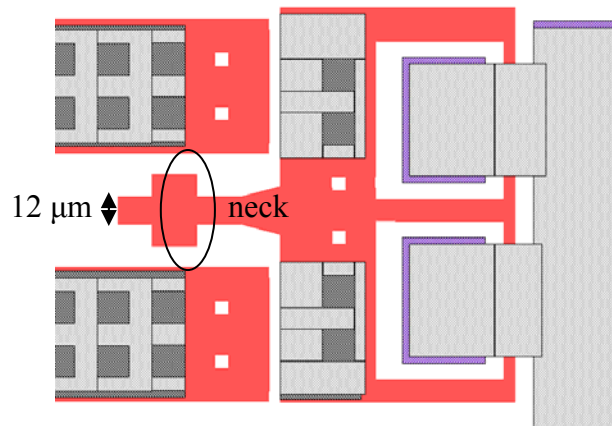


Figure 3-13: Layout of the inappropriate latch structure

(5) Latch structure design

One of the latch designs was not appropriate for assembly using probe. The layout is shown in Figure 3-13. Probe was hard to pick it up because the width was just 12 μm . The neck was easily broken when being picked up from side.

3–4 Summary

Two fabrication processes were investigated in this chapter. Although there were some problems in the original integrated SOI and SU-8 process, they were solved by changing the materials or adjusting process parameters. In order to improve the yield of assembly, the manual assembly can be replaced by self assembly. This was the first attempt to use the solder reflow for self-assembly. Although the result was not successful, some important issues were discovered in this experiment.

Chapter 4

Experiment Results and Measurement

This chapter presents the results of experiment and the measurement. The first part shows the measurement of SU-8/Single Crystal Silicon stress beam. The integrated devices are shown in the second part. The scanning electron microscopy (SEM) photographs and the optical measurement of individual devices are shown. Finally, the photo diode is discussed.



4-1 SU8/Single Crystal Silicon Stress Beam

In the releasing process, the frame of lens or mirror is lifted up by the stress beams and the stress beams also can prevent sticking to the substrate. So it plays an important role at the beginning of the release step. Figure 4-1 is a SEM photograph of the stress beams designed to measure the tip deflection. In the photograph, it can be seen that they all have a curvature introduced by the residual stress. Figure 4-2 is the measurement of the longest stress beam in Figure 4-1. The vertical displacement of the longest beam is about 35 μm , similar to the calculated result. Figure 4-3 shows the deflections of beams with length from 100 μm to 500 μm . The curvatures of these beams are almost the same even if their length is different.

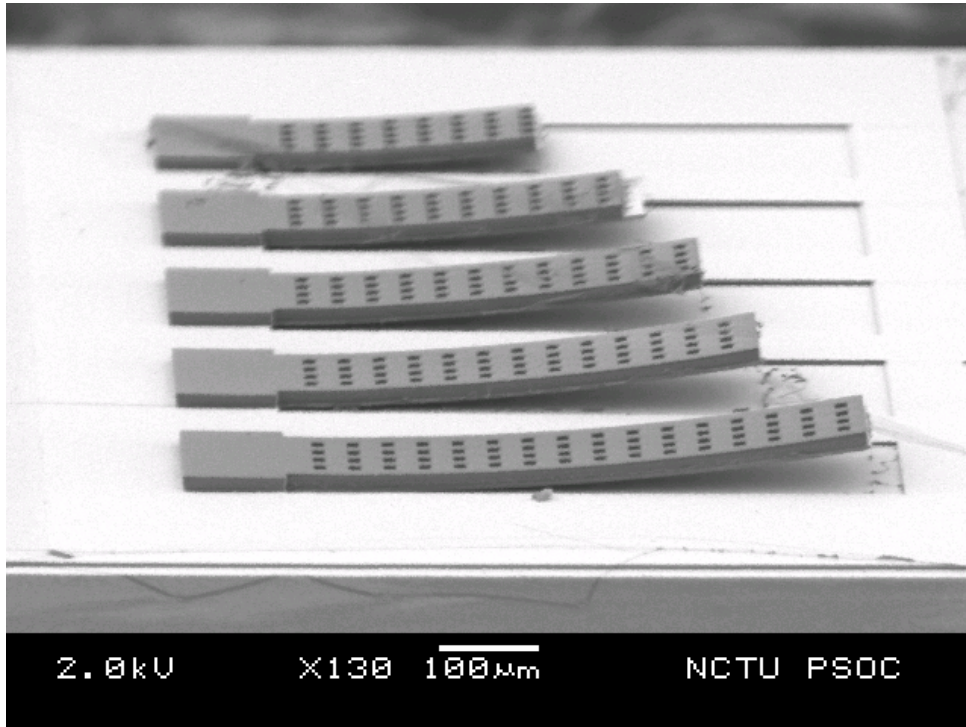


Figure 4-1: SU-8/SCS stress beams

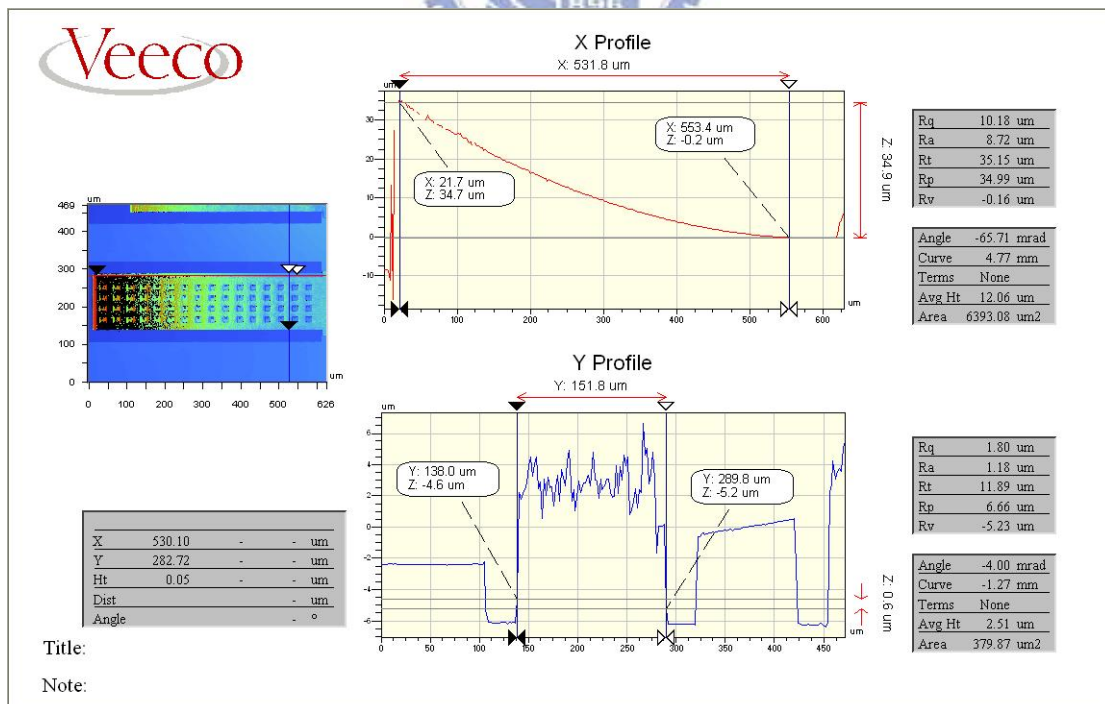


Figure 4-2: SU-8 stress-induced beam measured by WYKO-NT1100

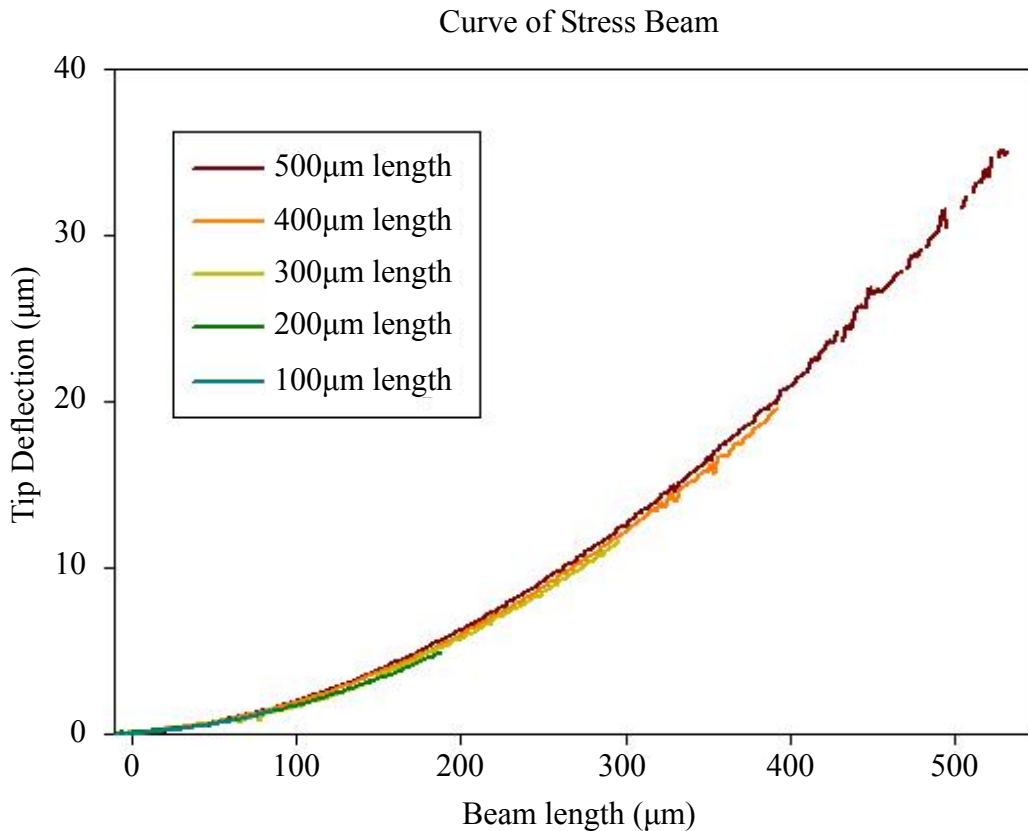
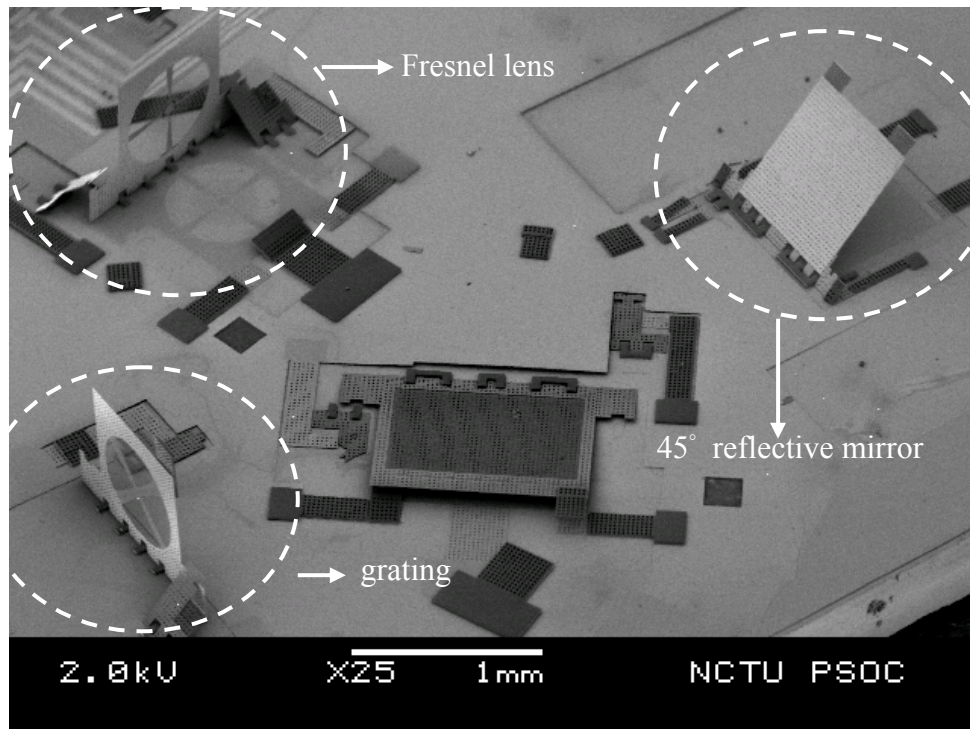


Figure 4-3: Deflection of stress beams with different length

4-2 Integrated Devices of Optical Bench

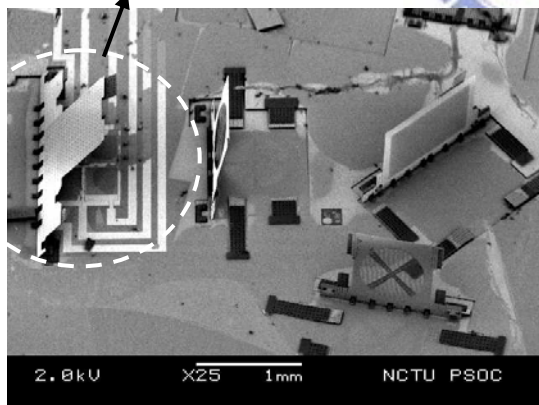
Figure 4-4 shows SEM photographs of the optical bench after assembly. Figure 4-4 (a) and (b) are the optical bench composed of silicon nitride optical devices. Figure 4-4 (c) is composed of SU-8 optical components. It can be seen that not all the components were well-assembled. The design of the anchor was the reason. The anchor was designed to cover the rotation hinge after releasing. Each device had two latches to fix it after releasing. In order to prevent the SU-8 anchor from peeling off, one of the anchor of latches was design as a “C” shape to increase the contact area. As the result, the latch could not slide into the notch as shown in Figure 4-5. According to the anchor geometry, the final angel changed from 37° to 58° . So the device can not

be fixed perfectly. The airflow may topple those devices when the SEM chamber is vented.



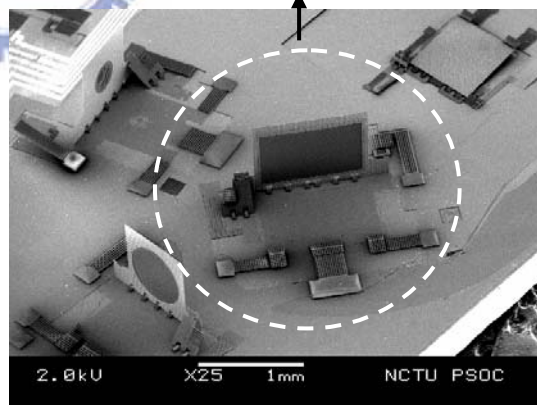
(a)

135° reflective mirror and photo detector



(b)

polarizer beam splitter



(c)

Figure 4-4: Integrated optical bench (a) Si_3N_4 based devices, (b) Si_3N_4 based devices with 135° reflective mirror and photo diode, (c) SU-8 based devices,.

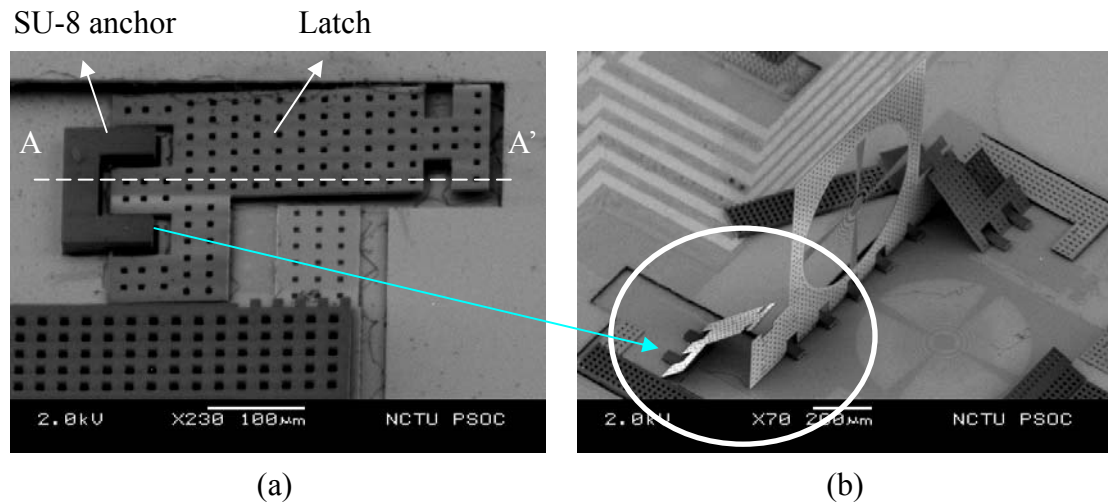


Figure 4-5: Failed assembly of latch structure.

(a) the C-shape SU-8 anchor, (b) latch and notch, (c) AA' cross section of latch rotation

4-3 Measurement of Optical Devices

This section focuses on the optical measurement of individual devices, especially the grating and the Fresnel lens.

- **Curvature measurement**

Optical surface curvature is very important for their optical performance. This is also the reason why SOI wafer is chosen. The surface of the silicon nitride grating is shown in Figure 4-6. The radius of curvature is 0.11 m in the x direction and 0.61 m in the y direction. The difference of height is about 0.9 μm in the x direction and 0.3 μm in the y direction. Figure 4-7 shows the measurement of silicon nitride polarizing beam splitter surface. The radius of curvature is 0.28 m in the x direction and 0.20 m

in the y direction. The difference of height is about 0.3 μm in the x direction and 0.4 μm in the y direction. Figure 4-8 shows the surface of silicon nitride Fresnel lens. The radius of curvature is 0.91 m in the x direction and 0.18 m in the y direction. The difference of height is about 0.2 μm in the x direction and 0.5 μm in the y direction.

Then the profile of the SU-8 based devices are measured and shown in Figure 4-9 to 4-11. For the SU-8 grating, the curvature is 0.18 m in the x direction and 0.23 m in the y direction. The difference of height is about 0.4 μm and 0.3 μm in the x and y direction respectively. The radius of curvature of SU-8 polarizing beam splitter is 0.64m in the x direction and 0.32m in the y direction. The difference of height is about 0.2 μm and 0.3 μm in the x and y direction respectively. The radius of curvature of SU-8 Fresnel lens is 0.2 m in X direction and 0.38 m in Y direction. The difference of height is about 0.3 μm and 0.2 μm in the x and y direction respectively.

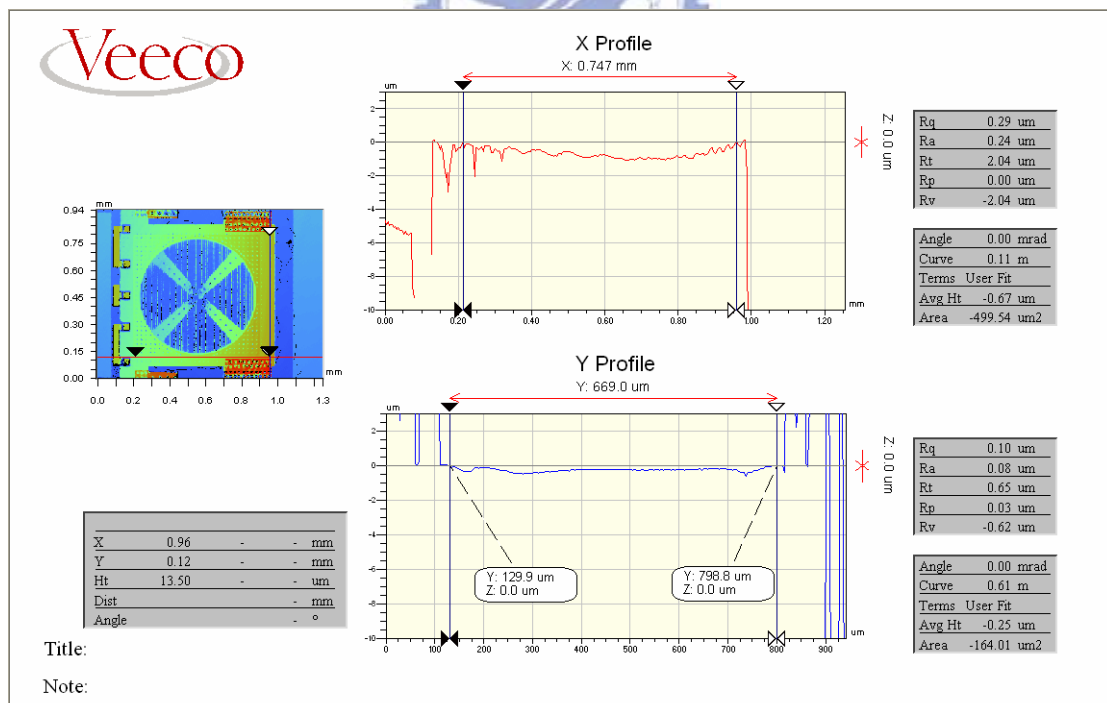


Figure 4-6: Curvature of the Si_3N_4 grating

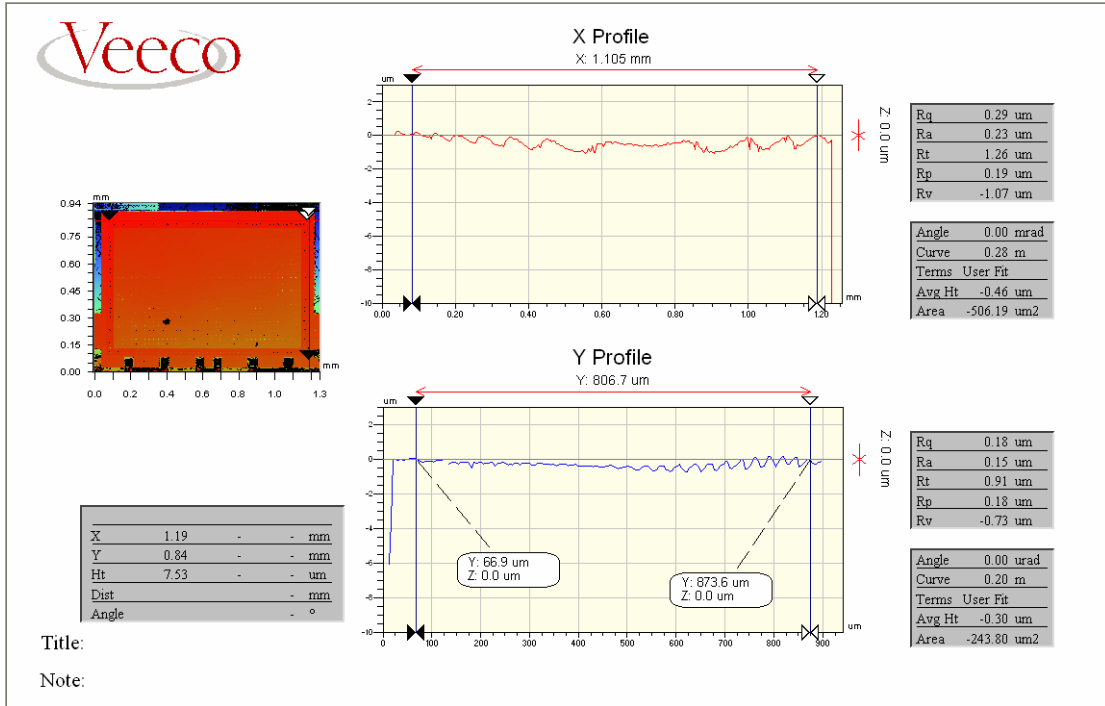


Figure 4-7: Curvature of the Si₃N₄ PBS

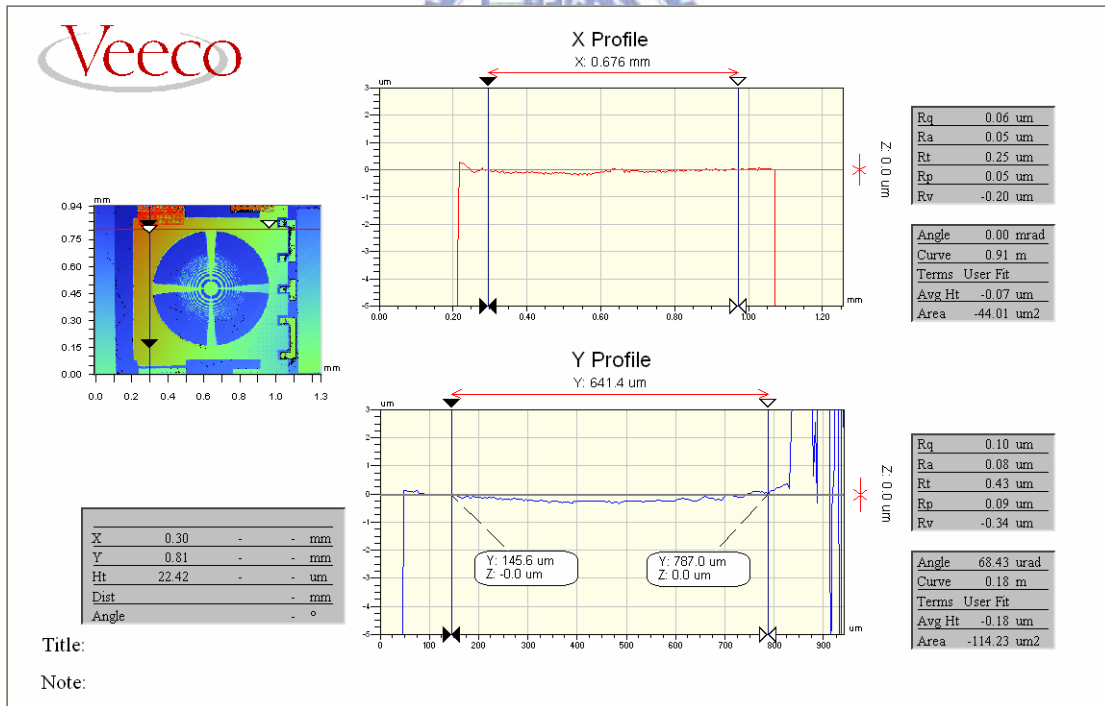


Figure 4-8: Curvature of the Si₃N₄ Fresnel lens

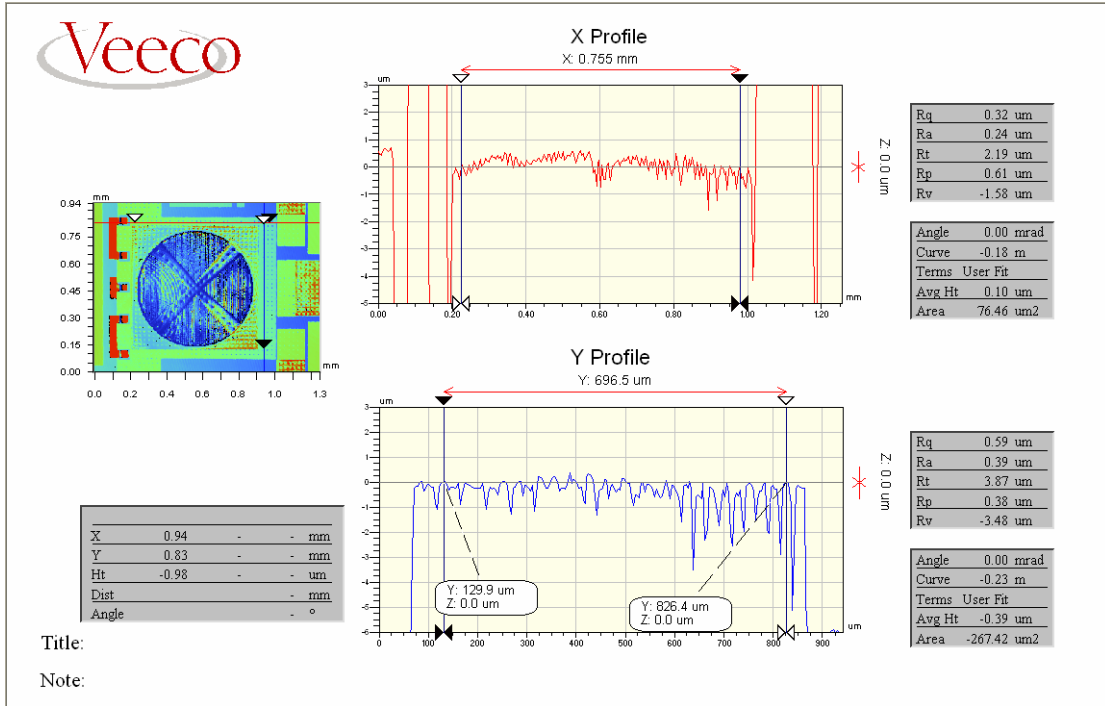


Figure 4-9: Curvature of the SU-8 grating

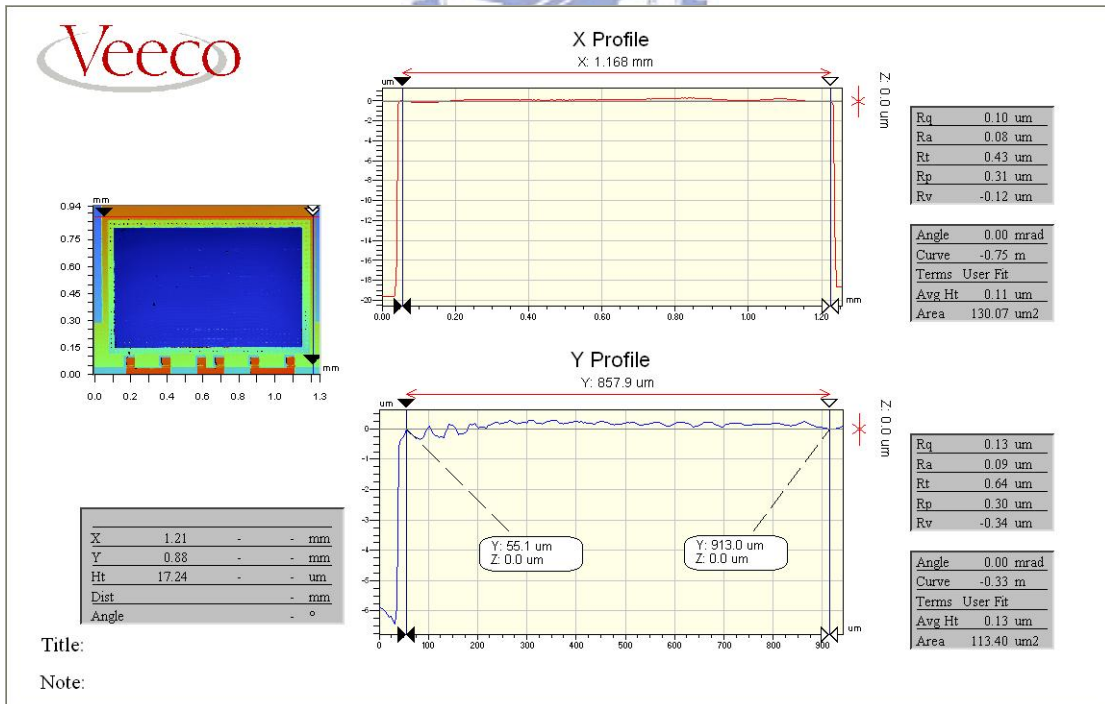


Figure 4-10: Curvature of the SU-8 PBS

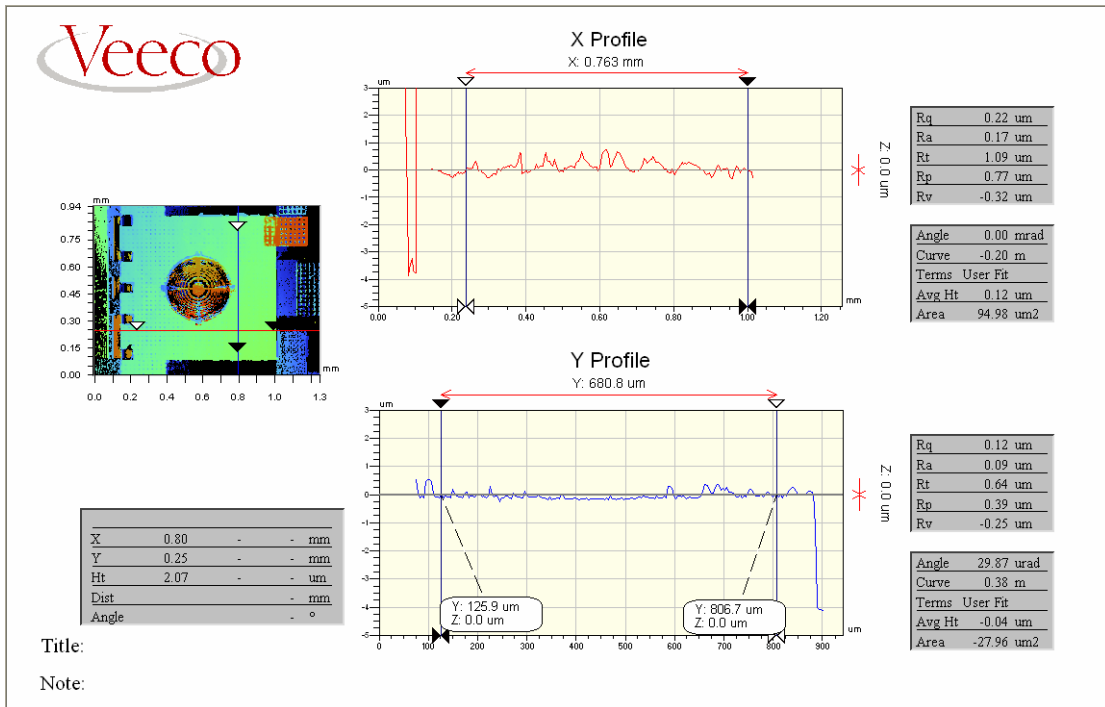


Figure 4-11: Curvature of the SU-8 Fresnel lens

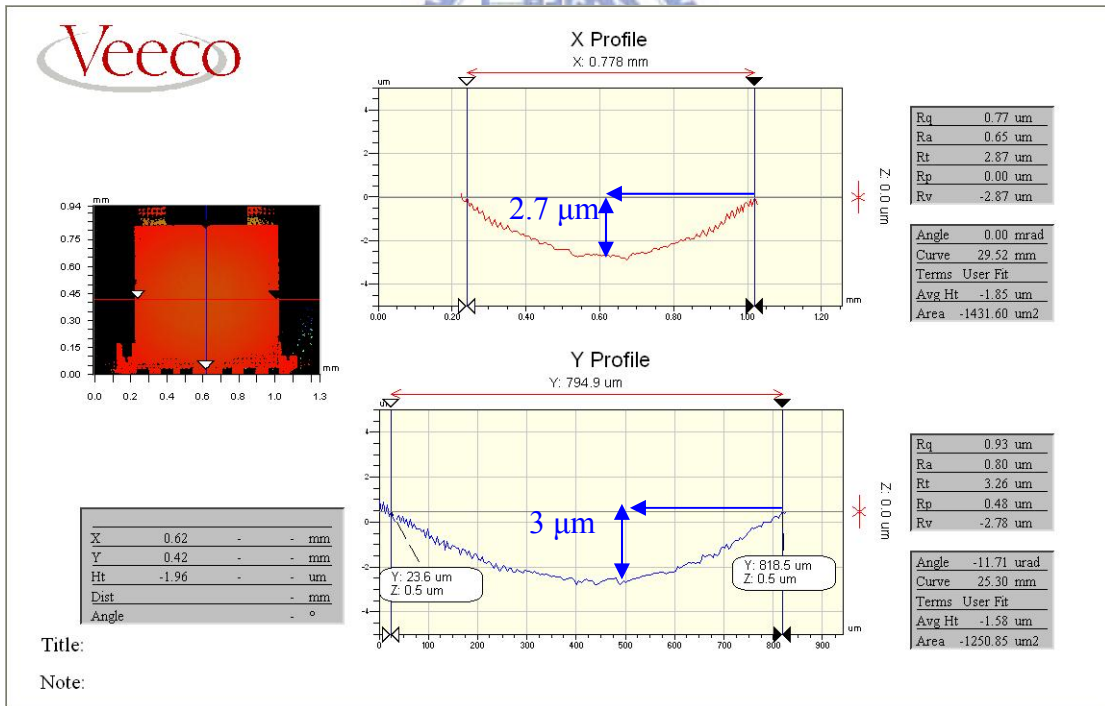


Figure 4-12: The curves of reflective mirror

According to the above figures, SU-8 and silicon nitride devices are both flat. But the condition in the reflective mirror is not so perfect. Figure 4-12 shows the surface measurement of the reflective mirror. The curves are 29.63 mm in the x

direction and 25.06 mm in the y direction. The drop height of the x direction is 2.7 μm and the y direction is 3 μm . The reason is the gold layer. The residual stress of gold produces this curvature after releasing. This may cause the optical beam to be distorted.

- **Optical measurement**

Figure 4-13 is a SEM photograph of SU-8 grating. The measurement system is shown in the Figure 4-14. The wavelength of the incident red laser light was 633 nm. The distance between grating and screen was about 33.5 cm. So, the diffraction angle θ was measured as

$$\theta = \tan^{-1}\left(\frac{2.072}{33.5}\right) = 3.54^\circ$$

According to the formula of diffraction grating, the grating pitch was 10 μm and diffraction angle was calculated as 3.63°. The measurement result is close to the design. The screen was then replaced by a CCD camera. Figure 4-15 shows the image captured by the CCD. The image was analyzed by Matlab, as showing in Figure 4-16. The diffraction efficiency ratio of the 0th order beam intensity I_0 and the ± 1 st order beam intensities $I_{\pm 1}$ is about 5.

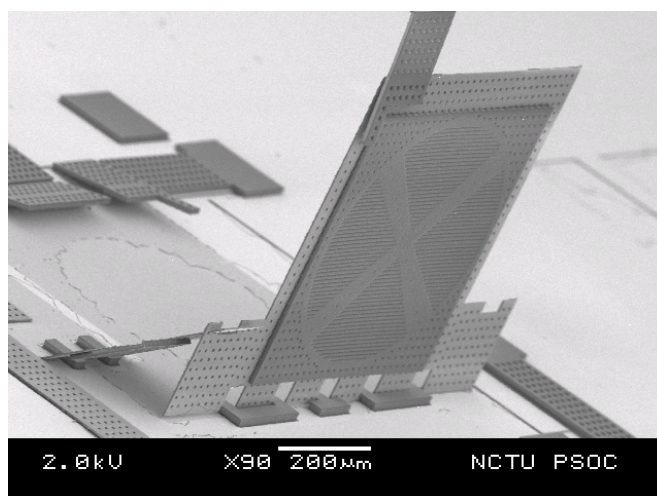


Figure 4-13: SEM of SU-8 grating

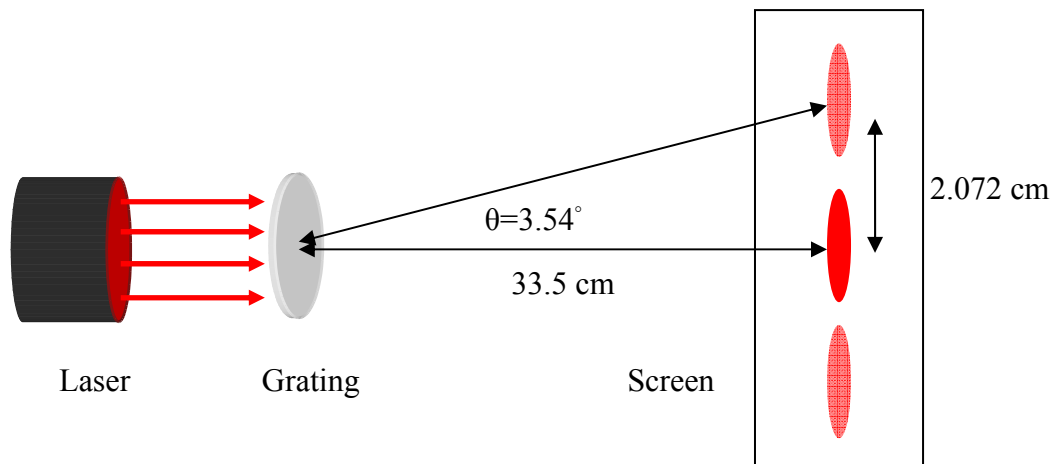


Figure 4-14: Schematic diagram of optical measurement of grating

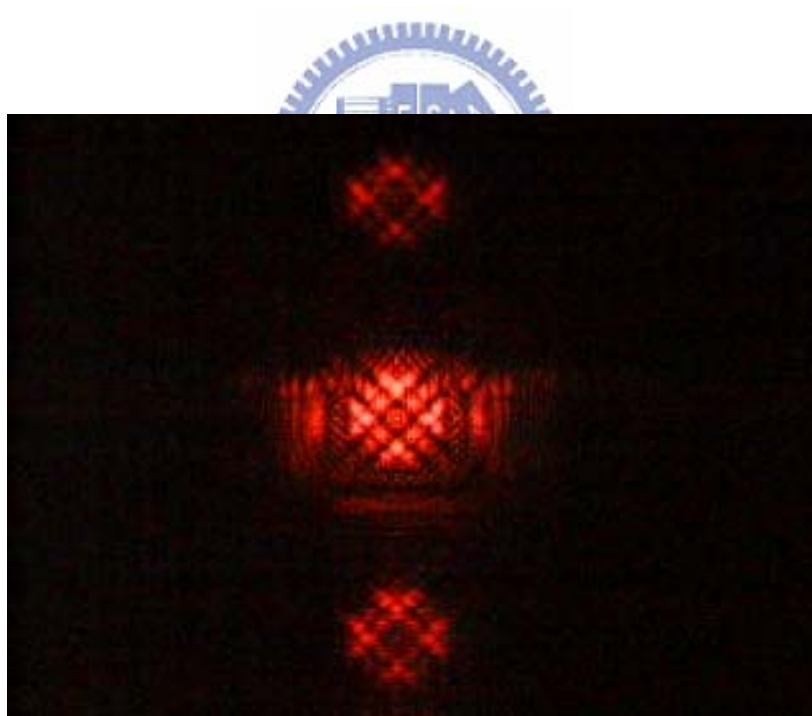
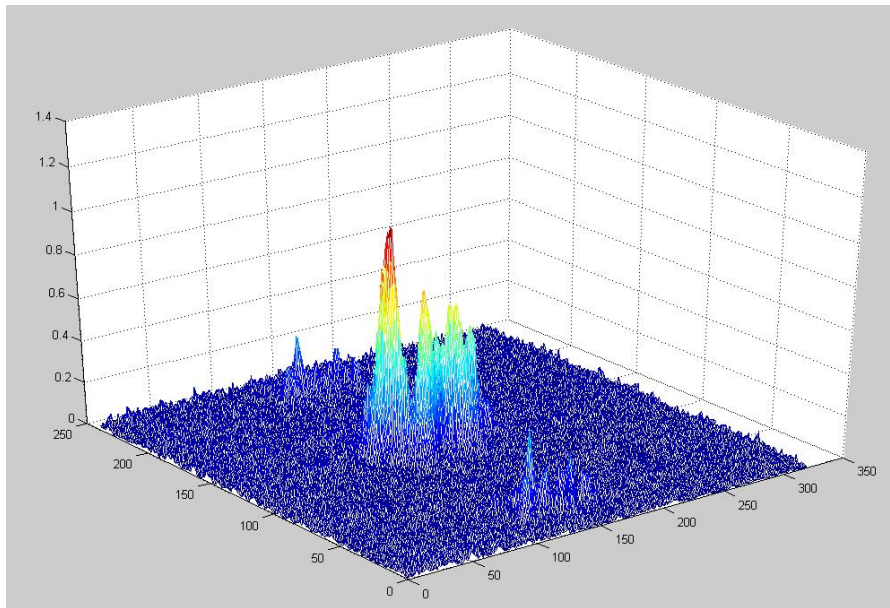
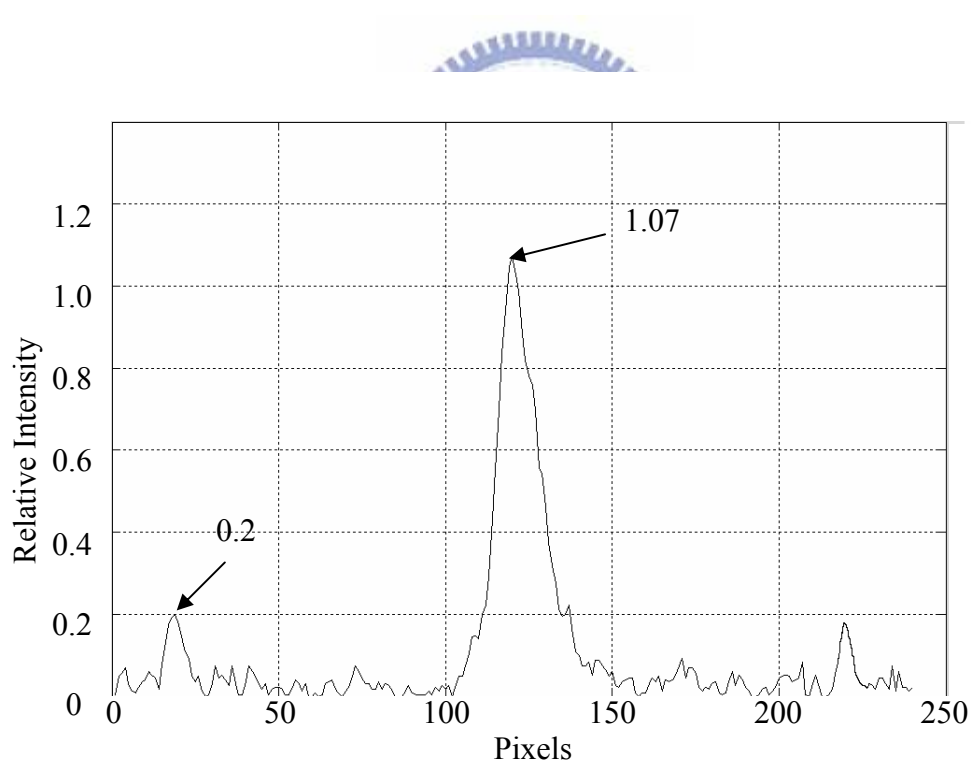


Figure 4-15: CCD image of diffracted spots.



(a) 3D profile of diffracted spots



(b) 2D plot of diffracted spots

Figure 4-16: Optical measurement of grating

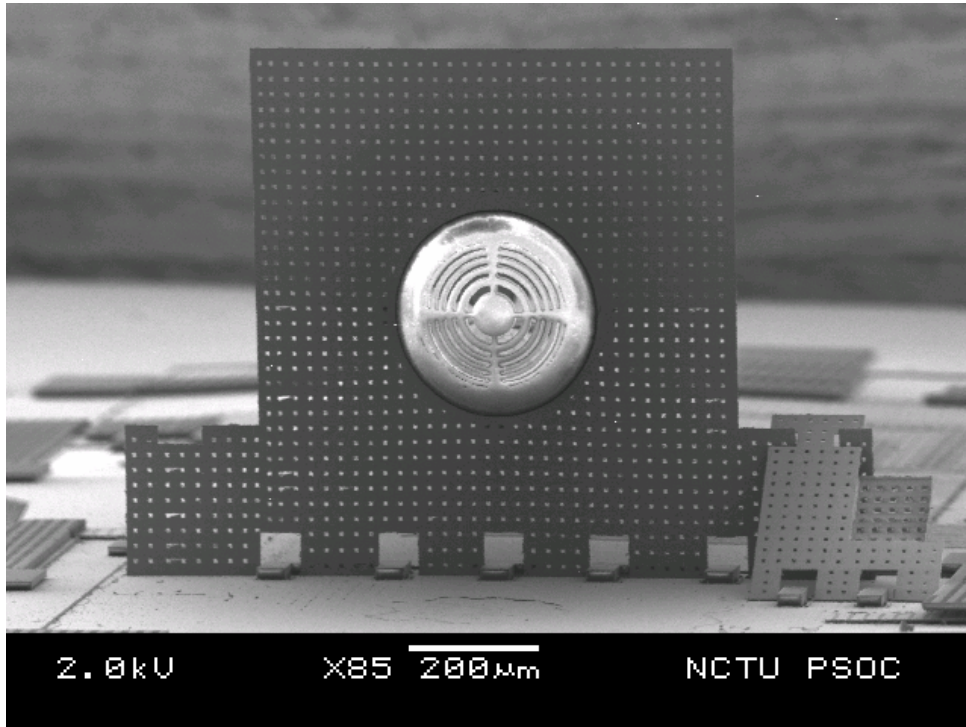


Figure 4-17: SEM of SU-8 Fresnel lens

Figure 4-17 shows the SEM photograph of a SU-8 Fresnel lens. The measurement instruments are showed in the Figure 4-18. At first, a proper position is determined for projecting a clear Fresnel lens image on the screen, as showing in Figure 4-19(a). Then the Fresnel lens or objective lens was moved a short distance f_1 until a brightest focused spot are shown on the screen, as Figure 4-19(b) shows. The distance f_1 is the focal length of this Fresnel lens. After a series of optical experiments, the focal length is measured as about 1.82 mm. The numeric aperture (N.A.) value of this lens is about 0.09,

$$\begin{aligned}
 \text{N.A.} &= \sin\theta = \sin\left(\tan^{-1}\left(\frac{r}{f}\right)\right) \\
 &= \sin\left(\tan^{-1}\left(\frac{165}{1820}\right)\right) \\
 &= 0.09
 \end{aligned}$$

where r is the radius of lens and f is focal length. The diffraction limit of the spot size, d , can be calculated as

$$d \approx \frac{0.5\lambda}{\text{N.A.}} = \frac{0.5 \times 0.633 \mu\text{m}}{0.09} = 3.52 \mu\text{m},$$

where λ is the wavelength of the red laser beam used in this experiment. The spot image captured by CCD is showed in Figure 4-20. The Full Width at Half Maximum (FWHM) of the focused spot can be calculated as about 3.58 μm . It is close to the theoretical value.

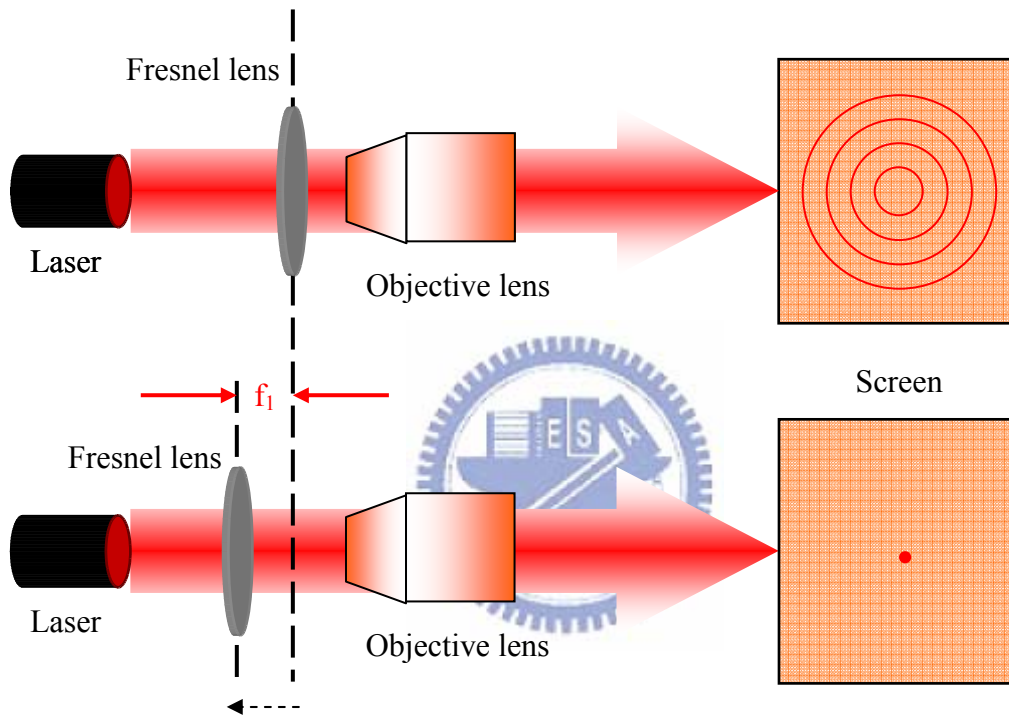


Figure 4-18: Schematic diagram of the optical measurement

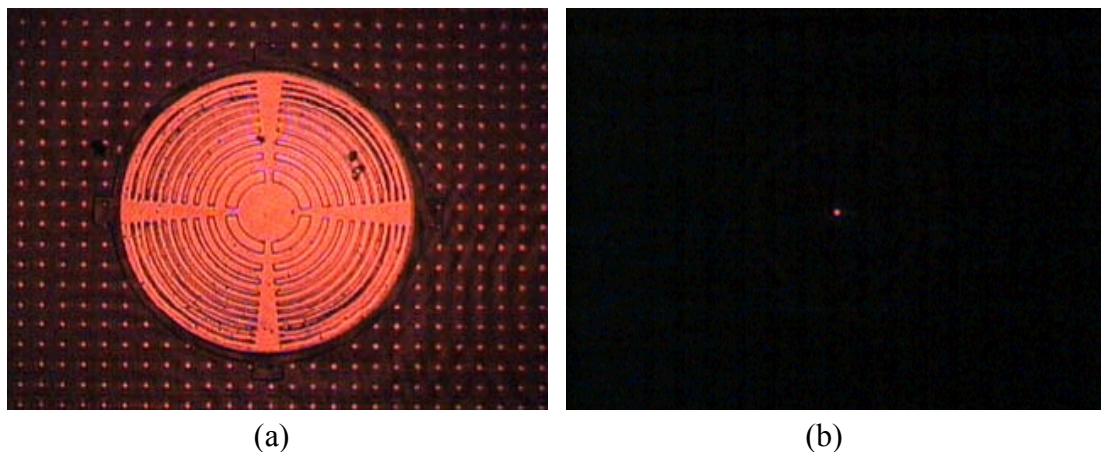
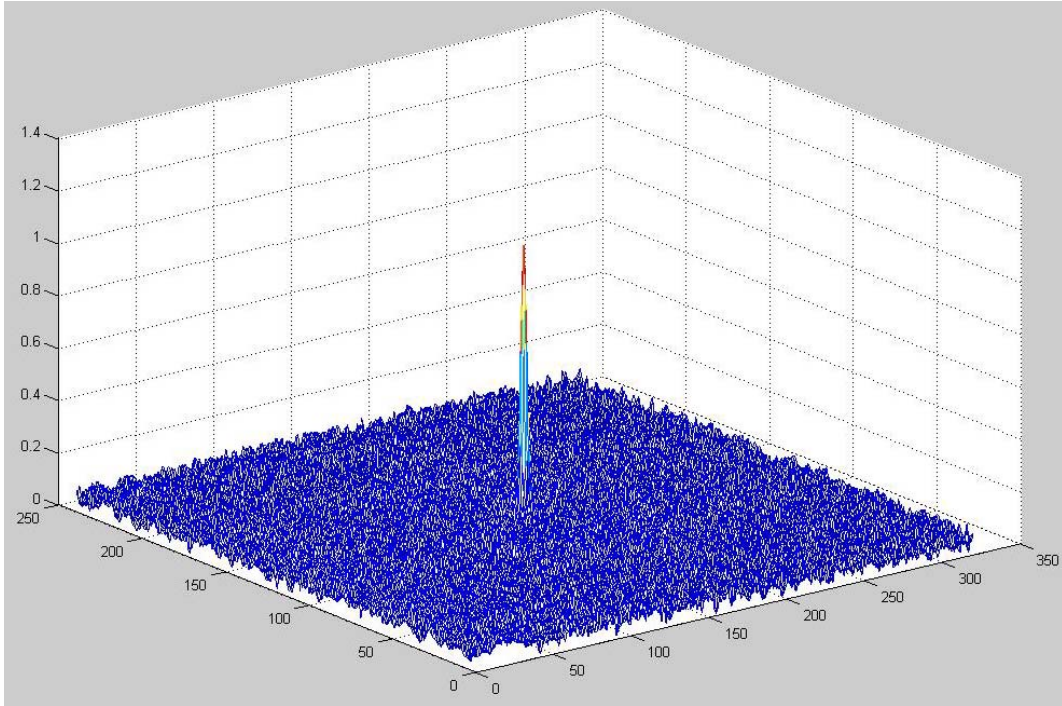
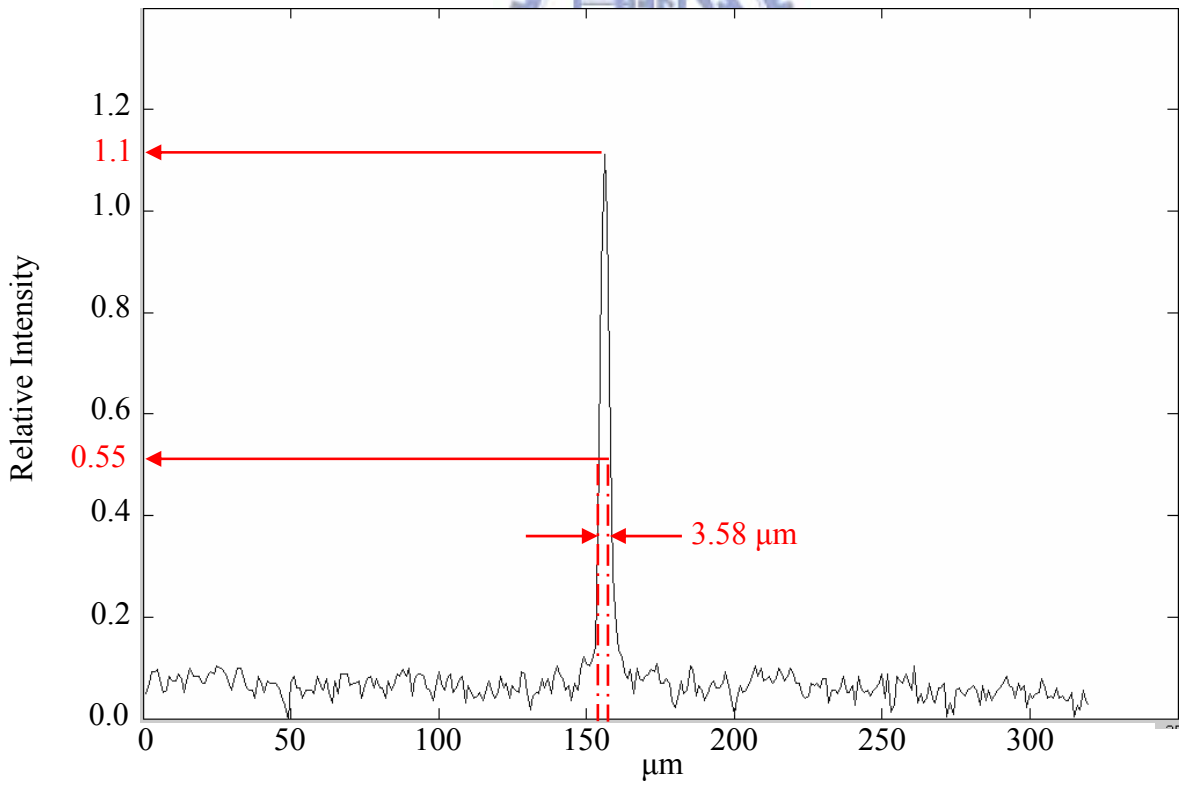


Figure 4-19: CCD image (a) Fresnel lens, (b) focused spot



(a) 3D profile of focused spot



(b) 2D profile of focused spot

Figure 4-20: Analysis of focused spot image

4-4 Photo detector

Figure 4-21 shows the 135° reflective mirror and the quad photo detectors for detecting the returned optical signal. Because the returned optical signal from disc is a digital signal, the current response of the diode is an important issue. The photo detector was measured by a Keithley 4200 semiconductor analyzer system before release. Figure 4-22 shows the reverse biased I-V curves of one of the photo diodes with and without light. Figure 4-23 shows the forward biased I-V curves. The solid line is the measured result with illumination, and the dashed line is the result without light. The power of the optical microscope light is 7.28 mW on a $9.5 \times 10^7 \mu\text{m}^2$ detector measured by a Newport powermeter set at 600 nm. The dimension of one diode is $122400 \mu\text{m}^2$. Therefore, the sensitivity can be calculated to be about 1.6 A/W.

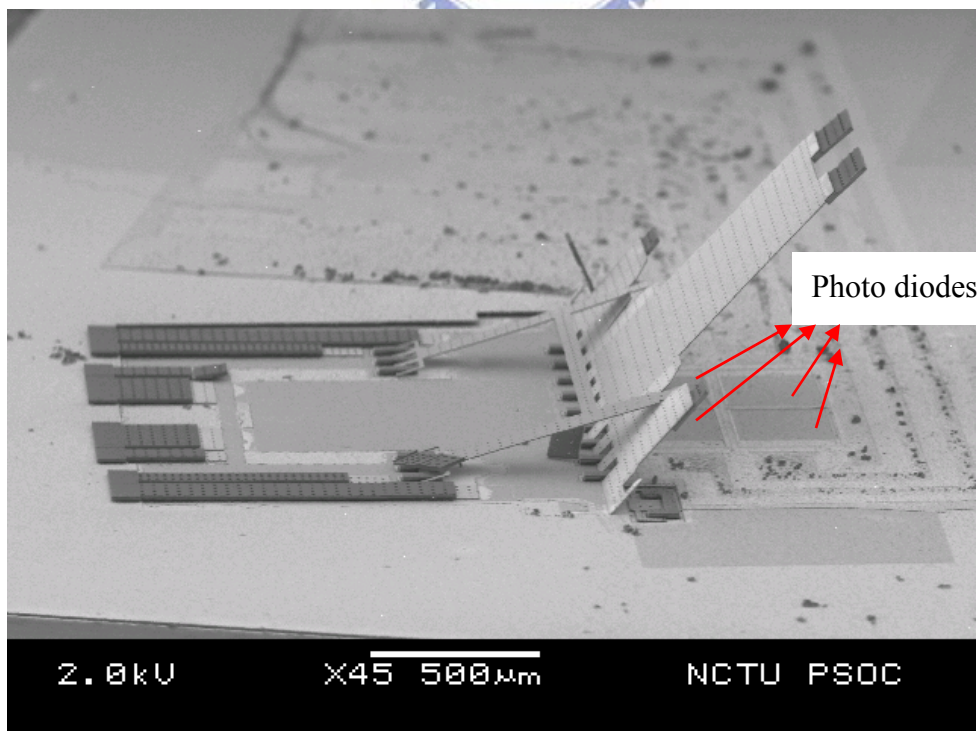


Figure 4-21: 135° reflective mirror and photo detectors

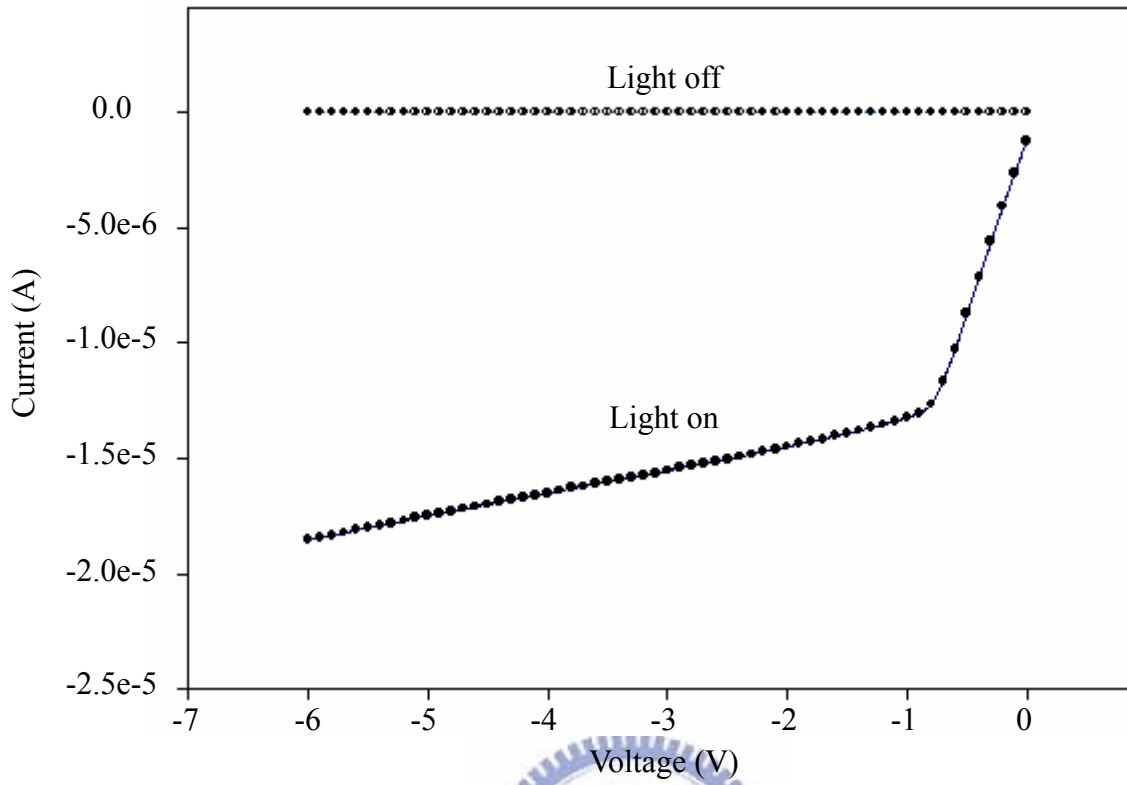


Figure 4-22: Reverse biased I-V curve of photo diode with and without light

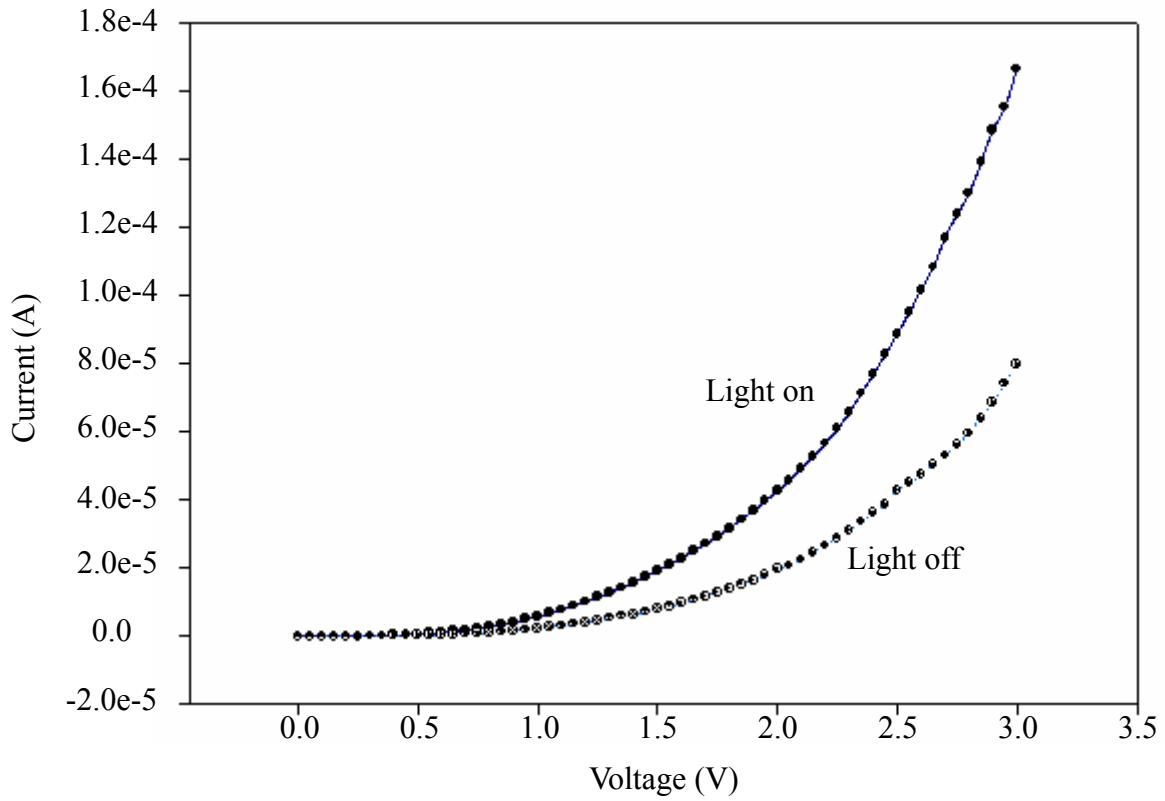


Figure 4-23: Forward biased I-V curve of photo diode with and without light

4-5 Summary

Although this optical bench system was not assembled perfectly, the flatness of the most devices was acceptable. The reflective mirror has a larger curvature than others because the gold layer is deposited on the surface. This is a problem needed to be overcome. The performance of SU-8 devices has been verified, and it may get a better performance by a detail optical design. In the following chapter some future works will be discussed.



Chapter 5

Conclusion and Future Work

5-1 Conclusion

The novel fabrication process to integrated SU-8 and SOI wafer is demonstrated and used to fabricate a basic optical bench in this thesis. The stress-free and single-crystalline natures of the SOI device layer and the transparency of SU-8 in the visible spectrum range makes this process ideal for integration of mechanical structures, optical devices, photo detectors, and circuits.

The silicon nitride thin film is used as the optical elements in this thesis. Although there is a problem about the small line width, the solution has been discussed in Sec. 3-3. Replacing silicon nitride by SU-8 for optical components not only solves the problem but also simplifies the fabrication process. The optical performance has been measured and discussed in Sec. 4-2.

Self-assembly can simplify the assembly process and reduce the risk of manual operation. The failure of the self-assembly in this thesis has been discussed in Sec. 3-3. Some of the future work will be discussed in the following.

5-2 Future work

To solve the problem of surface energy of solder balls, electroplating can be used. The initial shape is closer to the design in Sec. 2-2. To avoid stiction, dimple and back side etching are two solutions. If the back side of optical device is etched entirely, the die of the bench will be fragile. Dimple structure is difficult to fabricate under the

device layer. A new idea to integrate these two solutions is proposed. The back side pattern of each device is designed as shown in Figure 5-1. Several concentric rings are connected with bars and connected with the substrate after backside etching. This design can prevent the pattern from falling off the substrate after releasing. The remaining part plays a roll like dimple during releasing. This may reduce the probability of stiction. Furthermore, because the release process can be executed from back side by HF vapor, the release hole on the devices can be removed to improve the optical performance.

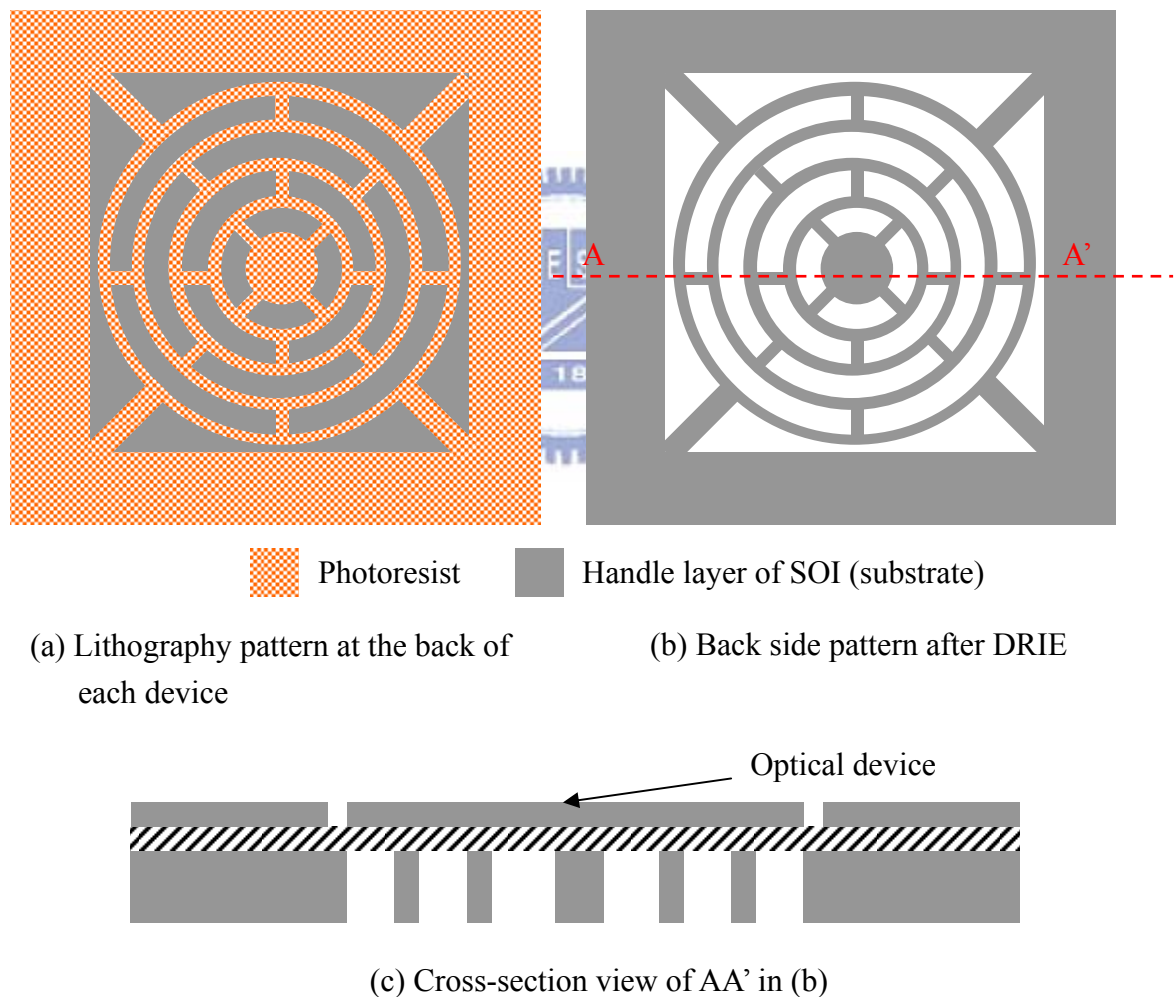


Figure 5-1: Dimple-like structure for SOI wafer to avoid stiction

Although the optical bench has been fabricated, some defects need to be improved. The small line width of the outside ring of Fresnel lens, the shape of anchor, and the spring latch design are the first targets to do. The SU-8 based optical element is a good idea to be integrates into this system. And a precise design in optical domain is necessary. Self-assembly is a good gateway to improve the yield of assembly, so it is worth trying to make the self-assembly successful. Finally, integration with the focusing and tracking device for a complete micro optical pick-up head system is the most important assignment in the future.



Reference

- [1] M. C. Wu, "Micromachining for optical and optoelectronic systems," *Proceedings of the IEEE*, vol. 85, no.11, pp. 1833-1856, 1997.
- [2] V. Milanovic, "Multilevel beam SOI-MEMS fabrication and applications," *Journal of Microelectromechanical Systems*, vol. 13 no. 1, pp19-30, 2004.
- [3] M. C. Wu, S. F. Shy and W. Fang, "Integrating the SOI and Poly-Si Surface Structures in a Monolithic Process for Optical Devices Platform," *IEEE/LEOS International Conference on Optical MEMS*, pp. 63-64, 2003.
- [4] F. Ayazi and K. Najafi, "High aspect-ratio combined poly and single-crystal silicon (HARPSS) MEMS technology," *Journal of Microelectromechanical Systems*, vol. 9, no. 3, pp.288-294, 2000.
- [5] G. T. A. Kovacs, N. I. Maluf, and K. E. Petersen, "Bulk Micromachining of Silicon", *Proceeding of the IEEE*, vol. 86, no. 8, pp. 1536-1551, 1998.
- [6] J. M. Bustillo, R. T. Howe, and R. S. Muller, "Surface Micromachining for Microelectromechanical Systems," *Proceedings of the IEEE*, vol. 86, no. 8, pp.1552-1574, 1998.
- [7] K. S. J. Pister, M. W. Judy, S. R. Burgett, and R. S. Fearing, "Microfabricated hinges," *Sensor and Actuators A-Physical*, vol. 33, no. 3, pp. 249–256, 1992.
- [8] J. W. Zu, Q. Qu, and G. Cheng, "Analytical Modeling and Quantitative Analysis of Scratch Drive Actuator" *Proceeding of ICMENS*, pp. 629-635, 2004.
- [9] Y. W. Yi and C. Liu, "Magnetic Actuation of Hinged Microstructures", *Journal of Microelectromechanical systems*, vol. 8, no.1, pp.10-17, 1999.
- [10] V. Kaajakari and A. Lal, " Electrostatic batch assembly of surface MEMS using ultrasonic triboelectricity," *Technical Digest. 14th IEEE International Conference on Micro Electro Mechanical Systems*, pp. 10-13, 2001.

- [11] T. Ebefors, E. Kalvesten, and G. Stemme, "New small radius joints based on thermal shrinkage of polyimide in V-grooves for robust self-assembly 3D microstructures," *Journal of Micromechanics and Microengineering*, vol. 8, no. 3, pp.188-194, 1998
- [12] Lucent Technology,
<http://www.bell-labs.com/org/physicalsciences/projects/mems/mems3.html>.
- [13] Y. P. Ho, M. Wu, H. Y. Lin and W. Fang, "A robust and reliable stress-induced self-assembly supporting mechanism for optical devices," *Microsystem Technologies*, vol. 11, no. 2-3, pp. 214-220, 2005.
- [14] L. Lijie, J. Zawadzka and D. Uttamchandani, "Integrated self-assembling and holding technique applied to a 3-D MEMS variable optical attenuator," *Journal of Microelectromechanical Systems*, vol. 13, no. 1, pp. 83-90, 2004.
- [15] D. C. Miller, Z. Wenge and V. M. Bright, "Microrelay packaging technology using flip-chip assembly," *Proceedings IEEE 13th Annual International Conference on Micro Electro Mechanical Systems*, pp. 265-270, 2000.
- [16] K. Beomjoon, D. Collard, M. Lagouge, F. Conseil, B. Legrand and L. Buchaillot, "Thermally actuated probe arrays for manipulation and characterization of individual bio-cell," *Proceedings IEEE 12th International Conference on Solid-State Sensors, Actuators and Microsystems*, vol. 2, pp. 1255-1258, 2003.
- [17] R. R. A. Syms, C. Gormley and S. Blackstone, "Improving yield, accuracy and complexity in surface tension self-assembled MOEMS," *Sensors and Actuators*, vol. 88, no. 3, pp. 273-283, 2000.
- [18] K. Harsh and Y. C. Lee, "Modeling for solder self-assembled MEMS," *Proceedings of the SPIE*, vol. 3289, pp. 177-184, 1998.
- [19] F. Ayazi, K. Najafi, "Design and Fabrication of a High-Performance Polysilicon

- Vibrating Ring Gyroscope,” *IEEE/ASME International Workshop, Micro Electro Mechanical Systems*, pp. 25-29, 1998.
- [20] V. Seidemann, S. Butefisch and S. Buttgenbach, “Fabrication and investigation of in-plane compliant SU8 structures for MEMS and their application to micro valves and micro grippers,” *Sensors & Actuators A-Physical*, vol. A97-98, pp. 457-461, 2002.
- [21] W. Zhang, M. Chan, “Properties and design optimization of photo-diodes available in a current CMOS technology,” *Proceedings. IEEE Hong Kong Electron Devices Meeting*, pp. 22-25, 1998.
- [22] H. S. Weng, R. T. Chang, E. Crabbe and P. Agnello, “CMOS active pixel image sensors fabricated using a 1.8 V, 0.25 μ m CMOS technology,” *IEEE Transactions on Electron Devices*, pp. 915-918, 1996. *vol.45, no.4, pp.889-894 1998*
- [23] T. K. Woodward and A. V. Krishnamoorthy, “1-Gb/s integrated optical detectors and receivers in commercial CMOS technologies,” *IEEE Journal of Selected Topics in Quantum Electronics*, vol. 5, no. 2, pp. 146-156, 1999.
- [24] T. N. Swe, K. S. Yeo and K. W. Chew, “Design and optimization of new high performance silicon photodiodes,” *Proceedings of IEEE, Asia-Pacific Microwave Conference*, pp. 685-688, 2000.
- [25] <http://aveclafaux.freesevers.com/SU-8.html>
- [26] H. Lorenz, M. Despont, N. Fahrni, J. Brugger, P. Vettiger and P. Renaud, “High-aspect-ratio, ultrathick, negative-tone near-UV photoresist and its applications for MEMS,” *Sensors & Actuators A-Physical*, vol. A64, no. 1, pp. 33-39, 1998.
- [27] H. S. Khoo, K. K. Liu and F. G. Tseng, “Mechanical strength and interfacial failure analysis of cantilevered SU-8 microposts,” *Journal of Micromechanics*

- & *Microengineering*, vol. 13, no. 6, pp. 822-831, 2003.
- [28] R. T. Chen, H. Nguyen and M. C. Wu, “A low voltage micromachined optical switch by stress-induced bending,” *Proceedings of IEEE international MEMS, 12th IEEE International Conference on Micro Electro Mechanical Systems*, vol. 11, pp. 424-428, 1999.
- [29] S. Timoshenko, “ Analysis of bi-metal thermostats,” *Journal of the Optical Society of America*, vol. 11, pp. 233-255, 1925.
- [30] M. W. Judy, Y. H. Cho, R. T. Howe and A. P. Pisano, “Self-adjusting microstructures (SAMS),” *Proceedings. IEEE Micro Electro Mechanical Systems. An Investigation of Micro Structures, Sensors, Actuators, Machines and Robots*, pp. 51-56, 1991.
- [31] J. E. Shigley and L. D. Mitchell, *Mechanical Engineering Design*, 4th Edition, McGraw-Hill, New York, NY, 1993.
- [32] M. Madou, *Fundamentals of Microfabrication*, 1st Edition, New York, NY: CRC Press, 1997.
- [33] R. R. A. Syms, E. M. Yeatman, V. M. Bright, and G. M. Whitesides, “ Surface Tension-Powered Self-Assembly of Microstructures - The State-of-the-Art,” *Journal of MicroMicroelectromechanical systems*, vol.12, no.4, 2003
- [34] R. R. A. Syms and E. M. Yeatman, “Self-assembly of fully three-dimensional microstructures using rotation by surface tension forces,” *Electronics Letters*, vol. 29, no. 8, pp. 662–664, 1993.
- [35] M. E. Motamedi, M. C. Wu and K. S. J. Pister, “Micro-opto-electro-mechanical devices and on-chip optical processing,” *Interational Society for Optical Engineering*, vol. 36, no. 5, pp. 1282-1297, 1997.